

Spectroscopic Investigation of Indium Halides as Substitutes of Mercury in Low Pressure Discharges for Lighting Applications

Dissertation zur Erlangung des Doktorgrades
an der Mathematisch-Naturwissenschaftlichen Fakultät
der Universität Augsburg

vorgelegt von
Stefan Briefi
am 23. Dezember 2011

Vorgelegt am 23. Dezember 2011

Tag der mündlichen Prüfung: 22. Mai 2012

Erster Gutachter: apl. Prof. Dr.-Ing. U. Fantz

Zweiter Gutachter: Prof. Dr. W. Brütting

Contents

1	Introduction	5
2	Finding Substitutes for Mercury in Fluorescent Lamps	7
2.1	The Role of Mercury in Fluorescent Lamps	7
2.2	The Role of Background Gases in Low Pressure Discharge Lamps	9
2.3	Requirements for Substitutes and Potential Candidates	10
2.4	Spectral and Molecular Properties of InBr and InCl	12
3	Properties of Low Temperature Low Pressure Plasmas	17
3.1	Plasma Generation and Heating Mechanisms	17
3.2	Population Processes, Models and Balances	20
3.2.1	Population of Electronic States	21
3.2.2	Ionization and Ambipolar Diffusion	23
3.2.3	Population of Vibrational States in Molecules	25
3.2.4	Population of Rotational States in Molecules	26
3.2.5	Corona Model and Collisional-Radiative Model	28
3.2.6	Ionization Balance and its Impact on T_e	30
3.2.7	Power Balance and its Impact on n_e	32
3.3	Opacity and Radiation Transport	36
3.3.1	Line Profiles	37
3.3.2	The Escape Factor Concept	39
4	Diagnostic Methods	43
4.1	Optical Emission Spectroscopy	43
4.1.1	Optical Emission Spectroscopy of Molecules	44
4.1.2	Correction of Reabsorption Effects	45
4.2	White Light Absorption Spectroscopy	48
4.2.1	True and Apparent Optical Depth	49
4.2.2	Correction of the Apparent Optical Depth	51
4.3	Extended Corona Model of Indium	54

4.4	The Collisional-Radiative Model Yacora Argon	60
4.5	Simulation of the Indium Halide A-X and B-X Emission Spectra	65
4.5.1	Computing Method	65
4.5.2	FCF and $A_{ik}^{v'v''}$ for InBr	69
4.5.3	Fitting Procedure for InBr	71
4.5.4	FCF , $A_{ik}^{v'v''}$ and Fitting Procedure for InCl	72
5	Experimental Setup	75
5.1	Plasma Generation	75
5.2	Spectroscopic Setup	77
5.3	Cold Spot Setup	80
6	Investigation of the RF-Coupling Method	83
6.1	Using Sealed Discharge Vessels	83
6.2	Using a Variable Vacuum Setup	86
7	Investigation of InBr as Radiating Species	89
7.1	Variation of the Cold Spot Temperature	89
7.2	Variation of the RF-Power	102
7.3	Variation of the Background Gas	109
8	Investigation of InCl as Radiating Species	115
8.1	Variation of the Cold Spot Temperature	115
8.2	Variation of the RF-Power	122
8.3	Variation of the Background Gas	123
9	Outlook on a Low Pressure Indium Halide Lamp	125
10	Summary	131
Appendix		139
A	Molecular Constants and Ionization Cross Sections	139
B	Integration over Solid Angle in an Infinite Cylinder	141
C	Data on the Hyperfine Splitting of Indium	144
Bibliography		147
Acknowledgements		157
Curriculum Vitae		158

1 Introduction

In general lighting, 61.8% of the global electrically generated light is provided by linear or compact fluorescent lamps [IAE06]. This high share arises from the widespread application in industrial, commercial and residential lighting. The remaining global electric-light production is subdivided between the share of high pressure discharge lamps (27.2%) which are primarily applied in outdoor and industrial lighting and incandescent light sources (11.0%) which are used in commercial and residential lighting [IAE06]. The role of solid state light sources (organic and inorganic light-emitting diodes) is still negligible on a global scale but the ongoing progress in improving their efficiency and total light output indicates that their role will increase heavily in the near future. However, recent studies predict that the share of solid state light sources primarily increases on the expense of the share of high pressure and incandescent lamps. At present, a large-scale substitution of fluorescent lamps seems very unlikely due to the high price of solid state light sources. In the near future, it is estimated that still 60% of the global electrically generated light is provided by fluorescent lamps [Fro11].

Fluorescent lamps are low pressure mercury containing rare gas discharges with internal electrodes which generate ultraviolet mercury radiation at 253.7 nm very efficiently. The mercury emission is converted into visible light by means of phosphors. A very critical aspect of fluorescent lamps is the toxicity of mercury. In the European Union the use of mercury is prohibited in all electronic devices according to the “Restriction of certain Hazardous Substances Directive” (RoHS) 2011/65/EU (earlier 2002/95/EG). The most significant exception to this directive is the use of mercury for lighting applications but the approved amount is strongly regulated and decreases gradually over the next years. A substitution of mercury by a non-toxic substance in low pressure discharge light sources is highly desirable due to the retaining importance of such lamps in general lighting.

The application of possible candidates for replacing mercury is limited by several requirements. For example, the substance must have a suitable emission spectrum and a high vapour pressure. These demands are fulfilled by the di-

atomic indium monohalide molecules InBr and InCl whose A – X and B – X emission spectra are located in the near-ultraviolet spectral range between 330 and 400 nm. Moreover, indium which is generated by dissociation process in the discharge also radiates intensely in the near-UV. The use of metal halides raises the issue, that power coupling by internal electrodes is not possible as the electrodes would quickly be eroded by the halides. Therefore inductive or capacitive RF-coupling with external electrodes has to be applied. Recent investigations already proved the concept of using indium halide low pressure discharges for generating near-UV emission and showed that a good efficiency can be achieved [HHK⁺10]. These first measurements were restricted to capacitive RF-coupling using argon as background gas. However, the full potential was not explored as systematic investigations were not carried out and no effort was made to understand the physical processes which determine the discharge characteristics.

In this work, the applicability of InBr and InCl in a low pressure discharge light source is investigated from a more fundamental point of view. For this purpose sealed cylindrical quartz discharge vessels which contain a defined amount of indium halide and a rare gas are used. Preliminary investigations which were performed within the scope of a diploma thesis [Bri08] showed that the efficiency and the intensity of the generated InBr and indium emission strongly depend on the evaporated indium halide density. This amount is determined by the vapour pressure and the temperature of the coldest spot of the discharge vessel wall. For a controlled variation of the indium halide density a well-defined cold spot setup is mandatory. This was realized in the revised experimental setup.

A comparison of inductively and capacitively RF-coupling with respect to the generated light output and to the applicability for lighting purposes is carried out. Furthermore, the impact of the cold spot temperature, the RF-power and the background gas type on the discharge characteristics is investigated for rare gas plasmas containing InBr or InCl. The set of these parameters which yields the maximum efficiency of generating near-UV indium halide and indium emission is determined. In general, the focus is put on the comprehension of the physical processes which determine the discharge characteristics and on the identification of the processes which limit the radiation efficiency. For this purpose the diagnostic methods white light absorption and optical emission spectroscopy are used. The potential of a low pressure indium halide discharge light source is discussed by simulating the application of phosphors and by outlining the step towards a lamp prototype.

2 Finding Substitutes for Mercury in Fluorescent Lamps

2.1 The Role of Mercury in Fluorescent Lamps

Common fluorescent lamps are discharge lamps which consist of a tube that is filled with a rare gas (typically argon, krypton or neon or a combination thereof) at a pressure between two and five mbar and several mg of mercury [LLLG04, Way69]. The plasma is generated using internal electrodes at each end of the tube. An AC current of a few hundred mA at a frequency in the order of 10 kHz (electronic ballast) or 50 Hz (conventional ballast) is supplied to the electrodes to power the discharge. On the inner side of the tube a phosphor is applied that converts the ultraviolet mercury emission which is generated by the plasma into visible light. The phosphors efficiently absorb the radiation of the intense mercury line at 253.7 nm and their emission mostly covers the spectral range that can be detected by the human eye.

The plasma is a low temperature low pressure arc discharge with an electron temperature T_e of about 1 eV (1 eV \approx 11600 K), an electron density n_e between 10^{17} m^{-3} and 10^{18} m^{-3} and a gas temperature T_{gas} of 300 – 700 K [LLLG04]. The optimal mercury density of those lamps is reached at a partial pressure of around 7×10^{-3} mbar which is achieved according to the vapour pressure of mercury at a coldest spot temperature T_{CS} of the lamp vessel of around 42 °C [LLLG04]. Below this value, the mercury density is too low to obtain a high light output. Above 42 °C reabsorption of the emitted photons in the plasma results in a decreasing efficiency. The lamps are designed in a way that the optimum coldest spot temperature is reached automatically in normal operation.

The unique property of low pressure mercury/rare gas discharges is the very high efficiency of the generated UV radiation: 60 to 70% of the electrical input power are emitted in a single mercury line at 253.7 nm that arises from the transition between the excited 6^3P_1 state (excitation energy 4.86 eV) and the

6^1S_0 ground state [LLLG04, Nat11]. This extremely high efficiency of generating UV photons has several physical reasons:

- The transition of the 253.7 nm line is resonant, i. e. a transition that terminates on the ground state. In general, resonant transitions have a very large transition probability for spontaneous emission. As the intensity of an emission line is proportional to this probability, the intensity of the 253.7 nm line and therefore the efficiency is high.
- The radiating 6^3P_1 state is flanked by the metastable 6^3P_0 and 6^3P_2 states [Nat11]. As the energy difference between these states and the 6^3P_1 state is small, excitation or deexcitation processes of the metastable states that end on the radiating 6^3P_1 state and hence increase its population density are very likely [Way69]. As the intensity of an emission line is also proportional to the population density of the upper state, these processes contribute to the high intensity and efficiency of the 253.7 nm radiation.
- The excitation of the 6^3P state of mercury (which is split into the 6^3P_0 , 6^3P_1 and 6^3P_2 state) by electron impact is more likely than the excitation of other states in the mercury atom as the 6^3P state is the first excited state and the energy difference to the next excited states is several eV [Way69, Nat11]. As the velocity distribution of the electrons follows a Maxwellian distribution [Way69], a larger excitation energy of a state causes a smaller excitation rate which can result in a difference of the population density of several orders of magnitude due to the low electron temperature of these discharges. Therefore, at the typical electron temperature of 1 eV the population density of the 6^3P state is much larger than the one of the other excited states which in turn results in a strong domination of the 253.7 nm line in the mercury emission spectrum.
- Considering resonant radiation (radiation from transitions that terminate on the ground state), reabsorption plays a very important role. If the photons are reabsorbed many times before leaving the plasma (“trapped” photons), the probability increases that the 6^3P_1 state is deexcited without emitting a photon. Mercury occurs in seven isotopes, and six of them have a noticeable natural abundance [BLB⁺05]. The resonance line at 253.7 nm has a slightly different wavelength for each isotope. This wavelength difference is large enough that the typical line broadening mechanisms do not

lead to an overlap of the single lines [Way69]. Hence, each mercury isotope can only reabsorb photons which were emitted by the same isotope [Hol47, HAM52]. That means the density of mercury in the plasma can be six times higher before radiation trapping limits the efficiency than it would have been if mercury occurred as a single isotope.

However, due to the conversion of one UV photon with an energy of 4.86 eV to one photon in the visible spectral range (photon energies 1.5 – 3 eV) by the use of a phosphor, a large amount of energy and therefore efficiency is lost [Way69]. The wavelength shift between the absorbed and the emitted photon is called the Stokes shift. Considering the phosphor quantum efficiency of typically 80 to 90% this results in an overall efficiency of the generation of visible light of 20 – 25% [LLLG04] which is still very high for a light source.

2.2 The Role of Background Gases in Low Pressure Discharge Lamps

Basically in all discharge lamps rare gases are used as background gas. Background gases support the ignition of the lamp and they help to increase the efficiency due to several reasons which can differ for each discharge lamp type. In the mercury/rare gas plasma of fluorescent lamps the main function of the background gas is to slow down the diffusion of the electrons and ions to the wall [Way69]. As this diffusion determines the electron temperature (see section 3.2.6) the choice of the background gas pressure allows for an adjustment of the electron temperature to the desired optimum level. This level can be described qualitatively as high enough that excitation and radiation losses greatly exceed elastic collision losses and low enough that excitation of the 6^3P_1 state of mercury predominates over the excitation of all higher states (which leads to the domination of the 253.7 nm line in the emission spectrum) [Way69].

The low pressure sodium lamp contains a background gas at a pressure of a few mbar and sodium which radiates very efficiently in the visible spectral range at 589.0 and 589.6 nm [Way69, Nat11]. Therefore, low pressure sodium lamps do not need a phosphor to convert a UV photon into a visible one. As these lamps only emit in the yellow spectral range, they do not produce white light which limits the application to outdoor lighting [LLLG04]. Sodium has a very low vapour pressure compared to mercury, therefore its optimum partial

pressure which is about 4×10^{-3} mbar (similar to the one of mercury in fluorescent lamps) is not reached until a cold spot temperature of 260 °C [Way69]. As virtually no sodium is evaporated at ambient temperature, a background gas is required to ignite the lamp. During the starting phase that lasts for about 10 to 15 minutes, the lamp heats up and turns from a pure rare gas discharge into a sodium discharge [LLLG04]. Since the optimum electrical properties such as power input per unit length are very similar to those of fluorescent lamps which only reach $T_{CS} \approx 42$ °C, the low pressure sodium lamps need some special operating and design conditions. There are basically two solutions to increase the cold spot temperature intrinsically: First, insulating the lamp or applying an infrared reflecting coating at the lamp wall to reduce the cooling of the lamp and second, favouring the energy transfer from the hot electrons to the cold gas atoms to increase the dissipated amount of power [Way69]. The latter is done by using neon at a pressure of 10 mbar or higher as background gas. This high pressure of a lightweight-atom gas provides strong gas heating by elastic scattering of electrons which increases the cold spot temperature to the desired level [Way69, LLLG04].

In summary, the choice of the background gas and its pressure helps to operate low pressure discharge lamps at the optimum conditions considering cold spot temperature and electron temperature. Furthermore, the rare gas makes an ignition of the cold lamp possible if the vapour pressure of the radiating species at ambient temperature is too low.

2.3 Requirements for Substitutes and Potential Candidates

As described in section 1 it is highly desirable to find efficient substitutes for mercury in low pressure discharge lamps. However, possible substitutes for mercury in low pressure discharge lamps have to fulfil several requirements. First of all, their vapour pressure has to be considerably high as the low gas temperature only allows for cold spot temperatures between ambient temperature and a few hundred degrees centigrade. As benchmark the vapour pressure at a temperature of 300 °C should at least reach 10^{-3} mbar [KZF09]. Because of this reason the use of pure elements as radiating media (which means their emission has to be in the UV or visible spectral range) is restricted to mercury, sodium and the rare gases which already are the basis for common discharge lamps [LLLG04, KZF09]. The list of possible substitutes can be extended to molecules. In general, tri- or

polyatomic molecules have several disadvantages considering the application as radiating species. Much energy is lost in excitation processes of their manifold rovibronic states and in the variety of dissociation processes. Moreover, their emission is distributed over a very large spectral range from UV to the far infrared. These properties strongly limit the efficiency of tri- or polyatomic molecules in the lamp application. Therefore, the application of molecules as radiating species has to be restricted to diatomic molecules. Their emission spectrum is usually distributed in a smaller wavelength range and the number of rovibronic states is reduced greatly compared to polyatomic molecules. Using diatomic molecules, the molecular emission as well as the emission of the atoms of the molecule can be used due to dissociation processes in the plasma. If the diatomic species of a candidate is not stable or easily available, parent molecules that form the desired molecule by electron impact dissociation in the plasma also have to be considered.

A second requirement is the spectral range of the emission. To reduce the Stokes shift and hence the energy that is lost in the conversion process, the emission of possible candidates and at least one of the atomic components of diatomic molecules should be in the near UV or in the visible spectral range [KZF09]. Furthermore, safety standards have to be satisfied which excludes hazardous or radioactive species. It should also be noticed that the reactivity of some of the possible candidates makes the utilization of internal electrodes impossible as they would quickly be eroded. In this case, other coupling methods such as inductive or capacitive RF-coupling have to be considered. Lamps with external RF-electrodes have already been developed in several designs, some of them even suitable for common bulb fittings [Wha93, LLLG04, Lap10].

Another important aspect is that stoichiometrically driven condensation has to be avoided [KZF09]. This means for example that a species XY which emits the desired radiation has a high vapour pressure, but in the plasma the species $X_a Y_b$ is formed which immediately condensates at the wall as the vapour pressure of this compound is very low. If such a condensation occurs, a long term operation of the lamp is not possible.

Considering all these requirements, a list of 14 diatomic molecules is obtained, the majority of them being metal halides [KZF09]. These molecules are not available or stable in the diatomic form except for indium monohalides. Moreover, the use of parent molecules leads to a much more complex plasma chemistry and a considerable amount of energy is needed for the formation of the diatomic species in the plasma by electron impact dissociation which limits the efficiency (see for

example [SMM⁺07] for GaI₃ utilization for generating GaI radiation). Therefore indium monohalides are ideal candidates for fundamental investigations as they provide simplicity and a high efficiency in this point. However, for rare gas discharges containing indium halides, electrodeless RF-coupling is necessary as the halide which is formed by dissociation processes erodes internal electrodes.

2.4 Spectral and Molecular Properties of InBr and InCl

Emission Spectra of InBr and InCl Discharges

In low pressure low temperature plasmas InCl and InBr emit an intense band spectrum in the near UV spectral range. This emission arises from the transitions of the excited A ³Π₀₊(0⁺) and B ³Π₁(1) states to the ground state X¹Σ⁺(0⁺) for both indium halides as their electronic structure is the same. The A and B state are the first excited states having an excitation energy of 3.29 and 3.39 eV for InBr and of 3.44 and 3.54 eV for InCl [MYSR04]. As the excitation energy does not differ much between the two excited states the emission arising from the A – X transition overlaps strongly with the one from the B – X transition. Furthermore, InBr and InCl have small values of their molecular constants which results in a small energy difference among the vibrational or rotational states in an electronic state. Due to this reason also the emission of the single rovibrational transitions within an electronic transition overlaps strongly. Only the particular sequences - emission from transitions $v' \rightarrow v''$ with a fixed value of $\Delta v = v' - v''$ (v' denotes the vibrational quantum number of the upper electronic state and v'' the one of the lower state) - of an electronic transition can be spectroscopically resolved.

The emission spectrum of the A – X and B – X transition ranges from 350 and 400 nm for InBr whereas it is between 330 and 380 nm for InCl. Figure 2.1 shows an exemplary emission spectrum of InBr where some sequences of the electronic transitions are labelled. This spectrum results from the simulation of the relative emission intensity described in section 4.5 which allows for a separation of the emission in the A – X and the B – X transition to demonstrate the strong overlap. The exemplary emission spectrum for InCl shown in figure 2.2 also results from a simulation. For both spectra a Gaussian apparatus profile with a full width at half maximum of 23 pm has been used for the calculation.

The emission from the C ¹Π₁(1) – X¹Σ⁺(0⁺) transition is located around

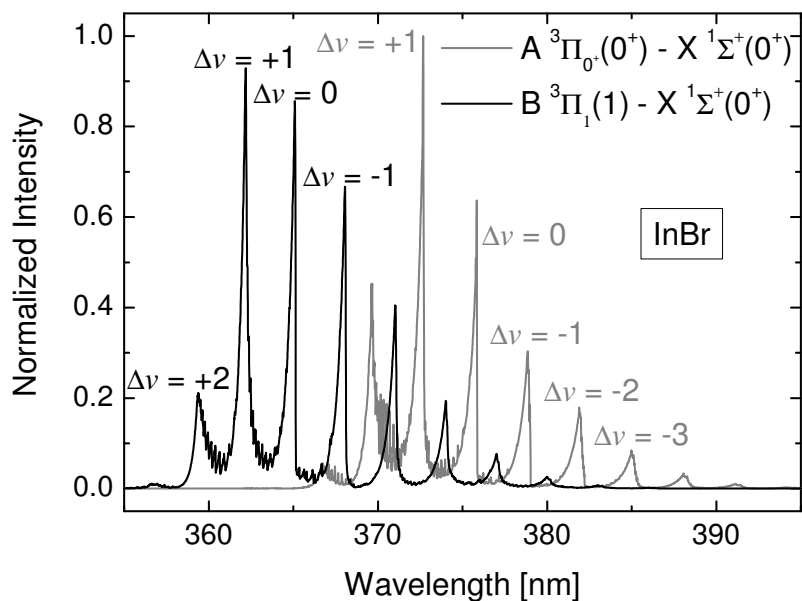


Figure 2.1: Simulated exemplary near UV emission spectrum of InBr arising from the A – X and the B – X transition. Some exemplary sequences $\Delta v = v' - v''$ are labelled. The single vibrational and rotational transitions cannot be resolved spectroscopically.

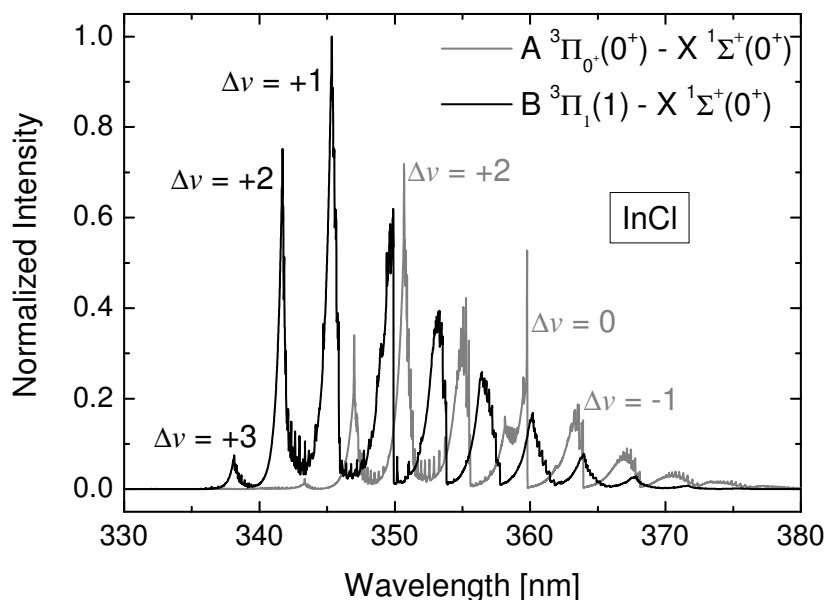


Figure 2.2: Simulated exemplary near UV emission spectrum of InCl arising from the A – X and the B – X transition. Some exemplary sequences $\Delta v = v' - v''$ are labelled. It should be noted that the wavelength and the relative intensity of the B – X transition of InCl are slightly incorrect as there is a mismatch between simulation and measurement (see section 4.5.4).

285 nm for InBr and around 270 nm for InCl [MYSR04]. However, in this work no molecular emission besides the one of the A – X and B – X transitions was detectable for both InBr and InCl in the spectral range between 250 and 1000 nm. The indium atom which is produced by dissociation processes in the plasma contributes to the emission predominantly with the emission lines at 410.2 and 451.1 nm. As the excitation energy of the states in bromine or chlorine is high, the intensity of the corresponding emission lines is negligible or not detectable.

Molecular Properties of InBr and InCl

In solid state, InBr is an orange-red salt with a density of 4960 kg/m³. Its melting point is at 290 °C [BPS55], the boiling point at 656 °C and the molecular mass is 194.72 amu [Lid05]. The InCl salt has a yellow colour and a density of 4190 kg/m³. The melting point of InCl is at 225 °C [SB58], the boiling point at 608 °C and the molecular mass is 150.27 amu [Lid05]. The natural abundance of the stable isotopes of indium, chlorine and bromine (see table 2.1) determines the isotopic composition and natural abundance of InBr and InCl which are shown in table 2.2.

Table 2.1: *Stable isotopes of indium, chlorine and bromine and their natural abundances [BLB⁺05].*

Element	Mass [amu]	Natural abundance [%]
In	113	4.29
	115	95.71
Cl	35	75.76
	37	24.24
Br	79	50.69
	81	49.31

The molecular constants of InBr and InCl [MYSR04] are summarized in the Appendix in section A. These constants determine the energy levels of the single rovibrational states as described in sections 3.2.3 and 3.2.4. A knowledge of these energy levels is required for simulating the InBr and InCl A – X and B – X emission spectra (see section 4.5). The InBr molecule has an ionization energy of 9.41 eV [BD72] and a dissociation energy of 3.99 eV [MYSR04]. The ionization energy of InCl is 9.75 eV [BD72] and the dissociation energy is 4.44 eV [MYSR04].

Several references for the vapour pressure of InBr and InCl can be found in the literature [SL60, KH07, TRBO89]. They have been determined experimen-

Table 2.2: Stable isotopes of InBr and InCl with their natural abundances (calculated after the natural abundances of indium, bromine and chlorine, see table 2.1).

Molecule	Composition	Mass [amu]	Natural abundance [%]
InBr	$^{113}\text{In}^{79}\text{Br}$	192	2.17
	$^{113}\text{In}^{81}\text{Br}$	194	2.12
	$^{115}\text{In}^{79}\text{Br}$	194	48.52
	$^{115}\text{In}^{81}\text{Br}$	196	47.19
InCl	$^{113}\text{In}^{35}\text{Cl}$	148	3.25
	$^{113}\text{In}^{37}\text{Cl}$	150	1.04
	$^{115}\text{In}^{35}\text{Cl}$	150	72.51
	$^{115}\text{In}^{37}\text{Cl}$	152	23.20

tally ([SL60, TRBO89]) or calculated theoretically ([KH07]). The corresponding vapour pressure curves differ from each other considerably (to be seen in figure 2.3). However, the optimum indium halide density which is adjusted via the cold spot temperature T_{CS} is a very important parameter that influences the discharge emission. In order to identify the cold spot temperature where the optimum efficiency is achieved the knowledge of the correct vapour pressure curve is required. A comparison of the indium halide density obtained from absorption measurements in gas phase with the density derived from the different vapour pressure curves is carried out in section 5.3 for InBr. This investigation proved that the

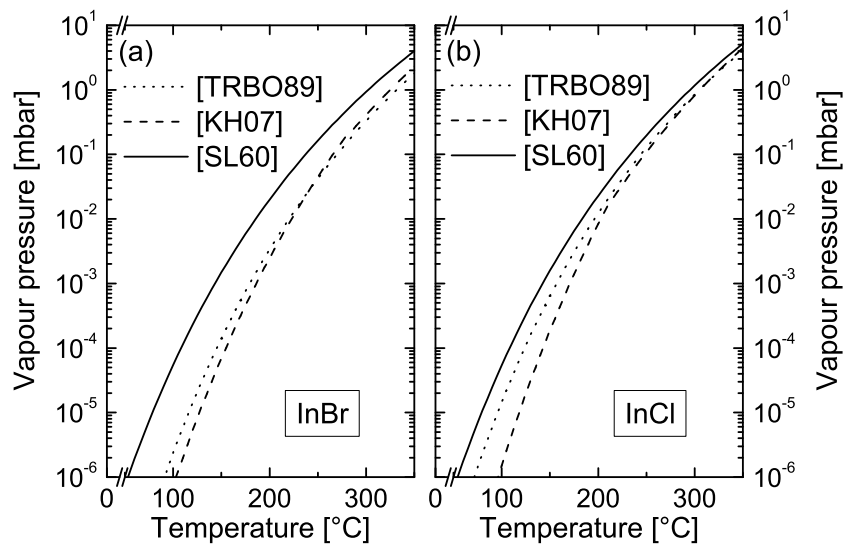


Figure 2.3: Vapour pressure curves of (a) InBr and (b) InCl calculated from the corresponding vapour pressure formulae of different references.

InBr densities calculated after the vapour pressure curve of [SL60] agrees best with the measured ones whereas the densities calculated after [KH07, TRBO89] are too small (see figure 5.7). Hence, the vapour pressure curve of reference [SL60] is used for InBr in the following. For InCl such a verification cannot be carried out as described in section 8.1. Therefore no statement about the significance of the particular vapour pressure curves of InCl can be given.

3 Properties of Low Temperature Low Pressure Plasmas

3.1 Plasma Generation and Heating Mechanisms

To generate a discharge by radio frequency (RF) heating, the RF-power can be transferred to the plasma by capacitive or inductive coupling. Further coupling methods which are based on resonant wave heating mechanisms are not discussed in this section as their application is not reasonable for lighting purposes as the lamp design would be more complex due to the required external magnetic fields. A capacitively coupled plasma (CCP, also called E-discharge) is sustained by the alternating electric field between the two electrodes of a capacitor. An inductively coupled plasma (ICP or H-discharge) is driven by an electric field that is induced by an alternating magnetic field [Lis92]. As the magnetic field is produced by a coil the ICP plasma can be compared to a single short-circuited secondary turn of a transformer. If the CCP or ICP is referred to as being “electrodeless”, the electrodes of the capacitor or the windings of the coil are separated from the plasma by a dielectric barrier. The CCP and ICP discharges are usually driven with a 50- Ω RF-power supply that operates at the typical industrial frequency of 13.56 MHz [LL94]. To assure efficient RF-coupling to the plasma, it is necessary to tune the impedance of the RF-circuit to 50 Ω resistance and zero ohms reactance. This is done by a so-called “matching network” which is introduced in the RF-circuit between the generator and the plasma.

Capacitive RF-Coupling

Using cylindrical discharge vessels, an electrodeless CCP can be realized by mounting electrodes outside the vessel at each end of the discharge tube. The advantage is that the fittings of such a lamp can be designed very similar to those of

conventional fluorescent lamps. Moreover, the electrodes do not block the radial discharge emission which is again advantageous for lighting applications.

The plasma generated by CCP discharges can be separated into three regions, the plasma volume and the two sheaths, where the bulk plasma interacts with the dielectric walls in front of each field-supplying electrode [Ben90]. The formation and the behaviour of the sheaths (which is described after [Ben90]) is mainly determined by the electrons in the plasma as their mobility is much higher (due to the smaller mass) compared to the one of the ions. If an electrode is charged positively - which is the case during one of the two RF-phases - the electrons quickly drift to the dielectric wall in front of this electrode charging the wall negatively. Due to the presence of the dielectric wall, no net charge flow can occur between the plasma and the electrodes. During the next half-cycle the electrode has a negative polarity which leads to a rejection of electrons and an attraction of ions. However, the negative wall charge cannot be neutralized completely during this RF-cycle as the mobility of the ions is lower. After several RF-cycles a sheath with a dimension of several Debye lengths between the bulk plasma and the dielectric wall is formed which has an almost stationary positive space charge. The excess negative charge at the dielectric wall leads to a positive bias of the plasma with respect to both electrodes which causes a continuous flow of ions through the sheath to the dielectric wall. This bias voltage adjusts itself in a way that the time-averaged electron and ion fluxes to the dielectric wall are equal. As this internal bias voltage can reach high values, the ions have gained high energies (up to several tens of eV [TE90], usually several times the value of T_e) when hitting the dielectric wall. These high ion energies are advantageous for plasma processing purposes like sputtering and etching but disadvantageous if one wants to avoid an erosion of the wall.

The RF-power coupled to a CCP is transferred to the electrons by ohmic heating in the bulk plasma and stochastic heating in the sheaths [LL94]. For Ohmic heating (also called collisional heating) the electric field energy is converted into thermal energy of the electrons due to collisions. If no collisions occur, the electrons move coherently with the oscillating field and no energy is transferred from the RF-field to the plasma. However, if they collide with other particles, the phase-coherent motion of the individual electron is broken. This results in an out-of-phase acceleration of the electron by the RF-field and thus in a net kinetic energy gain. In the stochastic heating process the phase-coherent motion of the electrons is broken collisionless by the reflection of the electrons at the decelera-

ting fields of the oscillating sheaths. Again, the out-of-phase acceleration leads to a net kinetic energy gain. A more detailed discussion of the heating mechanisms can be found in [LL94]. It should be noted that in some references all collisionless heating processes are referred to as stochastic heating.

Inductive RF-Coupling

An electrodeless cylindrical ICP discharge can e. g. be realized by winding a coil around a discharge tube. In general, inductive RF-coupling is more efficient compared to capacitive coupling. That provides higher electron densities and higher plasma emission at the same input power [SCC00, LL94], which is advantageous for lighting applications. But a problem in inductive coupling is the partial blocking of the radial plasma emission by the wire of the coil. A solution is the use of transparent conducting oxides such as indium tin oxide as wire material. These materials are already applied successfully as transparent electrodes in flat panel displays. Nevertheless, the basic investigations can also be carried out using a non-transparent coil.

In inductively coupled cylindrical discharges the oscillating magnetic field generated by the RF-coil is directed along the central axis of the cylinder. This magnetic field induces an oscillating electric field within the plasma which forms closed loops around the central axis [Hop92]. In general, the induction field is maximal at the plasma vessel circumference and decreases monotonically towards the central axis. However, in low pressure plasmas the occurring diffusion processes result in a radial uniform discharge despite the low induced field in the centre [Hop92]. It should be noted that the power applied to the RF-induction-coil can also cause capacitive coupling [LL94]. The low- and high-voltage ends of the coil produce a weak axial electric field through the discharge [Hop92]. This capacitive part makes an ignition of the plasma easier. Furthermore, the ICP discharge is sustained dominantly by the capacitive coupling parts especially at low power operation. This so-called E-mode has only faint emission and low electron densities [SCC00]. If the power increases, a mode transition to the H-mode with dominantly inductive coupling occurs resulting in a much higher emission and electron density. A more detailed discussion on the E-H-transition can be found in [TL99]. Of course, if inductive coupling is considered for lighting application one has to assure that the discharge is driven in H-mode.

Due to the capacitive parts of the RF-coupling, sheaths are formed at the dielectric surface of the vessel in the region of the coil-wire. However, as the ca-

capacitive coupling part is very weak, the sheath voltages are much lower compared to a CCP which also results in a much less acceleration of the ions [SCC00, LL94].

In electrodeless ICPs, the RF-power is coupled to the discharge via Ohmic heating, stochastic heating (in the E-mode) and collisionless heating (in the H-mode, also sometimes referred to as stochastic heating). Ohmic and stochastic heating have already been described in the previous section on CCP heating mechanisms. The collisionless heating in the H-mode is caused by the RF-induced spatially non-uniform and time-dependent electric field. The phase-coherent motion of the electrons travelling through the inhomogeneous field is broken if their thermal velocity is sufficiently high to sample the field inhomogeneity [SCC00, LG98]. As described above, the breaking of the phase-coherent motion leads to a net increase of the kinetic electron energy.

3.2 Population Processes, Models and Balances

If a low pressure discharge is considered for lighting purposes, it is important to gain insight in the population processes of the excited states in atoms, molecules or ions (the heavy particles) because the steady-state population density of the excited states determines the emitted radiation.

If thermal equilibrium would apply to a discharge, the population of excited states follows a Boltzmann distribution, the emitted spectral radiance is given by Planck's law and the density of the ions is given by the Saha equation. The neutral particles, the ions and the electrons all have the same kinetic energy. However, low pressure low temperature plasmas are non-equilibrium discharges, i. e. for a calculation of the population of excited states, of the emitted radiance and of the ion density all relevant processes have to be considered individually. Population models can be set up which balance the populating and depopulating processes. If the required input parameters (electron temperature, electron density, pressure, ...) are known, the steady-state population density of a desired state can be calculated numerically. These models can be used to identify the relevant population and depopulation processes or - by adjusting the calculated densities to measured ones by varying the input parameters - to determine plasma parameters like the electron temperature and density. However, the consideration of processes that involve photons can be very complex and it could be possible that relevant processes cannot be included in the model due to the lack of data on the corresponding cross sections which determine the process rates.

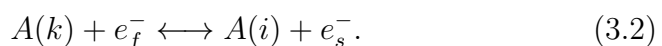
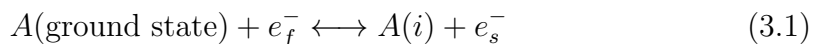
The typical electron density of low pressure discharges is in the range of $10^{14} \text{ m}^{-3} < n_e < 10^{19} \text{ m}^{-3}$ [LL94]. As a plasma is quasi-neutral the density of the positive ions times their ionization stage is equal to the electron density if the formation of negative ions can be neglected. The energy that is coupled into the plasma primarily heats the electrons as described in the previous section. Due to the large mass difference between electrons and heavy particles the energy transfer from electrons to heavy particles by elastic collisions is very ineffective. This leads to a much larger temperature of the electrons T_e which is typically in the range of several eV whereas the temperature of the neutral particles (also called gas temperature T_{gas}) and the temperature of the ions T_{ion} can only reach several times the ambient temperature [LL94]. Usually $T_{gas} \approx T_{ion}$ can be assumed as the energy transfer between neutral particles and ions is very efficient due to their similar mass.

By contrast to atoms, molecules also have vibrational and rotational states that can be excited. As the energy difference of those states is usually much smaller than the one of electronic states, different processes can populate the vibrational and rotational states. The discussion of molecular population and depopulation processes is restricted to diatomic molecules in this work, as only indium monohalides are considered.

3.2.1 Population of Electronic States

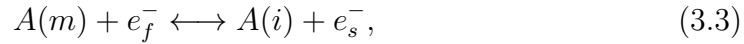
Several important excitation and deexcitation processes which determine the population density of excited electronic states in a plasma are discussed below. The listed processes shall only give a short overview of the variety of possible processes and the list does not claim completeness. It should be noted that it may be necessary to include further non-listed processes to allow for a correct characterization of the population density of an electronic state.

The energy difference between the individual electronic states of atoms, molecules and ions is usually in the range of several eV. As electrons have a high kinetic energy, the excited electronic state i of a heavy particle A is primarily populated by electron impact excitation out of the ground state or a lower state k :



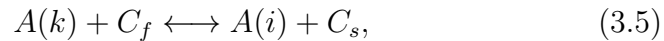
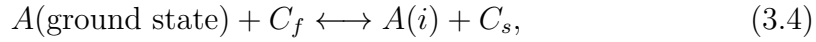
In the above processes, e_f^- and e_s^- denote a fast and a slow electron respectively.

The rate of electron impact excitation increases, if the density of the lower state in the plasma or the electron density increases. Electron impact excitation out of a metastable state m ,



can be a very important population process as metastable states usually have a high population density. The high density arises from the fact that radiative decay is not allowed for metastable states by quantum mechanical selection rules.

In general, inelastic collisions with other heavy particles C ,



do not contribute significantly to the population of excited electronic states as the heavy particles only have a low kinetic energy.

The most important deexcitation process of an excited electronic state i in low pressure low temperature plasmas is the spontaneous emission if the transition $i \rightarrow k$ is optically allowed:



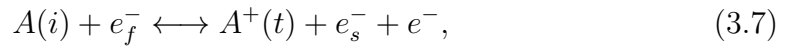
where $h\nu_{ik}$ denotes the energy of the emitted photon. If this process (which contributes to the population of the state k) proceeds over several intermediate states $i \rightarrow \dots \rightarrow k$ it is also called cascaded radiative decay.

Deexcitation processes can also occur non-radiative, for example by electron impact deexcitation (reverse process of (3.1), (3.2) and (3.3)) or by so-called quenching processes, i. e. deexcitation by heavy particle impact (reverse process of (3.4) and (3.4)). Another non-radiative deexcitation process is the diffusion of excited particles through the plasma volume to the wall of the discharge vessel where deexcitation occurs. This process is a relevant depopulation process for metastable states, as they cannot be deexcited by spontaneous emission.

The reversal process of (3.6) - the absorption of a photon - increases the population of the state i especially if the density of particles in the lower state k is considerably high in the discharge. Therefore population by reabsorption is especially important for upper states of resonant transitions or of transitions where the lower state is metastable. If the photons were emitted by the discharge itself

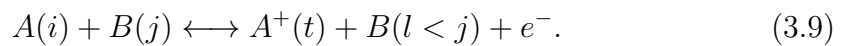
previously and are reabsorbed before they can leave the plasma, the transition is called optically thick (see section 3.3).

Due to the high kinetic energy of the electrons, ionization primarily occurs by inelastic collisions of heavy particles with electrons. Another ionization process is the absorption of a photon if the energy of the photon $h\nu$ is high enough:

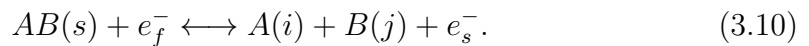


In these equations A^+ denotes the ion of the particle A which is in the electronic state t . The reversal processes of these ionization processes are the three-body-collisional recombination and the radiative recombination. However, in a low pressure low temperature plasma ions are primarily lost due to recombination at the wall of the discharge vessel. This process is described by the diffusion of ions from the bulk plasma to the wall (see next section).

A further process that leads to ionization of a particle is the so-called Penning ionization: The excitation energy of a particle B in the state j is transferred to the particle A in the state i by an inelastic collision (particle B must not necessarily differ from the particle A). The Penning ionization often involves metastable states due to their high population density. The amount of energy transferred to the particle A is enough to ionize it:



If a diatomic molecule AB is considered, dissociation occurs in the discharge. As the binding energy of the molecule is typically in the range of several eV dissociation is dominantly caused by inelastic collisions with electrons:



The potential curve of the molecular electronic state s primarily determines the resulting electronic state of the dissociation products A and B .

3.2.2 Ionization and Ambipolar Diffusion

As described in the previous section, the production of ions and electrons is dominantly caused by electron impact ionization (3.7) in low pressure low temperature plasmas. Recombination of ions and electrons in the plasma volume

(reversal reaction of (3.7) and (3.8)) can usually be neglected. Hence, the main loss process of ions and electrons is the diffusion to the wall of the discharge vessel followed by recombination at the wall. However, electrons have a much greater velocity than ions in the plasma as their mass is much smaller and their temperature is much higher. Therefore they leave the plasma much faster which leads to a charging of the wall. This generates an electric field between the wall and the bulk plasma which slows down the diffusion of the electrons and accelerates the diffusion of the ions until both fluxes are equal. This is a similar process as the formation of the sheaths in front of the electrodes of a CCP as described in section 3.1. But the potential of the sheaths caused by ambipolar diffusions is much lower compared to the CCP sheaths and they are not only located in front of the electrodes. The loss of ions caused by this so-called ambipolar diffusion is characterized by the confinement time of the ions τ_{ion} [s]. The following considerations of the diffusion are taken from [Möl93].

For very low pressures ($\lesssim 10^{-2}$ mbar) most ions directly collide with the wall due to their long mean free path length. This type of diffusion is called molecular diffusion. For higher pressures the diffusion and the confinement time of the ions are dominantly determined by collisions between the ions and heavy particles (laminar diffusion). As the pressure of the discharges investigated in this work is in the mbar range, the diffusion can be described by the laminar diffusion where the confinement time of the ions is given by

$$\tau_{ion}^{lam} = \frac{\Lambda^2}{D_a} \quad \text{with} \quad D_a = \frac{3\sqrt{\pi}}{8} \frac{T_e}{T_{gas}} \lambda_{ion} \sqrt{\frac{k_B T_{gas}}{m_{ion}}}, \quad (3.11)$$

with the ambipolar diffusion coefficient D_a [m²/s], the mean free path length of the ions λ_{ion} [m], the Boltzmann constant k_B [J/K] and the ion mass m_{ion} [kg]. For the equation which yields D_a it is assumed that $T_{ion} \approx T_{gas} \ll T_e$ which are all given in [K]. The mean diffusion length of the ions in a cylindrical plasma Λ [m] is determined by the radius r [m] and the length L [m] of the cylinder:

$$\frac{1}{\Lambda^2} = \left(\frac{2.405}{r}\right)^2 + \left(\frac{\pi}{L}\right)^2. \quad (3.12)$$

Due to the ambipolar diffusion of electrons and ions to the wall their density usually follows a radially symmetric profile in cylindrical plasma geometries where the maximum density is at the central axis [Beh91]. This profile can be described by a zero-order Bessel function.

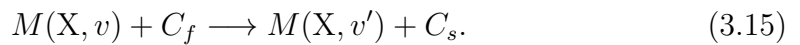
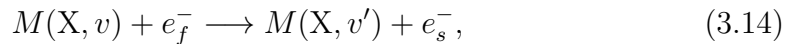
3.2.3 Population of Vibrational States in Molecules

The energy $G(v)$ (traditionally given in $[\text{cm}^{-1}]$) of a vibrational state with quantum number v in a molecular electronic state can be calculated as

$$G(v) = \omega_e \left(v + \frac{1}{2} \right) - \omega_e x_e \left(v + \frac{1}{2} \right)^2 + \omega_e y_e \left(v + \frac{1}{2} \right)^3 - \dots, \quad (3.13)$$

where ω_e , $\omega_e x_e$ and $\omega_e y_e$ (all given in $[\text{cm}^{-1}]$) denote molecular constants [Her50].

In general, the energy difference between the vibrational states is much smaller than the difference between electronic states. Hence, the kinetic energy of a heavy particle C can be sufficient to contribute to the vibrational population. Therefore the particular vibrational states in the electronic ground state X of a molecule M can be populated by electron or heavy particle impact excitation:



where the energy of the vibrational state v is smaller than the one with vibrational quantum number v' . The vibrational population of the electronic ground state of diatomic molecules in low pressure low temperature plasmas can typically be described by a sum of two Boltzmann distributions [Sob89] each characterized by a different vibrational temperature T_{vib} [K]. One temperature characterizes the population by inelastic collisions with electrons (but it does not necessarily have to be equal to T_e) and the other one characterizes the population by inelastic heavy particle collisions (which can be equal to the gas temperature) [Sob89]. Usually, the vibrational population is determined by a mixture of both processes.

Excited electronic molecular states are primarily populated by electron impact excitation out of lower electronic states (usually the ground state or a metastable state) as shown in section 3.2.1. Accompanying the electronic excitation a redistribution of the vibrational population can occur which is described by the so called Franck-Condon principle [Her50, Ber05]. As the electronic excitation takes place on a much shorter time scale than the oscillation of the two atoms of the diatomic molecule the internuclear distance r can be considered constant during the excitation process (Born-Oppenheimer approximation). The probability for a vibrational transition during the electron impact excitation is described by the

overlap integral of the wavefunctions of the vibrational states v' and v'' :

$$q_{ik}^{v'v''} = \left| \int_0^{\infty} \Psi_i^{v'*}(r) \Psi_k^{v''}(r) dr \right|^2, \quad (3.16)$$

where $\Psi_i^{v'}$ [$1/\sqrt{m}$] denotes the wavefunction of the vibrational state v' in the upper electronic state i and $\Psi_k^{v''}$ the one of the vibrational state v'' in the lower electronic state k . Due to the normalization of the wavefunctions the value of the so called Franck-Condon factor $q_{ik}^{v'v''}$ ranges from zero to unity. As the vibrational population of an excited electronic state strongly depends on the Franck-Condon factors it can differ heavily from a Boltzmann distribution which means it cannot be described by a temperature in contrast to the vibrational population of the electronic ground state. However, if the lifetime of the excited vibronic states greatly exceeds the average time between the inelastic collisions (3.14) & (3.15) the vibrational population can be redistributed. This is the case for metastable molecular states, for example. The vibrational population of such states might again be described by a sum of two Boltzmann distributions.

The most important deexcitation process, the spontaneous emission, can be described in molecules with vibrationally resolved transition probabilities $A_{ik}^{v'v''}$ [s^{-1}] for transitions $i, v' \rightarrow k, v''$. They are given by

$$A_{ik}^{v'v''} = \frac{16}{3} \frac{\pi^3}{\epsilon_0 h \lambda_0^3} \left| \int_0^{\infty} \Psi_i^{v'*}(r) D_{el}(r) \Psi_k^{v''}(r) dr \right|^2, \quad (3.17)$$

where ϵ_0 [C/(V m)] denotes the permittivity constant, h [J s] the Planck constant, λ_0 [nm] the central wavelength of the transition and $D_{el}(r)$ [C m] the electronic dipole transition moment [Her50, Ber05]. The spontaneous emission is not restricted by quantum mechanical selection rules concerning the values of v' and v'' .

It should be noted that the discussed processes again only represent the most important ones. Many other processes as e. g. recombination or dissociation may populate or depopulate special vibrational states preferably and can have a considerable influence on the vibrational population [Sob89].

3.2.4 Population of Rotational States in Molecules

The energy $F_v(J)$ (traditionally given in [cm^{-1}]) of the particular rotational state in a vibronic state with vibrational quantum number v can be calculated with

the molecular constants B_e , D_e , H_v , α and β (all given in $[\text{cm}^{-1}]$) after [Her50]:

$$F_v(J) = B_v J(J+1) - D_v [J(J+1)]^2 + H_v [J(J+1)]^3 - \dots \quad (3.18)$$

$$\text{with } B_v = B_e - \alpha \left(v + \frac{1}{2} \right) + \dots \quad \text{and} \quad D_v = D_e + \beta \left(v + \frac{1}{2} \right) + \dots$$

The energy difference between the single rotational states is very small (much smaller than the one between the vibrational states). Therefore the rotational population of a vibrational state v in the electronic ground state of a molecule M is determined by inelastic collisions with heavy particles C that have enough kinetic energy for the rotational excitation [Her50, Sob89]:



In general, electron impact excitation can be neglected as much more inelastic collisions with heavy particles occur (due to the higher density) than with electrons. The rotational population of the electronic ground state can usually be described with a Boltzmann distribution [Her50] characterized by the rotational temperature T_{rot} [K] [Sob89]. This rotational temperature is equivalent to the gas temperature of the plasma if the energy difference between the single rotational states is much lower than the value of $k_B T_{gas}$ [Sob89, AKK⁺96].

The rotational population of the ground state is transferred to the excited electronic molecular states via electron impact excitation. During this process a rotational redistribution occurs if the angular momentum of the electronic state changes as the rotational quantum number also have to change due to the conservation of the angular momentum. A Boltzmann distribution can usually still describe the rotational population in the excited electronic state but the rotational temperature may be different from the one of the ground state. If the energy difference ΔE_{rot} between the single rotational states is very small or the radiance lifetime of the excited state is long (which both increases the rate of inelastic heavy-particle collisions), a redistribution of the rotational population in the excited vibronic state occurs. If this is the case, the rotational temperature coincides again with the gas temperature of the plasma if $\Delta E_{rot} \ll k_B T_{gas}$ holds.

As described in section 3.2.1 the main deexcitation process of excited electronic states is spontaneous emission (if the upper state is not metastable). The transition from an excited electronic state with rotational quantum number J' into a lower state with J'' is restricted to $\Delta J = J' - J'' = 0, \pm 1$ due to quantum me-

chanical selection rules. The probability of such a transition is described by the so called Hönl-London factors [Her50]. These factors depend on the Hund's coupling cases valid in the upper and lower electronic state, the quantum numbers of these states and on constants that describe possible perturbations [Kov69]. The equations for almost any possible electronic transition can be found in [Kov69].

3.2.5 Corona Model and Collisional-Radiative Model

At low electron densities ($n_e \lesssim 10^{16} \text{ m}^{-3}$) the corona model can be used to describe the population of excited electronic states. This model is named after the corona of the sun which is a plasma with high electron temperatures and very low electron densities. The low value of n_e leads to a low rate regarding all population and depopulation processes involving electrons. Nevertheless, the main excitation process is electron impact excitation out of the ground state (3.1) as only electrons have enough kinetic energy to allow for excitation processes. Due to the low rate of inelastic collisions involving electrons the excited electronic states are populated to a much lower extent compared to the Boltzmann distribution. This makes the population of excited states by radiative decay from higher states (3.6) or electron impact excitation out of excited states (3.2) negligible. Reabsorption of a photon (reversal reaction of (3.6)) can also be neglected as population process as the mean free path of the photons is long. Again as the electron impact excitation rate is low, the average time between inelastic electron – heavy-particle collisions is much larger than the radiance lifetime of an excited state i . Therefore in the corona model the main excitation process, electron impact excitation, is balanced with spontaneous emission to lower states k as the main deexcitation process:

$$\underbrace{n_1 n_e X_{1i}(T_e)}_{\text{electron impact excitation}} = n_i \underbrace{\sum_{k < i} A_{ik}}_{\text{spont. emission}} . \quad (3.20)$$

$A_{ik} [\text{s}^{-1}]$ denotes the transition probability and $X_{1i}(T_e) [\text{m}^3/\text{s}]$ the rate coefficient for electron impact excitation out of the ground state into the excited state. The density of the ground state $n_1 [\text{m}^3]$ can be assumed to equal the particle density n_0 of the considered species as the amount of excited or ionized particles is very low. If n_e and T_e are known, the density $n_i [\text{m}^3]$ of the excited state can be calculated:

$$n_i = \frac{n_0 n_e X_{1i}(T_e)}{\sum_{k < i} A_{ik}} . \quad (3.21)$$

The required rate coefficient $X_{1i}(T_e)$ can be calculated with the corresponding cross section for electron impact excitation $\sigma_{1i}(E)$ [m²] by integrating the product of $\sigma_{1i}(E)$, the velocity of the electrons $v_e(E) = \sqrt{2E/m_e}$ [m/s] and the electron energy distribution function (EEDF) $f(E, T_e)$ [1/J] over the energy from the threshold energy of the excitation process E_{exc} [J] to infinity:

$$X_{1i}(T_e) = \int_{E_{exc}}^{\infty} \sigma_{1i}(E) \sqrt{2E/m_e} f(E, T_e) dE. \quad (3.22)$$

The electron energy distribution function is usually approximated by a Maxwellian distribution, which assumes that the electrons thermalize among themselves. This distribution is characterized by the electron temperature T_e :

$$f(E, T_e) dE = \frac{2}{\sqrt{\pi}} \frac{\sqrt{E}}{(k_B T_e)^{3/2}} \exp\left(-\frac{E}{k_B T_e}\right) dE. \quad (3.23)$$

However, the RF-heating of the electrons (described in section 3.1) can result in a non-Maxwellian EEDF. Furthermore, in the pressure range of mbar the frequency of inelastic electron – heavy-particle collisions is typically high enough to obtain substantial deviations from a Maxwellian distribution. In this case an electron temperature cannot be defined. Nevertheless, T_e can be used to characterize other EEDFs by relating it with the average electron energy $\langle E_e \rangle$ [eV]:

$$\langle E_e \rangle = \frac{3}{2} k_B T_e. \quad (3.24)$$

If a metastable electronic state exists between the ground state and the considered state i , the density of the metastable state can reach notable values despite the low n_e -value. Hence electron impact excitation out of the metastable state m (3.3) must also be considered in the population processes of the state i resulting in:

$$n_0 n_e X_{1i}(T_e) + n_m n_e X_{mi}(T_e) = n_i \sum_{k < i} A_{ik}. \quad (3.25)$$

In this extended corona model the population of the state i is given by

$$n_i = \frac{n_0 n_e X_{1i}(T_e) + n_m n_e X_{mi}(T_e)}{\sum_{k < i} A_{ik}}. \quad (3.26)$$

The corona model can only be applied if all other excitation and deexcitation processes besides electron impact excitation and spontaneous emission of

the considered state can be neglected. Therefore the validity of the corona model is usually restricted to very special cases. If additional processes as for example collisional deexcitation by electrons, radiative decay from higher states or absorption of photons have to be considered, a collisional-radiative model has to be set up. This model balances all relevant population and depopulation processes of a state numerically. However, this requires a detailed knowledge of cross sections and transition probabilities which are often not available in the literature.

3.2.6 Ionization Balance and its Impact on T_e

As described in section 3.2.2 the ionization of atoms or molecules in the plasma is dominated by inelastic collisions with electrons whereas the main loss mechanism of ions is their diffusion to the wall of the discharge vessel. Balancing these two processes yields

$$\underbrace{n_e n_0 X_{1, ion}(T_e)}_{\text{electron impact ionization}} = \underbrace{n_{ion} (\tau_{ion}^{lam})^{-1}}_{\text{laminar diffusion}}, \quad (3.27)$$

where n_0 [m³] is the density of the considered species, n_{ion} [m³] is the ion density and $X_{1, ion}(T_e)$ [m³/s] denotes the rate coefficient for electron impact ionization out of the ground state. In the above equation the assumption is made that only singly charged ions occur. $X_{1, ion}(T_e)$ can be calculated with the cross section for electron impact ionization $\sigma_{1, ion}(T_e)$ [m²] analogue to equation (3.22). If quasi-neutrality is applied, n_e equals n_{ion} and equation (3.27) reduces to

$$X_{1, ion}(T_e) = \frac{1}{n_0 \tau_{ion}^{lam}}. \quad (3.28)$$

With equation (3.11) which describes the confinement time of the ions in the laminar diffusion regime τ_{ion}^{lam} [s] it follows

$$X_{1, ion}(T_e) \propto \frac{\lambda_{ion}}{n_0 \sqrt{m_{ion}}}, \quad (3.29)$$

where the linear dependence of τ_{ion}^{lam} on T_e is neglected as the dependence of $X_{1, ion}$ on the electron temperature is much stronger. This means the steady-state electron temperature of the discharge is determined by the pressure (via n_0 and the mean free path length λ_{ion}), the ion mass and the rate coefficient for electron impact ionization. Some qualitative dependencies of the electron temperature on these parameters can be derived:

- The smaller the ionization energy of the ion (and therefore the larger the ionization rate coefficient), the lower is the electron temperature of a plasma as the ionization balance must be fulfilled.
- The smaller the pressure (and therefore n_0), the larger is the mean free path length λ_{ion} of the ion. This results in an increasing T_e .
- If the rate coefficient for electron impact ionization is the same for two ions but the mass of the ion differs, the electron temperature is smaller in the discharge with the heavier ion.

If different species of ions j occur in the plasma ($n_e = \sum_j n_{ion}^j$ always has to be fulfilled) the ionization balance of equation (3.27) has to be extended:

$$n_e \sum_j n_j X_{1, ion}^j(T_e) = \sum_j n_{ion}^j (\tau_{ion}^j)^{-1}. \quad (3.30)$$

Qualitative dependencies of T_e are now much more difficult to derive as the contributions of the particular ions cannot be considered separately.

For InBr(InCl)/rare gas discharges the following species have to be considered in the ionization balance: indium, bromine (chlorine), InBr (InCl) and the background gas. The rate coefficients for electron impact ionization out of the ground state of indium, bromine, chlorine, InBr and InCl are shown in figure 3.1. All rate coefficients have been calculated according to equation (3.22) assuming a Maxwellian EEDF. The required cross sections are taken from [SWF89] for indium and from [HWF87] for bromine and chlorine. As the cross sections for the ionization of InBr and InCl is not available in the literature they were estimated using the Gryzinski-method as described in [BD65] (see figure A.1 in the appendix for the obtained cross section).

Besides electron impact ionization out of the ground state, additional ionization processes such as electron impact ionization out of excited states (especially out of metastable states) may play an important role in the ionization balance. In general, the excitation energy of excited electronic states is only slightly below the ionization energy. Therefore the threshold energy for electron impact ionization out of excited states is reduced considerably compared to the ionization out of the ground state which results in a much higher rate coefficient. This is shown exemplarily for the rate coefficients for ionization out of the argon 1s and 2p states in figure 3.22 (see figure 4.6 for a energy level diagram for argon). The corresponding cross sections have been taken from [WBHF87] and [Hym79].

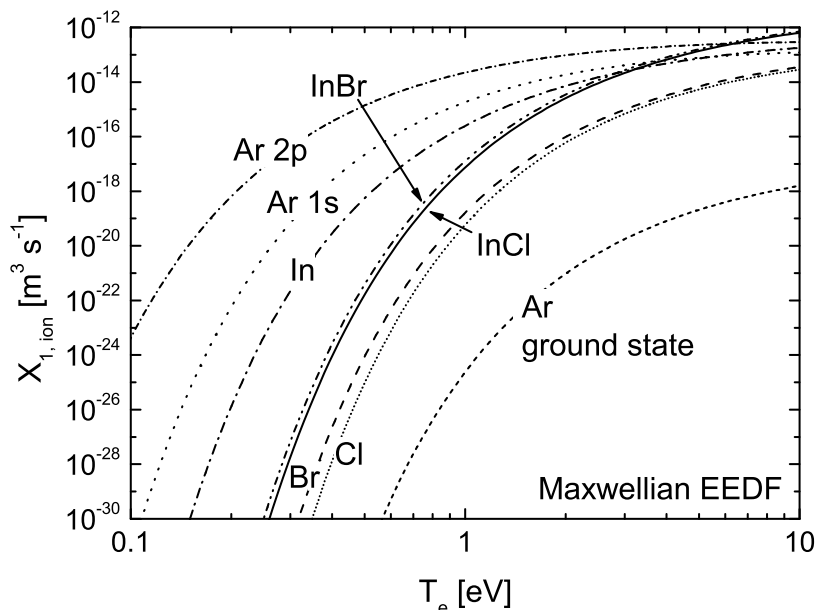


Figure 3.1: Rate coefficients for electron impact ionization out of the ground state. For argon the rate coefficients for ionization out of the ground state, out of the 1s states and out of the 2p states are shown.

Such additional ionization processes can provide an important contribution to the ionization balance despite the lower population density of the excited states compared to the density of the ground state. However, for the species relevant for indium halide/rare gas discharges the cross sections for ionization out of excited electronic states are mostly not available in the literature which makes a consideration of these processes in the ionization balance impossible.

Even if additional processes beside electron impact ionization out of the ground state are neglected, a quantitative evaluation of the ionization balance still requires the knowledge of all ion densities. As emission or absorption signals arising from ions could not be detected in the investigated discharges, ion densities could not be determined. Hence the impact of varying plasma parameters on the ionization balance and in turn on the electron temperature can only be described in a qualitative way.

3.2.7 Power Balance and its Impact on n_e

The electrical power P [W] supplied to a plasma basically heats the electrons as described in section 3.1. In steady-state P is balanced by several loss channels. The discussion in this section is restricted to the power balance of the bulk plasma,

whereas the power distributed to (or lost in) electrode regions or RF-sheaths are not considered. For the bulk plasma, typically only a small amount of energy is lost to the wall by convection (increasing the wall temperature) or transferred to the neutral heavy particles by elastic collisions (increasing the gas temperature) [Beh91]. However, in special applications, e. g. the low pressure sodium lamp as described in section 2.2, these loss channels can be enhanced explicitly by using a light-weight gas and/or a high pressure to increase the gas temperature and the wall temperature of a discharge. In general, the main power consuming processes are inelastic collisions which lead to an excitation, ionization or, in the case of molecules, to dissociation of the heavy particles:

$$P = P_{excitation} + P_{ionization} + P_{dissociation}. \quad (3.31)$$

If it is assumed that only species in the ground state, only one possible singly charged ion and only one possible dissociation energy exists, the power losses are given by

$$P_{excitation} = V_{plasma} n_e n_0 \sum_J X_{1J}(T_e) E_J, \quad (3.32)$$

$$P_{ionization} = V_{plasma} n_e n_0 X_{1, ion}(T_e) E_{ion}, \quad (3.33)$$

$$P_{dissociation} = V_{plasma} n_e n_0 X_{1, diss}(T_e) E_{diss}. \quad (3.34)$$

In the above equations V_{plasma} [m³] is the plasma volume, E_J , E_{ion} and E_{diss} [J] are the threshold energies for electron impact excitation to the state J , for ionization and for dissociation [Beh91]. X_{1J} , $X_{1, ion}$ and $X_{1, diss}$ denote the corresponding rate coefficients. This yields

$$P = V_{plasma} n_e n_0 X_{1, ion}(T_e) \left[\frac{\sum_J X_{1J}(T_e) E_J}{X_{1, ion}(T_e)} + E_{ion} + \frac{X_{1, diss}(T_e) E_{diss}}{X_{1, ion}(T_e)} \right]. \quad (3.35)$$

Substituting $n_e n_0 X_{1, ion}(T_e)$ after equation (3.27) and applying $n_e = n_{ion}$ gives

$$P = \frac{V_{plasma} n_e}{\tau_{ion}^{lam}} \left[\frac{\sum_J X_{1J}(T_e) E_J}{X_{1, ion}(T_e)} + E_{ion} + \frac{X_{1, diss}(T_e) E_{diss}}{X_{1, ion}(T_e)} \right]. \quad (3.36)$$

If only atoms are present in the discharge, dissociation processes do not occur and the number of excited states is greatly reduced as only electronic states i occur. In general, the energy levels of excited states in atoms are close to the ionization energy ($E_i \lesssim E_{ion}$) and the sum over the ionization rate coefficients for excitation

is in the order of the ionization rate coefficient [Beh91]. This results in almost equal energy losses due to excitation and ionization in atomic plasmas. As the ratio of the rate coefficients for ionization and excitation is almost independent on T_e and can therefore be considered constant, the value of $V_{plasma}n_e$ is proportional to the electrical input power and the confinement time [Beh91]:

$$V_{plasma}n_e \propto P\tau_{ion}^{lam}. \quad (3.37)$$

In molecular discharges, dissociation and the excitation of vibrational and rotational states increase the number of possible energy loss channels greatly compared to atomic discharges. Therefore, the generation of molecular discharges requires more power in general. The excitation of the variety of rovibronic states J can dominate the whole energy balance leading to

$$P \approx V_{plasma}n_en_0 \sum_J X_{1J}(T_e)E_J. \quad (3.38)$$

Rewriting the equation yields

$$V_{plasma}n_e \approx \frac{P}{n_0 \sum_J X_{1J}(T_e)E_J}. \quad (3.39)$$

From equation (3.37) for atomic and equation (3.39) for molecular discharges the following qualitative statements on the dependencies of $V_{plasma}n_e$ on external (pressure, input power) and internal plasma parameters (T_e , m_{ion}) can be drawn:

- The higher the electrical input power, the larger is the value of $V_{plasma}n_e$.
- In atomic discharges, a higher pressure leads to a larger value of $V_{plasma}n_e$. This dependence follows implicitly from the smaller mean free path length λ_{ion} at higher pressure. After equation (3.11) this results in a larger value of τ_{ion}^{lam} which in turn leads to the larger value of $V_{plasma}n_e$ according to equation (3.37). The situation is different in molecular discharges. An increase of pressure results in an increase of the particle density n_0 after the ideal gas law if the gas temperature is assumed to be constant. According to equation (3.39) this leads to a decrease of $V_{plasma}n_e$. It should be noted that in general a high pressure results in a considerable importance of energy losses by elastic collisions which have been neglected in equation (3.31). These processes lead to a decrease of $V_{plasma}n_e$ with increasing pressure.
- If two atomic discharges with differing ion mass are considered, the value

of $V_{plasma}n_e$ is larger in the discharge with the heavy-weight ion as its confinement time is larger than the one of the light-weight ion. For molecular discharges, $V_{plasma}n_e$ is independent of the confinement time of the ion and therefore also independent of the ion mass.

- In atomic discharges an increase of T_e results in a decrease of $V_{plasma}n_e$ as τ_{ion}^{lam} is indirectly proportional to the electron temperature according to equation (3.11). However, in molecular discharges an increase of T_e results in an increase of $V_{plasma}n_e$ due to the strictly monotonically increasing dependence of the rate coefficient on T_e .

As the power balance has to be fulfilled in steady-state, a change of the above described parameters has a direct influence on the value of the plasma volume times the electron density. If the plasma volume stays constant (this is for example the case if the whole discharge vessel is already filled with plasma) a change of these parameters changes the electron density. On the other hand side, a change of these parameters can also result in a change of the plasma volume (if the discharge vessel allows for it) resulting in a constant electron density.

If the power balance of InBr(InCl)/rare gas discharges is set up, the presence of indium, bromine (chlorine) and of the diatomic molecule InBr (InCl) in the discharge have to be considered besides the rare gas. Hence, the power losses due to dissociation and excitation of rovibrational states of the indium halide molecule have to be considered. However, the energy difference between the particular rotational and vibrational states of InBr and InCl is very small due to the small molecular constants (see section 2.4). The excitation energy of an excited rovibronic state can be approximated by the excitation energy of the electronic state neglecting the additional rovibrational excitation energy, i. e. the excitation of InBr and InCl can be treated as atomic excitation. This is advantageous for lighting purposes as the energy loss via rovibrational excitation processes is very small which provides more energy for excitation processes of electronic states and thus a better efficiency of generating radiation. Nevertheless, the power loss by dissociation processes has to be included in the power balance besides the power losses by ionization and excitation.

Many cross sections are required to calculate the rate coefficients for excitation of the particular species and for the dissociation of the indium halide molecule. This data is not available in the literature especially for InBr and InCl. Thus the impact of the discharge parameters on the power balance and in turn on n_e can only be discussed qualitatively for rare gas discharges containing InBr or InCl.

3.3 Opacity and Radiation Transport

If a considerable amount of radiation emitted by the plasma is reabsorbed before the photons leave the plasma volume, the radiation is referred to as optically thick or opaque. This effect plays an important role in low pressure discharges for lighting applications, as it limits the efficiency as described for the mercury radiation of fluorescent lamps in section 2.1. Furthermore, the absorption of radiation in the plasma is a population process as described in section 3.2.1. Therefore the reabsorption effect has to be considered for optically thick transitions in population models (see section 3.3.2).

In low pressure low temperature plasmas the population density of the upper state i of a transition is usually much smaller than the one of the lower state k . Therefore stimulated emission can be neglected. The radiance of an emission line $L_{ik}(l)$ [W/(m² sr)] that is transported through the plasma along a line of sight with length l ($0 \leq x \leq l$) is given by

$$L_{ik}(l) = \int_{line} L(\lambda, l) d\lambda = \int_{line} \int_0^l \underbrace{\epsilon(\lambda, x)}_1 \underbrace{\exp[-(l-x)\alpha(\lambda, x)]}_2 dx d\lambda, \quad (3.40)$$

assuming $L_{ik}(0) = 0$ [Beh98]. $L(\lambda, l)$ [W/(m² nm sr)] denotes the spectral radiance of the plasma, $\epsilon(\lambda, x)$ [W/(m³ nm sr)] the spectral emission coefficient, $\alpha(\lambda, x)$ [nm⁻¹] the spectral absorption coefficient and the variable x a position along the line of sight. As the wavelength λ is given in [nm] also x and l have the unit [nm]. Part 1 of the equation contains the emission generated at position x . Part 2 contains the fraction of the emitted radiation at x that is absorbed along the remaining length $l - x$ of the line of sight. The absorbed amount of radiation is usually emitted again in arbitrary direction, i. e. it can be considered lost.

The spectral emission coefficient $\epsilon(\lambda, x)$ of a single transition can be expressed by the line emission coefficient $\epsilon_{ik}(x)$ [W/(m³ sr)] and the line profile $P_{line}^{ems}(\lambda)$ [nm⁻¹] which is normalized to $\int_{line} P_{line}^{ems}(\lambda) d\lambda = 1$:

$$\epsilon(\lambda, x) = \epsilon_{ik}(x) P_{line}^{ems}(\lambda) = \frac{n_i(x) A_{ik} hc}{4\pi \lambda_0} P_{line}^{ems}(\lambda) \quad (3.41)$$

with the population density of the upper state n_i , the transition probability A_{ik} , the velocity of light c [m/s] and the central wavelength of the transition λ_0 [Tho88]. The spectral absorption coefficient of a single absorption line is given by the line absorption coefficient $\alpha_{ik}(x)$ and the absorption line profile $P_{line}^{abs}(\lambda)$

[nm⁻¹] which is normalized to $\int_{line} P_{line}^{abs}(\lambda) d\lambda = 1$:

$$\alpha(\lambda, x) = \alpha_{ik}(x) P_{line}^{abs}(\lambda) = \frac{\lambda_0^4}{8\pi c} \frac{g_i}{g_k} A_{ik} n_k P_{line}^{abs}(\lambda) \quad (3.42)$$

with the population density of the lower state n_k and the statistical weights g_i and g_k [Tho88]. Assuming that the absorption is constant along the line of sight, i. e. $\alpha_{ik}(x) \hat{=} \alpha_{ik}$ yields

$$L_{ik}(l) = \int_{line} \int_0^l \epsilon_{ik}(x) P_{line}^{ems}(\lambda) \exp[(x-l) \alpha_{ik} P_{line}^{abs}(\lambda)] dx d\lambda. \quad (3.43)$$

Hence the radiation of an emission line escaping from the plasma along a line of sight with length l depends on the line emission and the absorption coefficient as well as on the emission and absorption line profile.

3.3.1 Line Profiles

Several effects contribute to the profile of an emission or absorption line in a low pressure low temperature plasma: natural line broadening, Doppler broadening and the broadening due to collisions of the radiating particle with surrounding perturbers. A detailed description of these effects can be found in [Tho88, Gri64, SVY81] or [LH68]. This section only gives a short overview and describes the calculation methods of the full width at half maximum (FWHM) of the line profile for the different line broadening mechanisms.

As the excited state of an optically allowed transition has a finite lifetime the energy of the state and therefore of the emitted or absorbed photon is not well-defined due to the energy-time uncertainty principle. This results in natural line broadening. The FWHM ω_{nat} [nm] of its Lorentzian emission line profile with central wavelength λ_0 is determined by the lifetime of the upper state τ_i [s] and the one of the lower state τ_k [s] that participate in the transition:

$$\omega_{nat} = \frac{\lambda_0^2}{c} \left(\frac{1}{2\pi\tau_i} + \frac{1}{2\pi\tau_k} \right). \quad (3.44)$$

If the lower state is metastable or the ground state its contribution to ω_{nat} can be neglected as $\tau_i \ll \tau_k$.

Doppler broadening is caused by the thermal motion of the radiating particles and the Doppler effect. Different velocities lead to different Doppler shifts of

the wavelength of the emission line. The Maxwellian velocity distribution of the emitting particles leads to a Gaussian profile with a FWHM $\omega_{Doppler}$ [nm] given by

$$\omega_{Doppler} = 2\lambda_0 \sqrt{\frac{2k_B T_{gas} \ln 2}{mc^2}}, \quad (3.45)$$

where m [kg] denotes the mass of the radiating particle.

The broadening due to collisions has to be separated into two cases: collisions with neutral particles (pressure broadening) and with charged particles (Stark broadening). In both cases these interactions lead to a perturbation of the energy levels of the radiating species which causes the broadening. Pressure broadening results in a Lorentzian line profile and a linear dependence of the FWHM on the pressure. The constants that describe the linear dependence (the slope is also called broadening coefficient) are determined by the interaction potential between the radiator and the surrounding particles which is different for each transition. The FWHM $\omega_{pressure}$ is traditionally given in spectroscopic notation [cm^{-1}] and determined by

$$\omega_{pressure} = N \left(\frac{\gamma}{N} \right), \quad (3.46)$$

where N [cm^{-3}] is the density of the collision partner and γ/N the broadening coefficient [$10^{-20} \text{ cm}^{-1} \text{ cm}^3$] which can be found in the literature. However, in this work the wavelength is usually given in [nm], therefore also $\omega_{pressure}$ is given in [nm] in the following (the conversion can easily be performed). Stark broadening results in a Holtsmark profile whose FWHM can be calculated after [LH68]:

$$\begin{aligned} \omega_{Stark} &= 2 \times 10^{-16} \omega' n_e (1 + 1.75 \times 10^{-4} \bar{\alpha} q n_e^{1/4}) \\ \text{with } q &= 1 - 0.068 n_e^{1/6} T_e^{-1/2}, \end{aligned} \quad (3.47)$$

where n_e is the electron density (in cm^{-3}) and T_e the electron temperature (in K). The units of the constant factors in this equation can be chosen in a way that the resulting unit of ω_{Stark} is [nm]. Tabulated values of the ion broadening parameter $\bar{\alpha}$ and the FWHM ω' for an electron density of 10^{16} cm^{-3} can be found in the literature, for example in [Gri74]. In general, the Holtsmark line profile is similar to a Lorentzian line profile, therefore Stark broadening is approximated by a Lorentzian profile in this work.

In summary, the line profile is dominated by Doppler broadening around the central wavelength λ_0 in low pressure plasmas [Tho88]. The FWHM of collisional broadening due to charged and uncharged particles and the FWHM of natural line

broadening is typically several orders of magnitude lower [Tho88]. However, the Lorentzian profile decreases much more slowly in the wings of the line compared to a Gaussian profile, i. e. the wings of the line profile are dominated by the Lorentzian profile. Considering all broadening effects results in a Voigt profile which is a convolution of the Lorentzian and Gaussian profiles.

3.3.2 The Escape Factor Concept

The absorption of radiation in the plasma is a population process of the upper state of the transition as described in section 3.2.1. Therefore an optically thick transition results in an increase of the population density of the upper state. This effect can be considered by treating the absorption as negative emission, i. e. subtracting the absorption from the emission [Iro79]. Hence the opacity effect is referred to as a reduction of the transition probability A_{ik} by introducing a value Θ which ranges from zero to unity and is called escape factor [Hol47, Hol51]. The transition probability of an optically thick emission line is then given as $A_{ik}\Theta$ [s^{-1}]. The escape factor has to be derived individually for each application. One application is the consideration of the reduction of the escaping radiation by opacity effects in optical emission spectroscopy. If the radiation transport along the line of sight through the plasma is calculated, a so-called line escape factor Θ_{line} is yielded. This factor describes the fraction of the reabsorbed radiation which allows for a correction of the density obtained from the spectroscopic measurement (see section 4.1.2). Another application is the consideration of reabsorption of radiation as population process in collisional-radiative models, where the radiation transport of the surrounding plasma along all possible line of sights to one point within the plasma is considered. This escape factor is called population escape factor and its calculation is described in the next section.

Calculation of Population Escape Factors

Opacity effects are taken into account in collisional-radiative models by a so-called population escape factor Θ_{pop} . This escape factor is given by the relative difference between the emitted and the absorbed radiation at the relevant plasma

location y [Beh98]:

$$\begin{aligned}\Theta_{pop} &= \frac{\text{emitted radiation at } y - \text{absorbed radiation at } y}{\text{emitted radiation at } y} \\ &= 1 - \frac{\text{absorbed radiation at } y}{\text{emitted radiation at } y}.\end{aligned}\quad (3.48)$$

To obtain the emitted radiation of a single transition at position y , an integration of the isotropic spectral emission coefficient over the wavelength range of the emission line and over the solid angle Ω [sr] has to be carried out:

$$\text{emitted radiation at } y = \int_{\Omega} \int_{line} \epsilon_{ik, y} P_{line}^{ems}(\lambda) d\lambda d\Omega = 4\pi\epsilon_{ik, y}.\quad (3.49)$$

The result of the integration, $4\pi\epsilon_{ik, y}$, is independent of the plasma geometry.

The radiation that is absorbed is determined by the spectral absorption coefficient $\alpha_y(\lambda)$ at position y and the spectral radiance of the line originating from the whole plasma volume that reaches position y , $L_y(\lambda, l(\Omega))$:

$$\text{absorbed radiation at } y = \int_{\Omega} \int_{line} \alpha_y(\lambda) L_y(\lambda, l(\Omega)) d\lambda d\Omega.\quad (3.50)$$

The spectral radiance $L_y(\lambda, l(\Omega))$ depends on the individual lengths $l(\Omega)$ in each direction which are given by the plasma geometry. This is indicated by the dependence of l on the solid angle Ω . The population escape factor is now given by

$$\Theta_{pop} = 1 - \frac{\int_{\Omega} \int_{line} \alpha_y(\lambda) L_y(\lambda, l(\Omega)) d\lambda d\Omega}{4\pi\epsilon_{ik, y}}.\quad (3.51)$$

As in this work a cylindrical plasma is investigated, the calculation is carried out for the position y being on the central axis of the cylinder assuming a point symmetry of the plasma parameters. A sketch of the geometry where the integration variables are denoted is shown in figure 3.2. For each value of Ω , the radiation transport calculation is done by integrating along the line of sight (described by the x -axis) starting at the plasma edge ($x = 0$) and ending at position y ($x = l(\Omega)$). The spectral radiance that reaches position y is defined after equation (3.40):

$$L_y(\lambda, l(\Omega)) = \int_0^{l(\Omega)} \epsilon(\lambda, x) \exp[-(l(\Omega) - x) \alpha(\lambda, x)] dx.\quad (3.52)$$

If it is assumed that the absorption is homogeneous ($\alpha_y(\lambda) = \alpha(\lambda, x) \equiv \alpha(\lambda)$),

the population escape factor for a cylindrical geometry is given by [Beh98]:

$$\Theta_{pop} = 1 - \frac{\int_{\Omega} \int_{line} \alpha(\lambda) \int_0^{l(\Omega)} \epsilon(\lambda, x) \exp[-(l(\Omega) - x) \alpha(\lambda)] dx d\lambda d\Omega}{4\pi\epsilon_{ik, y}}. \quad (3.53)$$

Due to the dependence of $\epsilon(\lambda, x)$ and $\alpha(\lambda)$ on the line profile (according to equations (3.41) and (3.42)) also the population escape factor depends on the line profile. Furthermore, Θ_{pop} depends on the radial distribution of the emission which can be assumed to be parabolic in cylindrical plasmas [BF00].

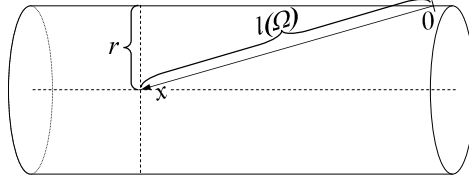


Figure 3.2: Sketch of the cylindrical geometry; r denotes the cylinder radius and the position y is located at the intersection point of the two dashed lines.

Dependence of the Population Escape Factor on the Line Profile

As stated in section 3.3.1, several effects contribute to the line profile in low pressure plasmas resulting in Lorentzian and Gaussian contributions to the line profile. If the Lorentzian contributions to the line profile could be neglected, only the gas temperature and the mass of the radiating particle is needed for the calculations of the population escape factor. No transition-specific constants would be required which would greatly reduce the effort. Therefore the influence of the Lorentzian profile on Θ_{pop} is investigated by comparing the values obtained with an Gaussian line profile ($\omega_{Gauss} = 3$ pm) and a Voigt profile whose FWHM of the Lorentzian part is assumed to be two orders of magnitude lower than the FWHM of the Gaussian part: $\omega_{Gauss} = 3$ pm, $\omega_{Lorentz} = 3 \times 10^{-2}$ pm. The values of the FWHM are only chosen exemplarily. Figure 3.3 shows the population escape factors calculated after equation (3.53) for the two line profiles exemplary for an infinite long cylinder with a radius of 1 m and a parabolic radial distribution of the emission. The integration over the solid angle of an infinite cylinder which is needed for the calculation of Θ_{pop} is shown in the appendix in section B.

At small values of α_{ik} (α_{ik} is defined after equation (3.42)) the population escape factor is unity as reabsorption effects can be neglected. Above $\alpha_{ik} = 10^{-5}$ the values of Θ_{pop} start to decrease. Up to $\alpha_{ik} \approx 10^{-2}$ the reabsorption dominantly

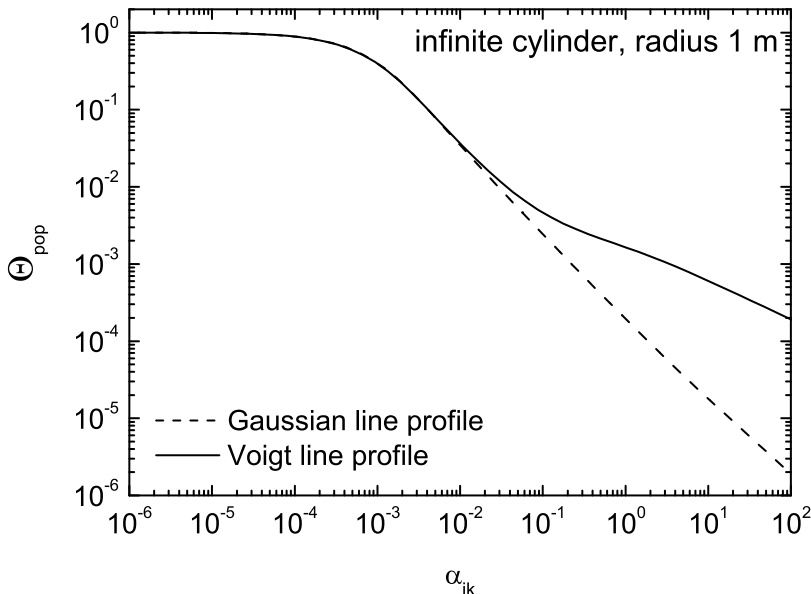


Figure 3.3: Population escape factors calculated with a Gaussian ($\omega_{Gauss} = 3 \text{ pm}$) and with a Voigt profile with $\omega_{Gauss} = 3 \text{ pm}$ and $\omega_{Lorentz} = 3 \times 10^{-2} \text{ pm}$.

occurs around the central wavelength of the transition. Thus the curves obtained with the two different profiles are the same. As stated in section 3.3.1, the line profile around λ_0 is mainly determined by the Doppler and therefore Gaussian profile which makes the influence of the Lorentzian part negligible. A further increase of α_{ik} leads to stronger reabsorption making the Lorentzian contribution which arise from natural and collisional line broadening important. However, as the Voigt profile is spread over a much broader wavelength range than a Gaussian profile, reabsorption in the wings of the line is still rather low. This results in a much smaller influence of reabsorption effects on the population compared to a pure Gaussian profile: At $\alpha_{ik} \approx 1$ the deviation of the Θ_{pop} -values obtained with the different line profiles is already one order of magnitude.

In summary, opacity effects considered by the population escape factor can be separated into three regions depending on α_{ik} : Below a threshold value Θ_{pop} is unity as reabsorption can be neglected completely, the plasma is optically thin. In the mid-range of α_{ik} reabsorption becomes important but it is sufficient to consider only Doppler broadening. At high values of α_{ik} it is important to take the Lorentzian contributions to the line profile into account even if their FWHM is orders of magnitude smaller compared to the FWHM of Doppler broadening. Therefore it is very important to check for each transition which region of α_{ik} is relevant for the investigated plasma as neglecting the Lorentzian contributions to the profile may lead to a strong overestimation of reabsorption effects.

4 Diagnostic Methods

4.1 Optical Emission Spectroscopy

In optical emission spectroscopy (OES) the line of sight integrated plasma emission is used to obtain densities of upper states of atomic or molecular transitions and the radiated power. OES is a non-invasive diagnostic method which means measurements do not influence the plasma.

For lighting purposes it is important to determine the power that is radiated by the discharge into the whole solid angle Ω [sr]. The line emission coefficient ϵ_{ik} [W/(m³ sr)] gives the radiated power of an emission line originating from a transition between an upper state i and a lower state k (see equation (3.41)). ϵ_{ik} is obtained by integrating the line-of-sight averaged spectral emission coefficient $\epsilon(\lambda)$ [W/(m³ nm sr)], which is measured by a spectrometer, over the emission line:

$$\int_{\Omega} \epsilon_{ik} d\Omega = \int_{\Omega} \int_{line} \epsilon(\lambda) d\lambda d\Omega, \quad (4.1)$$

$$\text{with } \epsilon(\lambda) = \frac{1}{l} \int_0^l \epsilon(\lambda, x) dx, \quad (0 \leq x \leq l),$$

where l denotes the length of the line of sight. Usually, the dependence of the isotropic spectral emission coefficient on the solid angle is already considered in the calibration of the spectrometer, so that the spectral emission coefficient integrated over the whole solid angle, $\epsilon_{cal}(\lambda)$ [W/(m³ nm)], is already obtained by the measurement (for details on the calibration of a spectrometer see section 5.2). Furthermore the spectrometer is typically calibrated in a way that the solid-angle-integrated number of photons radiated by an emission line $\epsilon_{photons}(\lambda)$ [1/(m³ nm s)] is obtained by the measurement. Therefore the line emission coefficient has to be calculated taking into account the energy of the photons:

$$\int_{\Omega} \epsilon_{ik} d\Omega = \int_{line} \epsilon_{cal}(\lambda) d\lambda = \int_{line} \epsilon_{photons}(\lambda) \frac{hc}{\lambda} d\lambda. \quad (4.2)$$

The power Φ_{ik} [W] of a transition emitted by the whole plasma is given by multiplying the solid-angle-integrated line emission coefficient with the actual plasma volume V_{plasma} [m³] assuming a homogeneous emission:

$$\Phi_{ik} = V_{plasma} \int_{\Omega} \epsilon_{ik} d\Omega. \quad (4.3)$$

The efficiency of the plasma η_{ik} describes the fraction of the RF-power P [W] coupled into the plasma which is transferred into light output of the transition $i \rightarrow k$:

$$\eta_{ik} = \frac{\Phi_{ik}}{P}. \quad (4.4)$$

To obtain population densities from optical emission spectroscopy measurements, the emissivity I_{ik} [1/(m³ s)] of a transition has to be calculated. I_{ik} is given by integrating $\epsilon_{photons}(\lambda)$ over the emission line:

$$I_{ik} = \int_{line} \epsilon_{photons}(\lambda) d\lambda. \quad (4.5)$$

The population density of the upper state n_i [m⁻³] can now be obtained with the transition probability for spontaneous emission A_{ik} [s⁻¹] after

$$n_i = \frac{I_{ik}}{A_{ik}}. \quad (4.6)$$

Spectroscopic measurements can typically be reproduced within $\pm 5\%$. As this is also true for the intensity calibration the total error of quantities determined from OES measurements can be estimated to be $\pm 10\%$.

4.1.1 Optical Emission Spectroscopy of Molecules

In this section, OES of molecular spectra arising from vibronic transitions ($i, v' \rightarrow k, v''$) are considered disregarding the rotational structure. The emissivity $I_{ik}^{v'v''}$ of this transition is given by integrating the radiated number of photons $\epsilon_{photons}(\lambda)$ over the rotational structure. The population density $n_i^{v'}$ of a vibrational state in the upper electronic state can then be calculated after equation (4.6):

$$n_i^{v'} = \frac{I_{ik}^{v'v''}}{A_{ik}^{v'v''}}. \quad (4.7)$$

With InBr or InCl the single vibronic transitions cannot be resolved as the emission bands overlap strongly due to Doppler broadening, i. e. the respective emissivity $I_{ik}^{v'v''}$ cannot be determined. However, if the relative vibrational population $n_{i,rel}^{v'}$ is known, the population density of the whole electronic state i can be derived using effective transition probabilities A_{ik}^{eff} . In doing so, the vibrationally resolved transition probabilities $A_{ik}^{v'v''}$ have to be weighted according to the relative vibrational population $n_i^{v'}$ which is normalized to $\sum_{v'} n_{i,rel}^{v'} = 1$ [FW06]:

$$A_{ik}^{eff} = \sum_{v'} n_{i,rel}^{v'} A_{ik}^{v'v''} \quad (4.8)$$

If a Boltzmann distribution of the vibrational states is valid the relative population is given by the vibrational temperature $n_{i,rel}^{v'}(T_{vib})$ (see section 3.2.3). The vibrational temperature can be determined experimentally (see section 4.5). Using the effective transition probability the population density n_i of the whole electronic state i can be calculated by summarizing over all emissivities corresponding to the transition $i \rightarrow k$:

$$n_i = \frac{\sum_{v'} \left(\sum_{v''} I_{ik}^{v'v''} \right)}{A_{ik}^{eff}}. \quad (4.9)$$

4.1.2 Correction of Reabsorption Effects

If the density of the lower state of an atomic or molecular transition is considerably high, a fraction of the emitted radiation can be reabsorbed before the photons leave the plasma. This effect called “opacity” and its influence on the population densities of the states corresponding to the transition is described in section 3.3. If a transition gets optically thick the radiance L_{ik} of an emission line that escapes from the plasma (defined after equation (3.40)) is appreciably lowered which leads to an underestimation of population densities obtained via OES. However, these densities are needed as input parameters for further analysis (e. g. see section 4.3). Therefore, the reabsorption of emitted radiation along the line of sight with length l ($0 \leq x \leq l$) has to be considered according to equation (3.43):

$$L_{ik}(l) = \int_{line} \int_0^l \epsilon_{ik}(x) P_{line}^{ems}(\lambda) \exp[-(x-l) \alpha_{ik} P_{line}^{abs}(\lambda)] dx d\lambda. \quad (4.10)$$

All quantities of the equation are defined as described in section 3.3. As the OES measurements are performed along the central axis of a cylindrical plasma (see

section 5.2), the emission can be considered as constant along the line of sight ($\epsilon_{ik}(x) \hat{=} \epsilon_{ik}$) as it is radially symmetric. Furthermore it is assumed that the emission and absorption line profiles are the same: $P_{line}^{ems}(\lambda) \hat{=} P_{line}^{abs}(\lambda) = P_{line}(\lambda)$. This is reasonable as the parameters that determine the line profile according to section 3.3 are the same for the particles being in the absorbing or being in the emitting state in the investigated plasmas. The integration over the line of sight yields

$$L_{ik}(l) = \int_{line} \frac{\epsilon_{ik}}{\alpha_{ik}} [1 - \exp(-\alpha_{ik} l P_{line}(\lambda))] d\lambda. \quad (4.11)$$

Similarly to the population escape factor Θ_{pop} of section 3.3 which accounts for reabsorption effects in the plasma volume (needed for collisional radiative models), a line escape factor Θ_{line} can be defined. The line escape factor takes reabsorption effects along the line of sight into account and can therefore be used to correct the underestimation of the density obtained via OES. Θ_{line} is given by the ratio of the escaping radiance of the emission line considering (optically thick) and neglecting reabsorption (optically thin) [Beh98]:

$$\Theta_{line} = \frac{L_{ik}(l)^{\text{optically thick}}}{L_{ik}(l)^{\text{optically thin}}} = \frac{\int_{line} \frac{\epsilon_{ik}}{\alpha_{ik}} [1 - \exp(-\alpha_{ik} l P_{line}(\lambda))] d\lambda}{\int_{line} \int_0^l \epsilon_{ik} P_{line}^{ems}(\lambda) dx d\lambda}. \quad (4.12)$$

As the integration of the optically thin radiation simply yields $\epsilon_{ik} l$ the line escape factor is given by

$$\Theta_{line} = \frac{1}{\alpha_{ik} l} \int_{line} [1 - \exp(-\alpha_{ik} l P_{line}(\lambda))] d\lambda, \quad (4.13)$$

which is independent of the line emission coefficient. The expression in the exponential function, $\alpha_{ik} l P_{line}(\lambda)$, is also referred to as the optical depth $\tau(\lambda)$ of a transition (see section 4.2). The opacity-corrected population densities can now be derived from OES measurements by modifying equation (4.6):

$$n_i = \frac{I_{ik}}{A_{ik} \Theta_{line}}. \quad (4.14)$$

Dependence of the Line Escape Factor on the Line Profile

After equation (4.13) the line escape factor is dependent on the line profile $P_{line}(\lambda)$ and the value of $\alpha_{ik} l$. It should be noted that the value of $\alpha_{ik} l$ has to be given in [nm] for the calculation as the wavelength is also used in [nm]. As shown in section 3.3 the line profile in low pressure plasmas consists of Gaussian and Lorentzian

contributions where the FWHM of the Lorentzian parts is usually several orders of magnitude smaller than the Gaussian FWHM. As stated in section 3.3.2 no transition-specific constants would be required if the Lorentzian contributions could be neglected. This would greatly reduce the effort for the calculation of the line escape factor. Therefore the influence of the Lorentzian part of the line profile has to be investigated first. Figure 4.1 shows an exemplary Θ_{line} calculated by using a pure Gaussian line profile ($\omega_{Gauss} = 3$ pm) and a Voigt profile. The Lorentzian part in the Voigt profile is assumed to be two orders of magnitude smaller than the FWHM of the Gaussian part: $\omega_{Gauss} = 3$ pm, $\omega_{Lorentz} = 3 \times 10^{-2}$ pm. The Gaussian and the Voigt line profile are normalized to $\int_{profile} P_{line}(\lambda) d\lambda = 1$.

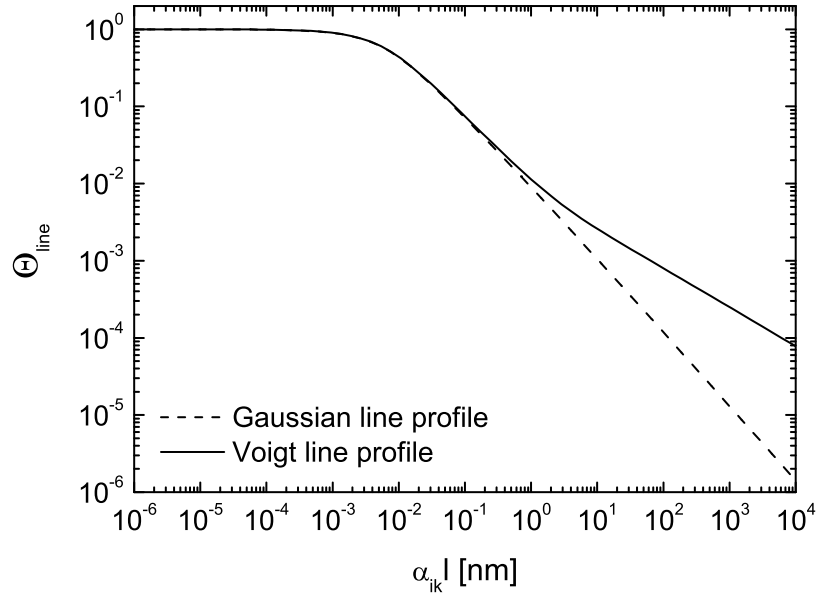


Figure 4.1: Line escape factors calculated with a Gaussian ($\omega_{Gauss} = 3$ pm) and with a Voigt profile with $\omega_{Gauss} = 3$ pm and $\omega_{Lorentz} = 3 \times 10^{-2}$ pm.

Similar to the opacity effects described by population escape factors (which are discussed in section 3.3.2) the reabsorption effects described by the line escape factor can be separated into three parts: The first region at small values of $\alpha_{ik} l$, where Θ_{line} is unity as reabsorption can be neglected, the second region (10^{-3} nm $\lesssim \alpha_{ik} l \lesssim 10^{-1}$ nm) where reabsorption becomes important but it is sufficient to consider the Gaussian Doppler profile and the third region where also the Lorentzian contributions which arise from natural and collisional line broadening are relevant. Hence one must figure out which region of $\alpha_{ik} l$ is relevant for the investigated transition.

4.2 White Light Absorption Spectroscopy¹

White light absorption spectroscopy is used to determine the line of sight integrated density of an absorbing atomic or molecular species in the plasma. If light passes through a homogeneously absorbing medium of length l , e. g. a plasma, the transmitted intensity is given by

$$I(\lambda, l) = I(\lambda, 0) \exp[-\tau(\lambda)], \quad (4.15)$$

where $I(\lambda, x)$ is the intensity at wavelength λ and position x with $0 \leq x \leq l$ [Tho88]. The optical depth $\tau(\lambda)$ of a line is defined as [Tho88]:

$$\tau(\lambda) = \frac{\lambda_0^4}{8\pi c} \frac{g_i}{g_k} A_{ik} n_k l P_{line}(\lambda) = \alpha_{ik} l P_{line}(\lambda), \quad (4.16)$$

where the last part of the equation follows from equation (3.42). All quantities of the above equation are defined as described in section 3.3. As the line profile is normalized to $\int_{line} P_{line}(\lambda) d\lambda = 1$, the value of $\alpha_{ik} l$ is equal to the magnitude of the optical depth for a given line profile. It should again be noted that the unit of $\alpha_{ik} l$ has to be in [nm] as the wavelength is also given in [nm].

By integrating the logarithm of the intensity over the wavelength of the absorption line, n_k can be determined according to equations (4.15) and (4.16):

$$n_k = \frac{8\pi c}{\lambda_0^4} \frac{g_k}{g_i} \frac{1}{A_{ik} l} \int_{line} \ln \left(\frac{I(\lambda, 0)}{I(\lambda, l)} \right) d\lambda. \quad (4.17)$$

Hereafter the integrand is called the absorption signal. This makes it easier to distinguish it from the transmitted intensity.

For white light absorption measurements no intensity calibration of the spectroscopic setup is required. However, to obtain the absorption signal the plasma emission has to be subtracted from the measured transmitted intensity. Spectroscopic measurements can typically be reproduced within $\pm 5\%$ which results in an over-all error of $\pm 10\%$ of white light absorption measurements.

Similar to optical emission spectroscopy of molecules the effective transition probability A_{ik}^{eff} can be utilized for absorption measurements. In this case, the absorption signal has to be integrated over the whole system of the electronic

¹The explanations and remarks of this section especially on the apparent optical depth have also been submitted for publication [BWF11].

transition $k \rightarrow i$:

$$n_k = \frac{8\pi c g_k}{\lambda_0^4 g_i A_{ik}^{eff} l_{system}} \int \ln \left(\frac{I(\lambda, 0)}{I(\lambda, l)} \right) d\lambda. \quad (4.18)$$

Saturation in White Light Absorption Spectroscopy

If the optical depth is substantial a saturation effect of the transmitted intensity occurs [Tho88]. This effect arises in the following way: The optical depth of a line is strongest at the central wavelength λ_0 . While passing through the absorbing medium the intensity at the central wavelength $I(\lambda_0, x)$ decreases much faster than the intensity at the wings of the line $I(\lambda_0 \pm \delta\lambda, x)$. At position $x + \delta x$, the incident radiation at λ_0 is therefore smaller than at $\lambda_0 \pm \delta\lambda$. As the absorption is proportional to the incident intensity according to equation (4.15), the absorption at $x + \delta x$ is smaller at the central wavelength compared to the wings of the line. This leads to the saturation of the transmitted intensity with increasing $\alpha_{ik} l$ especially around λ_0 which is shown in figure 4.2 (a). In this figure the transmitted intensities which are normalized to the incident intensity calculated for an exemplary Gaussian line profile with a FWHM of $\omega_{line} = 3$ pm and different values of $\alpha_{ik} l$ are plotted. Furthermore it can be seen that the absorption line seems to be broadened due to the saturation of the peak intensity. For very high optical depths the transmitted intensity approaches zero around λ_0 .

4.2.1 True and Apparent Optical Depth

A white light absorption signal is usually recorded with a spectrometer having a finite wavelength resolution which is typically defined by a Gaussian apparatus profile $P_{app}(\lambda)$ [nm^{-1}] normalized to $\int_{profile} P_{app}(\lambda) d\lambda = 1$. The intensity $I_{meas}(\lambda, l)$ measured with the spectrometer is given by the convolution of the transmitted intensity $I(\lambda, l)$ with the apparatus profile [SS91]:

$$I_{meas}(\lambda, l) = \{I(\lambda, 0) \exp[-\tau(\lambda)]\} * P_{app}(\lambda). \quad (4.19)$$

The incident intensity of the white light changes only slightly over the wavelength range of an absorption line and can be considered as constant: $I(\lambda, 0) = I_0$. Therefore the transmitted intensity is given by

$$I_{meas}(\lambda, l) = I_0 \{\exp[-\tau(\lambda)]\} * P_{app}(\lambda). \quad (4.20)$$

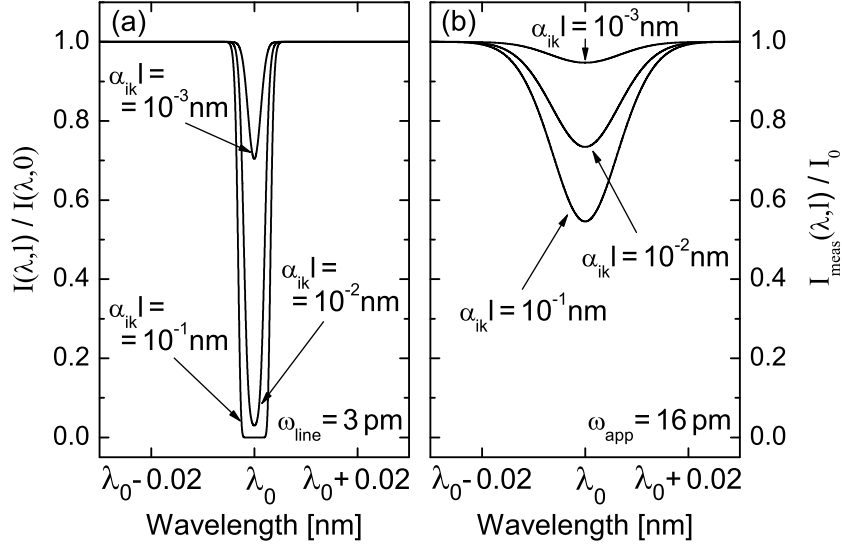


Figure 4.2: Calculated white light absorption spectra for different values of $\alpha_{ik} l$ for a Gaussian line profile (FWHM 3 pm). Part a: normalized transmitted intensity $I(\lambda, l)/I(\lambda, 0)$. Part b: normalized intensity $I_{meas}(\lambda, l)/I_0$ using a Gaussian apparatus profile with $\omega_{app} = 16$ pm.

Figure 4.2 (b) shows measured transmitted intensities which are calculated after equation (4.20) with the transmitted intensities shown in figure 4.2 (a) and an exemplary Gaussian apparatus profile with FWHM $\omega_{app} = 16$ pm. It can be seen that the convolution of the transmitted intensity with $P_{app}(\lambda)$ leads to a broadening of the line and a strong reduction of the peak height compared to the profiles of figure 4.2 (a) as $\omega_{app} > \omega_{line}$. Moreover the saturation of the peak intensity is greatly reduced compared to the real transmitted intensity and the flattening of the absorption line as the intensity approaches zero at high optical depths can no longer be seen. However, the integral of the absorption line is not affected by the convolution due to the normalization of the apparatus profile.

To determine the influence of the broadening caused by the apparatus profile on the density the integration over the logarithm of the inverted normalized intensity has to be carried out according to equation (4.17). Since the absolute values of $I_{meas}(\lambda, l)/I_0$ differ from those of $I(\lambda, l)/I(\lambda, 0)$, the measured absorption signal $\ln[I_0/I_{meas}(\lambda, l)]$ also differs from the real one $\ln[I(\lambda, 0)/I(\lambda, l)]$. In the present case of white light absorption, the broadening results in a lower measured absorption signal compared to the real one:

$$\int_{line} \ln \left(\frac{I(\lambda, 0)}{I(\lambda, l)} \right) d\lambda \geq \int_{line} \ln \left(\frac{I_0}{I_{meas}(\lambda, l)} \right) d\lambda. \quad (4.21)$$

This results in an underestimation of the density determined by the absorption measurements. The integrals of equation (4.21) only coincide if $\omega_{app} \ll \omega_{line}$ as in this case the real absorption signal is approximately reproduced despite the convolution with $P_{app}(\lambda)$ [SS91].

In order to distinguish the real absorption signal (or the real optical depth) from the measured one, the measured signal is referred to as the apparent absorption signal (or the apparent optical depth).

4.2.2 Correction of the Apparent Optical Depth

In low pressure plasmas the FWHM of the absorption line is typically much smaller than ω_{app} . If the optical depth is substantial the effect of the apparent optical depth has to be taken into account. This can be done in the data evaluation by introducing a correction factor for white light absorption spectroscopy measurements f_{WLABS} defined by the ratio of the integral over the real absorption signal and the integral over the measured apparent absorption signal:

$$f_{WLABS} = \frac{\int_{line} \ln \left(\frac{I(\lambda,0)}{I(\lambda,l)} \right) d\lambda}{\int_{line} \ln \left(\frac{I_0}{I_{meas}(\lambda,l)} \right) d\lambda} = \frac{\alpha_{ik} l}{A_{meas}} \geq 1. \quad (4.22)$$

A_{meas} [nm] is the integral of the measured absorption signal. The density of the lower state n_k is then given by

$$n_k = f_{WLABS} \frac{8\pi c g_k}{\lambda_0^4 g_i} \frac{1}{A_{ik} l} \int_{line} \ln \left(\frac{I_0}{I_{meas}(\lambda,l)} \right) d\lambda. \quad (4.23)$$

For low optical depth the correction factor approximates unity. This is also the case if $\omega_{app} \ll \omega_{line}$ holds.

The value of the correction factor is dependent on $\alpha_{ik} l$ and therefore on n_k which is not known prior to the absorption measurement. However, for a given line profile and apparatus profile the real and the measured absorption signal can be calculated for any values of $\alpha_{ik} l$ using equations (4.15) , (4.16) & (4.20). This yields the area of the calculated measured apparent absorption signal $A_{meas}^{calc}(\alpha_{ik} l, P_{line}, P_{app})$ and the corresponding correction factor for any value of $\alpha_{ik} l$. Therefore just the area A_{meas}^{calc} can be used to determine f_{WLABS} :

$$A_{meas}^{calc}(\alpha_{ik} l, P_{line}, P_{app}) = A_{meas} \quad \Rightarrow \quad f_{WLABS}. \quad (4.24)$$

For a given line profile and apparatus profile each $\alpha_{ik} l$ determines A_{meas}^{calc} and f_{WLABS} unambiguously. Obviously, a good knowledge of both profiles is essential for this approach.

Despite the use of A_{meas}^{calc} for the determination of the correction factor for the measurements the considerations in the following section are made with respect to $\alpha_{ik} l$ and not to A_{meas}^{calc} as the optical depth is the relevant physical quantity.

Dependence of the Correction Factor on P_{line} and P_{app}

In order to investigate the influence of the Lorentzian contribution of the line profile due to natural and collisional line broadening (see section 3.3.1) on the correction of the apparent optical depth, calculations are carried out by using a Gaussian Doppler line profile ($\omega_{Gauss} = 3$ pm) and a Voigt profile both plotted in figure 4.3. In both cases a Gaussian apparatus profile with $\omega_{app} = 16$ pm is used for the calculations. The FWHM of the Lorentzian part in the Voigt profile is assumed to be two orders of magnitude lower than the FWHM of the Gaussian part: $\omega_{Gauss} = 3$ pm, $\omega_{Lorentz} = 3 \times 10^{-2}$ pm.

Similarly to the consideration of opacity by line or population escape factors (see section 4.1.2 and 3.3.2) three regions can be defined for f_{WLABS} : Below a threshold value of $\alpha_{ik} l$ the correction factor is almost unity and the difference between the apparent and the true optical depth can be neglected. In the mid-range of the optical depth (above $\alpha_{ik} l \approx 10^{-4}$ nm) the correction cannot be neglected, but it is sufficient to consider only the Doppler profile. Above $\alpha_{ik} l \approx 0.1$ nm the Lorentzian contributions to the line profile arising from natural and collisional line broadening have to be taken into account in the calculation of f_{WLABS} even if their FWHM is orders of magnitude smaller compared to $\omega_{Doppler}$.

The second profile besides the line profile that determines the correction factor is the apparatus profile. If $\omega_{app} \ll \omega_{line}$ no correction factor has to be applied. On the contrary, the larger ω_{app} gets with respect to ω_{line} the larger gets f_{WLABS} . This can be seen in figure 4.4 where the correction factor is calculated for different values of the FWHM of a Gaussian apparatus profile. For the calculation the same Voigt profile as in figure 4.3 is used. Below an optical depth of $\alpha_{ik} l = 3 \times 10^{-3}$ nm the difference between the correction factors calculated with $\omega_{app} = 6$ pm and with $\omega_{app} = 26$ pm is smaller than 10%. The deviation rises up to 50 to 60% at high optical depths. Therefore the calculation of f_{WLABS} requires the FWHM of the apparatus profile for each transition.

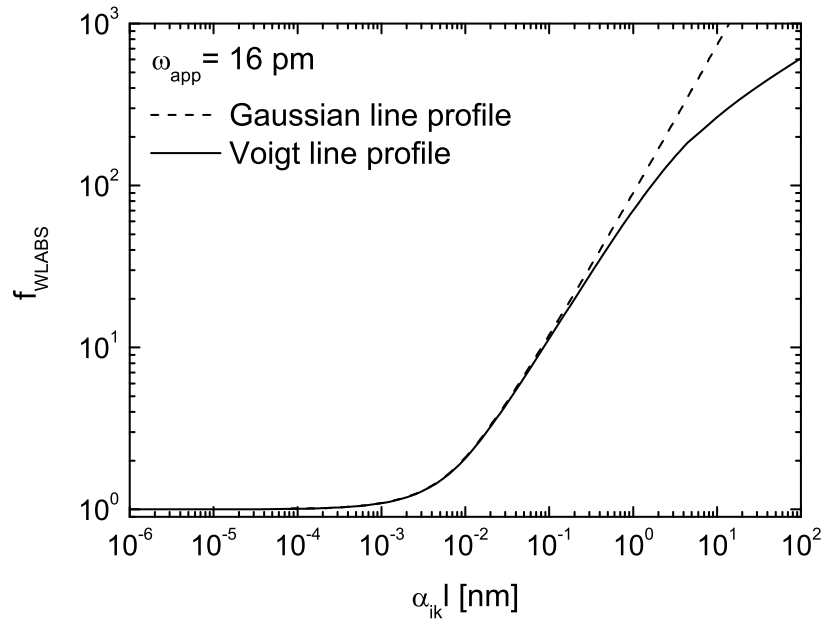


Figure 4.3: Correction factors for saturation in white light absorption spectroscopy calculated with a Gaussian ($\omega_{\text{Gauss}} = 3 \text{ pm}$) and with a Voigt profile with $\omega_{\text{Gauss}} = 3 \text{ pm}$ and $\omega_{\text{Lorentz}} = 3 \times 10^{-2} \text{ pm}$. The apparatus profile is assumed to be Gaussian with $\omega_{\text{app}} = 16 \text{ pm}$.

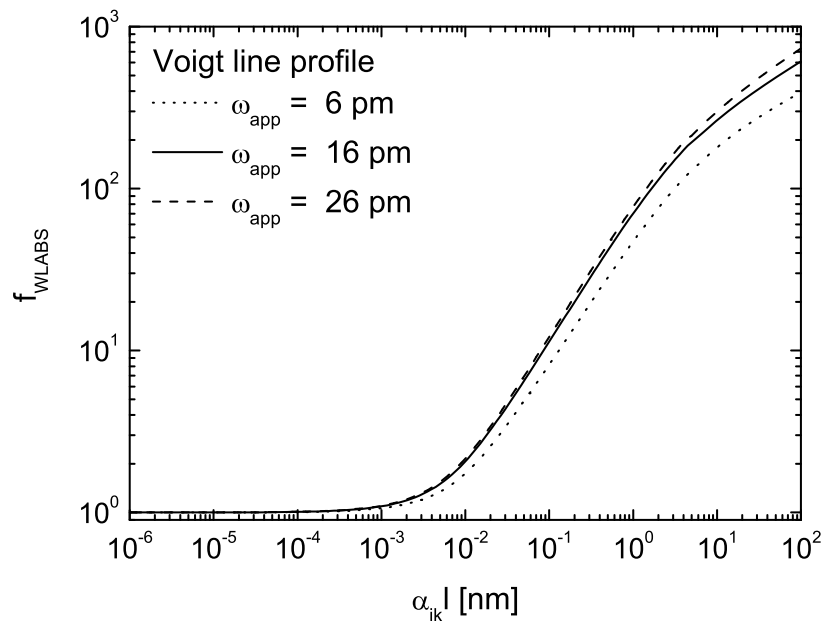


Figure 4.4: Correction factors for saturation in white light absorption spectroscopy calculated with a Voigt line profile ($\omega_{\text{Gauss}} = 3 \text{ pm}$, $\omega_{\text{Lorentz}} = 3 \times 10^{-2} \text{ pm}$) and a varying FWHM of the Gaussian apparatus profile.

4.3 Extended Corona Model of Indium

In an indium halide containing rare gas discharge the background gas radiation vanishes with increasing cold spot temperature which limits the range where the corresponding population models can be applied. Thus a population model of the relevant indium states is set up to determine the electron temperature and density. Adjusting the modelled population densities to those measured with emission and absorption spectroscopy by varying the model input parameters n_e and T_e yields their values provided that all other required input parameters are known. It should be noted that the measured population densities are averaged over the axial line of sight, i. e. also the values of n_e and T_e are line-of-sight-averaged. However, in cylindrical discharges the axial profiles of n_e and T_e can be assumed to be constant in contrast to their radial profiles.

As stated in section 3.2.5 the population processes of a typical low pressure low temperature plasma used for lighting purposes have to be modelled with a collisional-radiative model. However, setting up this model requires a detailed knowledge of many cross sections and transition probabilities. For indium this data is mostly not available in the literature. Thus a corona model which requires less (and available) data is applied to the relevant states of the indium atom.

The indium corona model includes the population and depopulation processes of the $6\ ^2S_{1/2}$ and the $7\ ^2S_{1/2}$ states which have an excitation energy of 3.02 and 4.50 eV respectively [GGV90] (figure 4.5 shows a part of the energy level diagram of the indium atom). The ground state of indium (which has the electron configuration [Kr] $4d^{10} 5s^2 5p^1$) is split into the $5\ ^2P_{1/2}$ state and the metastable $5\ ^2P_{3/2}$ state which has an excitation energy of 0.27 eV [GGV90]. Hence the corona model has to be extended to consider electron impact excitation out of the metastable $5\ ^2P_{3/2}$ state as well as this process contributes significantly to the population density of the excited states. In the extended corona model of the state i ($6\ ^2S_{1/2}$ or $7\ ^2S_{1/2}$) electron impact excitation out of both fine structure components of the ground state is balanced with spontaneous emission:

$$\begin{aligned}
 n_{5\ ^2P_{1/2}} n_e X_{5\ ^2P_{1/2} \rightarrow i}^{e^- \text{ impact exc.}}(T_e) + n_{5\ ^2P_{3/2}} n_e X_{5\ ^2P_{3/2} \rightarrow i}^{e^- \text{ impact exc.}}(T_e) = \\
 = n_i \sum_{k < i} A_{ik} = \frac{n_i}{\tau_i}. \quad (4.25)
 \end{aligned}$$

n is the density of the state which is denoted in the subscript, $X^{e^- \text{ impact exc.}}(T_e)$ is the rate coefficient for electron impact excitation out of the $5\ ^2P_{1/2}$ or the $5\ ^2P_{3/2}$

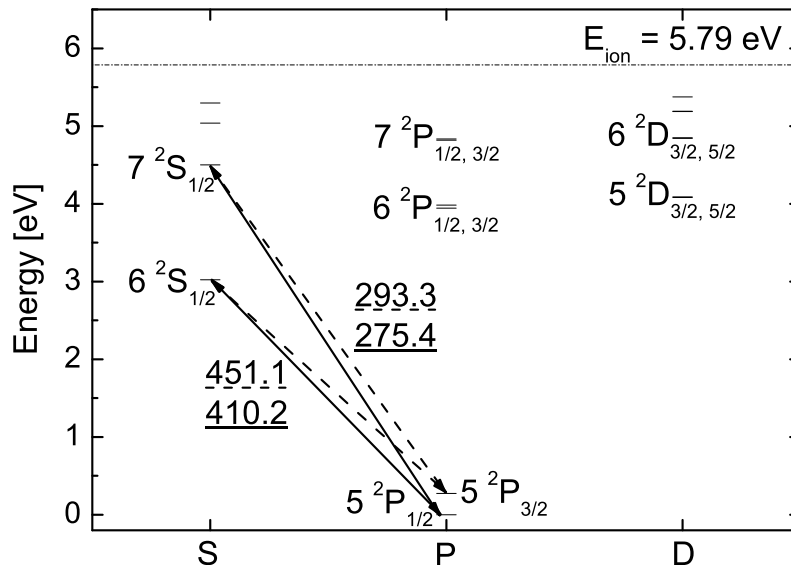


Figure 4.5: Part of the energy level diagram of indium based on the data from [GGV90]. The transitions which are relevant for the extended corona model are plotted together with their central emission wavelength.

state into the state i and A_{ik} is the transition probability from the state i to the lower state k ($5^2P_{1/2}$ or $5^2P_{3/2}$). The radiance lifetime τ_i which equals the inverse sum $\sum_{k<i} A_{ik}$ is 7.2 ns for the $6^2S_{1/2}$ state [LDF78] and 19.5 ns for the $7^2S_{1/2}$ state [ES83]. The rate coefficients $X^{e^- \text{ impact exc.}}(T_e)$ are calculated after equation (3.22) which requires cross sections (taken from [SN74]) and the electron energy distribution function. As stated in section 3.2.5 a pressure in the range of mbar can lead to deviations of the EEDF from a Maxwellian distribution. However, if on the other hand the electron density is high (which is the case for indium halide/rare gas discharges) this results in a high frequency of elastic electron – electron collisions. This leads to a better thermalization of the electrons among each other and therefore to a decrease of the deviation of the EEDF from a Maxwellian distribution. A measurement of the EEDF which is typically done using Langmuir-probes cannot be carried out in indium halide containing discharges as the tungsten wire of the probe is quickly eroded by the halide. Therefore a Maxwellian EEDF is assumed due to the high electron densities of indium halide/rare gas discharges for the calculation of the rate coefficients.

Determination of the Electron Temperature

If the ratio of equation (4.25) applied to the densities of the $6^2S_{1/2}$ and the $7^2S_{1/2}$ state is taken, the resulting equation is independent of n_e since it cancels out,

but the equation is still dependent of the electron temperature:

$$\frac{n_{6^2S_{1/2}}}{n_{7^2S_{1/2}}} = \frac{\tau_{6^2S_{1/2}}}{\tau_{7^2S_{1/2}}} \times \frac{n_{5^2P_{1/2}} X_{5^2P_{1/2} \rightarrow 6^2S_{1/2}}^{e^- \text{ impact exc.}}(T_e) + n_{5^2P_{3/2}} X_{5^2P_{3/2} \rightarrow 6^2S_{1/2}}^{e^- \text{ impact exc.}}(T_e)}{n_{5^2P_{1/2}} X_{5^2P_{1/2} \rightarrow 7^2S_{1/2}}^{e^- \text{ impact exc.}}(T_e) + n_{5^2P_{3/2}} X_{5^2P_{3/2} \rightarrow 7^2S_{1/2}}^{e^- \text{ impact exc.}}(T_e)}. \quad (4.26)$$

With knowledge of the four population densities the electron temperature can be determined. To obtain the required densities from spectroscopic measurements the corresponding transition probabilities are needed. However, there exist several references for the A_{ik} -values of the relevant transitions [PS62, CB62, FMM78, WM80, Doi95, Mor00]. In some cases the given values differ by a factor of 10. Since reference [Mor00] represents a recent review of the existing experimental and theoretical data, the values recommended by this reference are used in this work. Table 4.1 shows the relevant transition probabilities.

Table 4.1: *Transition probabilities for the relevant indium lines [Mor00].*

Wavelength [nm]	A_{ik} [10^8 s^{-1}]
275.4	0.13
293.3	0.23
410.2	0.50
451.1	0.89

White light absorption measurements of the lines at 410.2 and 451.1 nm are used to obtain the densities of the $5^2P_{1/2}$ and $5^2P_{3/2}$ states as these transitions provide a better detection limit than the lines at 275.4 and 293.3 nm. The better detection limit arises from the better detector sensitivity and the higher intensity of the white light source between 400 and 460 nm compared to the sensitivity and the intensity between 275 and 300 nm. The densities of the $6^2S_{1/2}$ and $7^2S_{1/2}$ states are determined via OES. The measurement of the 410.2 and the 451.1 nm line each yield the density of the $6^2S_{1/2}$ state. The obtained density values should coincide but they differ up to a factor of 2. This difference can arise from inaccurate values of the corresponding transition probabilities. The same differences are obtained for the population density of the $7^2S_{1/2}$ state which is determined by measurements of the 275.4 and the 293.3 nm line. To improve the reliability of the model, the averaged value of the two obtained densities is used for the model for the population density of both the $6^2S_{1/2}$ and the $7^2S_{1/2}$ state.

Determination of the Electron Density

If the electron temperature is known, equation (4.25) can be used to determine n_e from the absolute density value of the $6\ ^2S_{1/2}$ or of the $7\ ^2S_{1/2}$ state. It turned out that the two values of n_e obtained from the different states usually coincide within 10%. These two values are averaged to obtain the final electron temperature.

Input Data for Opacity and Apparent Optical Depth Correction

The amount of atomic indium in the discharge is correlated with the indium halide density as indium is generated by the dissociation of the molecule. If the plasma contains high indium halide amounts the density of indium gets high enough that reabsorption of the emission of indium lines and saturation in absorption measurements occurs. Therefore these effects have to be considered in the determination of the population densities according to sections 4.1.2 and 4.2.2.

For the calculation of the line escape factor Θ_{line} and the correction factor for saturation in white light absorption f_{WLABS} the line profile of the relevant transition is required according to equations (4.12) and (4.24). Furthermore, for the calculation of the line escape factor, the value of $\alpha_{ik} l$ is needed. According to equation (3.42) this value is given by the statistical weights of the states participating in the transition and the central wavelength (each taken from [Nat11]), the transition probability A_{ik} (taken from [Mor00]), the plasma length which is determined by the experimental setup (see section 5.2) and the density of the lower state of the transition which is known from the corrected absorption measurements. As the indium density can reach very high values also high values of $\alpha_{ik} l$ in the order of unity are reached. This makes the consideration of the Lorentzian contributions to the line profile due to natural and collisional broadening necessary both for f_{WLABS} and Θ_{line} . A computer program has been written that calculates the correction factors or the line escape factors with the profiles of the indium lines at 410.2, 451.1, 275.4 and 293.3 nm.

For each transition hyperfine splitting of the corresponding electronic states has to be considered as both isotopes of indium have a nuclear spin of 9/2. As the natural abundance of ^{115}In is 95.7% the second stable isotope, ^{113}In can be neglected in the calculations. The energy differences of the particular hyperfine split $5\ ^2P_{1/2}$, $5\ ^2P_{3/2}$ and $6\ ^2S_{1/2}$ states can be found in [DMZ53] whereas those of the $7\ ^2S_{1/2}$ state are calculated from the constants given in [GGV90]. The transitions between the hyperfine split states have different relative intensities

which can be calculated with respect to the quantum numbers. For the relevant transition this has already been carried out [DMZ53]. For the 410.2 and the 275.4 nm lines, the central wavelength of the single components differ from each other by several pm. In the low pressure range these hyperfine components do not overlap if natural, pressure and Doppler broadening is considered [EHKU84] which makes it possible to calculate the line profile of each line individually. For the 451.1 and 293.3 nm lines this is not the case. Due to the overlap of the line profile of the single components pressure broadening effects are very difficult to calculate as the individual hyperfine states influence each other [Tho88]. However, as an approximation also the line profile of the hyperfine components of the 451.1 and 293.3 nm lines is calculated individually. A summary of the energy levels of the hyperfine split states and the wavelengths of the resulting transitions can be found in the appendix in section C.

The radiance lifetime of the single states which is needed to calculate the FWHM of the natural line broadening are listed in table 4.2 together with the corresponding reference. The lifetime of the ground state is infinite and does therefore not contribute to the natural linewidth. The one of the metastable $5^2P_{3/2}$ state is not available in the literature but the radiance lifetimes of metastable states are typically in the range of 10^{-3} s or larger. Hence also the contribution of the lifetime of the metastable $5^2P_{3/2}$ state can be neglected for natural line broadening. The FWHM of the Doppler profile is determined by the atomic mass of indium which is 114.8 amu and the gas temperature which is given by the heating temperature of the discharge vessel (see section 5).

Table 4.2: *Radiance lifetimes of the relevant indium states.*

State	Lifetime τ_i [ns]	Reference
$5^2P_{1/2}$	∞	—
$5^2P_{3/2}$? (typically $\sim 10^6$)	—
$6^2S_{1/2}$	7.2	[LDF78]
$7^2S_{1/2}$	19.5	[ES83]

The spectroscopic measurements are carried out using a background gas which density exceeds the indium density by at least 3 orders of magnitude. Also the InBr density is at least one order of magnitude smaller than the density of the background gas. Therefore pressure broadening of the indium lines is rather caused by collisions of indium atoms with the atoms of the background gas than by collisions with other indium atoms or InBr molecules. The pressure broadening

data of collisions between Ar and In is only available in the literature for the $6\ ^2S_{1/2} \leftrightarrow 5\ ^2P_{1/2}$ transition [EHKU84] but not for the other lines. Because of this lack of data pressure broadening of all lines is calculated using the broadening coefficients of the 410.2 nm line shown in table 4.3 as an approximation. If a pure van-der-Waals interaction of the radiating species and the perturber is assumed (which is described by the Lindholm-Foley theory [Fol46]), the broadening coefficients show a gas temperature dependence: $\gamma/N \propto (T_{gas})^{0.3}$. This dependence can be neglected in the line profile calculations as the measurements of γ/N in [EHKU84] are carried out at $T_{gas} \approx 750$ K which corresponds to the typical gas temperatures of the discharges investigated in this work. The background-gas density which is needed for the calculation of the FWHM of pressure broadening according to equation (3.46) is derived from the filling pressure of the vessel and the gas temperature (see section 5) after the ideal gas law.

Table 4.3: *Broadening coefficients of the indium line at 410.2 nm for indium rare-gas collisions (only the investigated background gases are listed) [EHKU84].*

Background gas	Broadening coefficient [10^{-20} cm $^{-1}$ cm 3]
Neon	1.65
Argon	3.61
Krypton	3.29

If the electron density is below 10^{19} m $^{-3}$ Stark broadening can be neglected as the FWHM is at least one order of magnitude lower than the FWHM caused by pressure broadening [NF87]. However, for the investigated indium halide/rare gas discharges n_e -values above this threshold value are obtained in some cases. As the FWHM of Stark broadening depends on n_e and T_e which are not known prior to the evaluation of the extended corona model, the consideration of this effect in the line profile calculations would require an iterative determination of n_e & T_e and of the corrected densities. The values obtained by this iterative method do not necessarily converge, therefore the influence of Stark broadening on the line profile is also neglected for n_e -values above 10^{19} m $^{-3}$.

The typical error of the spectroscopic measurement of the indium population densities can be estimated to be $\pm 10\%$ but the error arising from the calculation of f_{WLBS} and Θ_{line} also has to be considered. A variation of the gas temperature between the typical values of 700 and 900 K results in a maximal deviation of the corresponding correction factors of a few per cent. A pressure variation between 1

and 6 mbar has almost no influence on the correction factor value over the whole α_{ik} l range due to the hyperfine splitting of indium. Moreover, the values of f_{WLABS} depend on the FWHM of the apparatus profile of the spectrometer. As this FWHM can be measured very accurately via OES the corresponding error is negligible. The error arising from the correction factors is estimated to be $\pm 15\%$, i. e. even very high correction factors can be trusted.

Remarks

It should be noted that an extended corona model is a very elementary approach to describe the population and depopulation of the excited indium states. The reabsorption of radiation which actually is important cannot be considered as this would require the knowledge of the A_{ik} -values for all optically allowed transitions from the $6\ ^2S_{1/2}$ and $7\ ^2S_{1/2}$ states to lower states which are not available in the literature completely. Furthermore, other possibly relevant processes such as radiative decay into the relevant states from higher states or quenching processes cannot be taken into account due to the lack of available cross section data. The calculation of the correction factors of reabsorption and saturation effects for the spectroscopic measurements is also based on simplifying assumptions regarding the line profile. Moreover, a Maxwellian EEDF has to be assumed for the calculation of the rate coefficients.

Despite the above listed assumptions and limitations of the extended corona model its utilization provides an access to the very important plasma parameters n_e and T_e . Without a knowledge of these parameters an investigation of the physical processes that determine the discharge characteristics of indium halide/rare gas discharges can only be carried out to a very limited extent. Even if the obtained absolute n_e and T_e -values might only have a limited significance, their relative trends already provide a very valuable information.

4.4 The Collisional-Radiative Model Yacora

Argon

An validation of the n_e and T_e values obtained from the extended corona model can be carried out by the utilization of the approved collisional-radiative model Yacora argon. If argon is used as background gas in the discharge, the determination of the electron temperature and density can be carried out from spectroscopic measurements of both argon and indium which allows for a benchmark of the n_e

and T_e -values obtained from the extended corona model of indium.

The collisional-radiative model Yacora argon calculates the steady-state population densities of the first 14 excited $1s$ and $2p$ states of the argon atom (given in Paschen notation) dependent on the ground state density, the electron temperature and density, the gas temperature and the pressure. A part of the energy level diagram of argon is shown in figure 4.6. The collisional-radiative model which is based on the numerical solver Yacora [WDF09] has been set up by [Die10] and includes the following processes: electron impact excitation and deexcitation (3.1), (3.2) & (3.3), spontaneous emission and reabsorption of radiation (3.6), electron impact ionization (3.7) and Penning ionization (3.9). The radiative decay of higher excited states is considered by using apparent electron impact excitation cross sections which include these processes implicitly. Furthermore the diffusion of metastable states to the wall is considered. However, reabsorption effects are only included in the form of population escape factors calculated assuming a pure Doppler and therefore Gaussian line profile as this model was originally set up for plasmas having pressures of a few Pa. If the model is applied to plasmas in the mbar range, it is necessary to consider the Lorentzian parts of the line profile which arise from natural and collisional line broadening

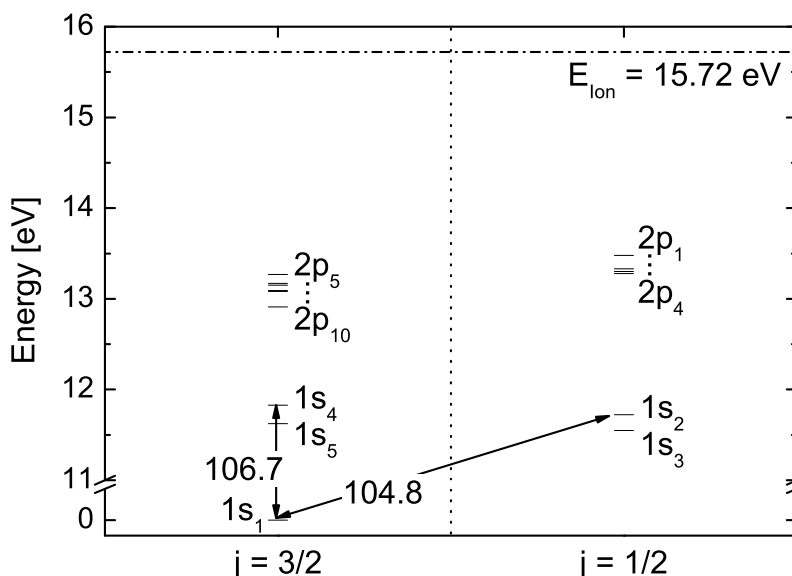


Figure 4.6: Part of the energy level diagram of argon based on the data from [Nat11]. The levels are given in Paschen notation. The $1s_3$ and the $1s_5$ states are metastable whereas radiative transitions between the $1s_2$ and the $1s_4$ states and the ground state can occur (these transitions and their central emission wavelength are plotted exemplarily).

for the transitions between the $1s_2$ and $1s_4$ state to the ground state which result in the lines at 104.8 and 106.7 nm [Nat11]. Therefore the population escape factors of these two lines have been calculated after equation (3.53) with a line profile that considers natural line broadening, pressure broadening and Doppler broadening (Stark broadening has been neglected). For all other lines which arise from transitions between the $1s$ and $2p$ states, it is sufficient to consider only Doppler broadening in the Θ_{pop} -calculation as the lower state is several orders of magnitude lower than the ground state. In the following, the input parameters for the profile-calculation of the 104.8 and 106.7 nm lines are summarized.

According to section 3.3.1, the FWHM of natural line broadening is determined by the radiance lifetimes of the participating states which is 2.15 and 8.6 ns for the $1s_2$ and the $1s_4$ state respectively [Law68]. The lifetime of the ground state is infinite and does therefore not contribute to natural broadening. The gas temperature which determines the FWHM of Doppler broadening besides the argon mass of 39.9 amu is given by the heating temperature of the discharge vessel (see section 5). As these lines are in the VUV spectral range, a direct measurement of the broadening coefficient γ/N has not been performed to the authors knowledge. But the FWHM of pressure broadening of a resonant transition can be calculated from the oscillator strength f_{ik} and the wavenumber ν_{ik} [cm^{-1}] of the transition [Fol46, CC74]:

$$\omega_{pressure} = \frac{1.45 e^2 f_{ik} n}{8m_e c^2 \nu_{ik}}, \quad (4.27)$$

where e denotes the elementary charge [C], m_e the electron mass [kg] and n the argon density which can be calculated from the filling pressure and the heating temperature of the vessel after the ideal gas law (see section 5). The units of the constant values of the above equation are traditionally chosen in a way that $\omega_{pressure}$ is given in [cm^{-1}]. The oscillator strength of the transition between the $1s_2$ ($1s_4$) and the ground state is 0.21 (0.051) [Val77]. This results in a broadening coefficients γ/N of $11.46 \times 10^{-20} \text{ cm}^{-1} \text{ cm}^3$ for the 104.8 nm line and $2.83 \times 10^{-20} \text{ cm}^{-1} \text{ cm}^3$ for the 106.7 nm line.

Determination of the Electron Temperature and Density

Via OES and white light absorption measurements of the lines shown in table 4.4 the population densities of the $1s$ and $2p$ states in the plasma can be obtained. On the other hand, these densities can also be calculated by the collisional-radiative model Yacora Argon with the following input parameters: n_e , T_e , T_{gas} and the

pressure. The gas temperature and the pressure are determined by the heating temperature of the vessel and the filling pressure (see section 5) after the ideal gas law. Therefore matching the absolute values of the calculated population densities to the measured ones yields the electron temperature and density. However, in doing so the measured densities have to be corrected due to saturation and opacity effects according to sections 4.2.2 and 4.1.2.

Input Data for Opacity and Apparent Optical Depth Correction

To consider reabsorption and saturation effects after equations (4.12) and (4.24) for the $1s \leftrightarrow 2p$ transitions, the line profile of each transition has to be calculated. In contrast to indium no hyperfine splitting has to be considered in argon as the nuclear spin is zero. For the calculation of the line escape factors and the correction factors f_{WLABS} the Lorentzian contributions to the line profile which arise from natural and collisional line broadening have to be considered for all measured transitions. The radiance lifetimes of the $1s$ and $2p$ states which determine the FWHM of natural broadening according to equation (3.44) are listed in table 4.4. The metastable $1s_5$ state has a very large radiance lifetime [KS93] and does therefore not contribute. The lifetime of the metastable $1s_3$ state is not available in the literature but can be assumed to be also very large. The FWHM of Doppler broadening is given by T_{gas} which equals the heating temperature of the discharge vessel (see section 5) and the atomic mass of argon which is 39.9 amu.

As mentioned in section 3.3 the FWHM of pressure broadening has to be derived for each transition individually. Table 4.5 shows the broadening coefficients of the relevant argon lines which have been measured at different gas temperatures (those of [Val77] at 3900 K, those of [THU82] at 300 K). The $(T_{gas})^{0.3}$ dependence of the broadening coefficients according to the Lindholm-Foley theory [Fol46, THU82] has been considered. The argon density which is needed for the determination of $\omega_{pressure}$ is derived from the filling pressure and the heating temperature of the discharge vessel (see section 5) after the ideal gas law. Again, Stark broadening has been neglected in the calculation of the line profiles.

The error of the corrected population densities of argon can be estimated in a similar way to the error of the indium densities (see section 4.3). As no hyperfine splitting occurs with argon, the impact of a pressure variation on the correction factor values is remarkable in general but not in the relevant α_{ik} l range (below unity). Therefore the correction factor errors can be estimated to be $\pm 15\%$.

Table 4.4: Radiance lifetimes of the relevant argon states and the wavelengths of the lines [Nat11] which are used to measure the population density of the listed states via OES or white light absorption spectroscopy (ABS).

State	Lifetime τ_i [ns]	Reference	Wavelength [nm]	Method
$1s_2$	2.15	[Law68]	840.8	ABS
$1s_3$?	—	794.8	ABS
$1s_4$	8.6	[Law68]	810.4	ABS
$1s_5$	38×10^9	[KS93]	811.5	ABS
$2p_1$	21.7	[WBD ⁺ 89]	750.4	OES
$2p_2$	28.3	[WBD ⁺ 89]	826.5	OES
$2p_3$	29.0	[WBD ⁺ 89]	840.8	OES
$2p_4$	29.3	[WBD ⁺ 89]	794.8	OES
$2p_5$	24.4	[WBD ⁺ 89]	751.5	OES
$2p_6$	29.4	[WBD ⁺ 89]	763.5	OES
$2p_7$	30.2	[WBD ⁺ 89]	810.4	OES
$2p_8$	30.6	[WBD ⁺ 89]	842.5	OES
$2p_9$	30.7	[WBD ⁺ 89]	811.5	OES
$2p_{10}$	40.5	[WBD ⁺ 89]	912.3	OES

Table 4.5: Pressure broadening coefficients of the relevant argon lines.

Wavelength [nm]	Broadening coefficient [$10^{-20} \text{ cm}^{-1} \text{ cm}^3$]	Reference
750.4	11.90	[Val77]
751.5	4.10	[Val77]
763.5	3.40	[Val77]
794.8	2.80	[Val77]
810.4	2.80	[THU82]
811.5	1.42	[THU82]
826.5	9.90	[Val77]
840.8	11.30	[THU82]
842.5	3.30	[Val77]
912.3	2.20	[Val77]

4.5 Simulation of the Indium Halide A – X and B – X Emission Spectra²

To investigate the vibrational and rotational population of the A and B state of the indium halides the relative intensity of the molecular emission arising from the A – X and B – X transition is calculated. By matching the simulated spectra to the measured ones by adjusting the input parameters for the simulation, the relative rotational and vibrational population is obtained. However, this is only possible with high accuracy if the spectral resolution of the experimental setup is sufficiently high [BF11]. If the relative vibrational population is known, effective transition probabilities can be derived according to section 4.1.1. This allows for the determination of absolute molecular population densities: the density of the A or B state via OES or the density of the ground state using white light absorption spectroscopy. Furthermore, as the A – X and the B – X transitions are simulated separately also the fraction of the emission which arises either from the A – X or the B – X transition can be calculated. This is important, as the emission spectra of the two transitions overlap strongly making an assignment of the emission bands to the particular transitions difficult. But this assignment is needed for the evaluation of spectroscopic measurements. The simulation program was initially set up for InBr [Bri08]. In this work, the simulation is improved to consider more population processes and the simulation is extended to InCl.

At very high InBr densities reabsorption effects occur [Bri08] but these effects cannot be considered in the simulation as data on the broadening of InBr emission lines are not available in the literature. If the shape of the InBr band is heavily distorted by opacity effects, a fit of the simulation to the measured intensity can no longer be performed.

4.5.1 Computing Method

The simulation of the relative molecular emission is based on the calculation of the relative rovibronic population densities of the X, A and B states of the indium halide molecule. In contrast to a population model, the relevant population and depopulation processes are only described by the simulation in a qualitative way. As the energy difference between the individual states is very low, it is necessary to take states with high vibrational and rotational quantum numbers into account.

²The explanations and remarks of this section especially on the calculation of Franck-Condon factors and transition probabilities of InBr have also been published [BF11].

For InBr, first investigations showed [Bri08] that for a good match of simulated and measured spectra the calculation must include the energetically lowest 25 vibrational states in the X, A and B state each having 300 rotational states. Significant deviations have been observed by reducing the maximum considered vibrational quantum number below $v = 20$.

Wavelength of the Single Emission Lines

The energy E of the rovibrational states of the X, A and B state is calculated according to the equations of section 3.2 using the molecular constants taken from [MYSR04]. The wavelength λ of a transition from a state described by the vibrational and rotational quantum numbers v' and J' in the upper electronic state i (A or B state) to a state v'' and J'' in the ground state X is derived from the energy difference of both states ΔE :

$$\lambda = \frac{hc}{\Delta E} = \frac{hc}{E_{i, v', J'} - E_{X, v'', J''}}. \quad (4.28)$$

Relative Population Density of the Upper State

As described in section 3.2, several processes can contribute to the population of excited electronic states. In the simulation it is assumed that the vibrational states of the A and B state are populated by electron impact excitation out of the ground state:

$$n_X^{v''} \xrightarrow{e^- \text{ impact exc.}} n_i^{v'}. \quad (4.29)$$

The energy difference between the vibrational states in the ground state is only about 0.03 eV ($\approx 300 \text{ K} \ll T_{gas}$). Therefore both inelastic collisions between the indium halide molecule and heavy particles (background gas, indium, bromine and chlorine respectively) or between indium halide and electrons can populate the vibrational states. In the simulation, both processes are considered assuming a Boltzmann distribution with the vibrational temperatures T_{vib}^{gas} and $T_{vib}^{e^-}$. These processes have different excitation rates depending on the cross section of the collision and the density of the collision partners resulting in a differing contribution to the vibrational population. However, cross sections for inelastic collisions between indium halides and heavy particles or electrons are not available in the literature. Despite the lack of data, the different excitation rates of these processes can be considered by weighting the population calculated with $T_{vib}^{e^-}$ relatively to

the population calculated with T_{vib}^{gas} :

$$n_{X,rel}^{v''}(T_{vib}^{gas}, T_{vib}^{e-}, \xi) = \tilde{n}_X^{v''}(T_{vib}^{gas}) + \xi \bar{n}_X^{v''}(T_{vib}^{e-}), \quad (4.30)$$

where ξ denotes the weighting factor. The resulting relative vibrational population in the ground state $n_{X,rel}^{v''}(T_{vib}^{gas}, T_{vib}^{e-}, \xi)$ is normalized in a way that the population of the whole ground state is unity:

$$\sum_{v''} n_{X,rel}^{v''}(T_{vib}^{gas}, T_{vib}^{e-}, \xi) = 1. \quad (4.31)$$

For the excited A and B state, the relative vibrational population $n_{i,rel}^{v'}$ is derived from the population of the ground state applying the Franck-Condon principle [FH98] as described in section 3.2.3:

$$n_{i,rel}^{v'} \propto q_{iX}^{v'v''} n_{X,rel}^{v''}(T_{vib}^{gas}, T_{vib}^{e-}, \xi), \quad (4.32)$$

where $q_{iX}^{v'v''}$ is the Franck-Condon factor for the transition X , $v'' \rightarrow i$, v' . Again the vibrational population is normalized to unity:

$$\sum_{v'} n_{i,rel}^{v'} = 1. \quad (4.33)$$

The relative rotational population $n_{i,v',rel}^{J'}$ of a state with quantum number v' is directly calculated in the excited electronic state i . This can be done as the rotational population is redistributed in the excited state via collisions with the background gas on a much shorter time scale than the radiative decay [Mul10]. Again a Boltzmann distribution of the rotational population is assumed which is described by the rotational temperature T_{rot} . The rotational population is also normalized to unity:

$$\sum_{J'} n_{i,v',rel}^{J'} = 1. \quad (4.34)$$

The relative population of the single state with quantum number v' and J' in the A or B state, $n_{i,rel}^{v',J'}$, is then given by

$$n_{i,rel}^{v',J'} = n_i^{v'} n_{i,v',rel}^{J'}(T_{rot}). \quad (4.35)$$

If the time scale for heavy particle collisions is short enough to allow for a rotational redistribution, also a redistribution of the vibrational population has to be

considered. However, laser induced fluorescence measurements proved [Mul10], that vibrational redistribution in the excited states via heavy particle collisions does not occur.

Relative Intensity of the Single Emission Lines

The relative intensity I_{rel} of a molecular emission line arising from a rovibronic transition ($i, v', J' \rightarrow X, v'', J''$) is given by

$$I_{rel} \propto \frac{n_{i,rel}^{v',J'}}{(2J'+1)} \nu_{iX} A_{iX}^{v',v''} S_{P,Q,R}(J'), \quad (4.36)$$

where ν_{iX} [s^{-1}] denotes the frequency of the emitted photon calculated according to equation (4.28), $A_{ik}^{v',v''}$ the vibrationally resolved transition probability and $S_{P,Q,R}(J')$ the Hönl-London factor for the P,Q or R branch [Her50]. As described in section 3.2.4, the Hönl-London factors depend on the Hund's coupling cases of the electronic states which are involved in the transition. As InBr and InCl are very heavy molecules Hund's case (c) is valid for both the A – X and the B – X transition [MYSR04]. Furthermore, both transitions are singlet – triplet transitions which means spin-orbit interactions may lead to perturbations in the intensity distribution of rotational lines [Kov69]. The formulae for the Hönl-London factors for the A – X and B – X transition can be found in [Kov69]. For their calculation constants describe the magnitude of perturbation due to the spin-orbit interaction are required. In the cases of InBr and InCl, these constants are not available in the literature. In general, Hund's case (c) is very similar to case (a) since the resultant angular momentum from the coupling of the single electronic and rotational angular momenta of the electronic state is the same in both cases [Her50]. Therefore the Hönl-London factors of Hund's case (a) which can be found in [Her50] and which do not require any special constants are used in the simulation as an approximation. Thus, spin-orbit interactions are neglected.

Resulting Band Spectrum

For each rovibronic transition line ($i, v', J' \rightarrow X, v'', J''$) a Gaussian line profile is calculated with the peak of the profile at the wavelength of the transition. The area of the Gaussian profile is equal to the relative intensity of the line emission. The FWHM of the Gaussian line profile is an input parameter of the simulation. Because mass of InBr and InCl is large, the FWHM of the Doppler profile is

much smaller than the apparatus profile of the optical system. Hence the FWHM used for the simulation is given by the apparatus profile which is determined by the experimental setup. The FWHM of the apparatus profile in the wavelength range of the indium halide emission bands is measured via OES utilizing the nearby indium lines. To obtain a spectrum, the intensities of all computed lines are added up. The relative intensities of the two electronic transitions can be adjusted separately to consider the possibility of a different electronic population of the A and the B state.

According to section 2.4, the InBr molecule basically has two relevant isotopic species, $^{115}\text{In}^{79}\text{Br}$ with a natural abundance of 48.52% and $^{115}\text{In}^{81}\text{Br}$ with 47.19%. Therefore, the emission is simulated for both species separately and then added, taking into account the natural abundances to obtain the final spectrum. The isotopes $^{113}\text{In}^{79}\text{Br}$ (2.17%) and $^{113}\text{In}^{81}\text{Br}$ (2.12%) are neglected.

For InCl also only two isotopes, $^{115}\text{In}^{35}\text{Cl}$ and $^{115}\text{In}^{37}\text{Cl}$ (natural abundance 72.51% and 23.20%), are considered in the simulation. The isotopes $^{113}\text{In}^{35}\text{Cl}$ and $^{113}\text{In}^{37}\text{Cl}$ (3.25% and 1.04%) are neglected due to their low abundance.

4.5.2 FCF and $A_{ik}^{v'v''}$ for InBr

The simulation requires vibrationally resolved Franck-Condon factors (FCF) and transition probabilities $A_{ik}^{v'v''}$ as input parameters. FCF of the InBr molecule can be found in the literature only for vibrational quantum numbers up to $v = 13$ [SRRR88] and radiative lifetimes can be found only for selected vibrational levels of the A or B state [KH07]. Therefore FCF and $A_{ik}^{v'v''}$ were calculated using the program TraDiMo [FW06]. This program derives the eigenvalues and vibrational wave functions via numerically solving the Schrödinger equation. The calculations are based on the Born-Oppenheimer potential curves, the electronic dipole transition moments and the reduced mass of the molecule as input parameters. The overlap integral of two vibrational wave functions in different electronic states yields the FCF according to section 3.2.3. The $A_{ik}^{v'v''}$ are calculated from the overlap of the vibrational wave functions with the electronic dipole transition moments. A more detailed description of TraDiMo can be found in [FW06].

There are three sets of potential curves for the X, A and B state of InBr available in the literature: RKR potential curves [SRRR88], Hulburt-Hirschfelder potential curves [MYRS03] and potential curves from quantum mechanical calculations [BPCD09]. The data for RKR potential curves are only given for vibrational quantum numbers up to $v = 12$. As already mentioned, for a good match of

the simulated spectrum and the measurement vibrational states up to $v = 24$ have to be taken into account. Hence, Morse potential curves were calculated using the molecular constants of InBr [MYSR04] which reproduced the RKR potential curves quite well. But Morse potential curves are only a very good approximation close to the minimum of the potential curve and therefore for low vibrational energies. However, the energy of the state with vibrational quantum number $v = 24$ of InBr is still rather low because of the large mass of the molecule. This can be seen in figure 4.7 where the Morse potential curves of the X, A and B state of InBr are shown together with the energy levels of some exemplary vibrational and rotational states. TraDiMo calculations were carried out with all three self-consistent sets of potential curves: with the Morse potential curves as extended fit to the RKR curves, with the Hulbert-Hirschfelder curves and with those from the quantum mechanical calculations. The electronic dipole transition moments $D_{AX}(r)$ and $D_{BX}(r)$ for the A – X and B – X transition are taken from [KH07]. They are empirically determined and given as:

$$D_{AX}(r) = D_{AX}(r_{eX}) \left[1 + 4 \cdot \left(\frac{r}{r_{eX}} - 1 \right) \right] \quad \text{and} \quad (4.37)$$

$$D_{BX}(r) = D_{BX}(r_{eX}), \quad (4.38)$$

where r_{eX} is the equilibrium nuclear distance of the ground state and $D_{AX}(r_{eX}) = 0.0705$ atomic units and $D_{BX}(r_{eX}) = 0.053$ atomic units [KH07]. Simulations were carried out with all sets of data and compared to measured emission spectra. The best match of the relative intensity of simulated and measured spectra by far were achieved with the data derived from the Morse potential curves.

In general, the potential curves are not dependent on the mass of the isotope. However, in the case of Morse potential curves, slightly different curves are obtained for the isotopic species as Morse potential curves are calculated with molecular constants as input parameters. Calculations of the FCF and $A_{ik}^{v'v''}$ have been carried out on the one hand with the appropriate mass of the corresponding isotope ($^{115}\text{In}^{79}\text{Br}$ or $^{115}\text{In}^{81}\text{Br}$) and on the other hand with the abundance-averaged mass. The simulation of the band spectrum using either the data gained considering the isotopic species or the averaged mass only differ in the range of a few percent. Nevertheless, the FCF and $A_{ik}^{v'v''}$ obtained with the appropriate isotope mass are used in the simulations³.

³They can be found online at http://www.physik.uni-augsburg.de/epp/FCF_and_Aik.pdf.

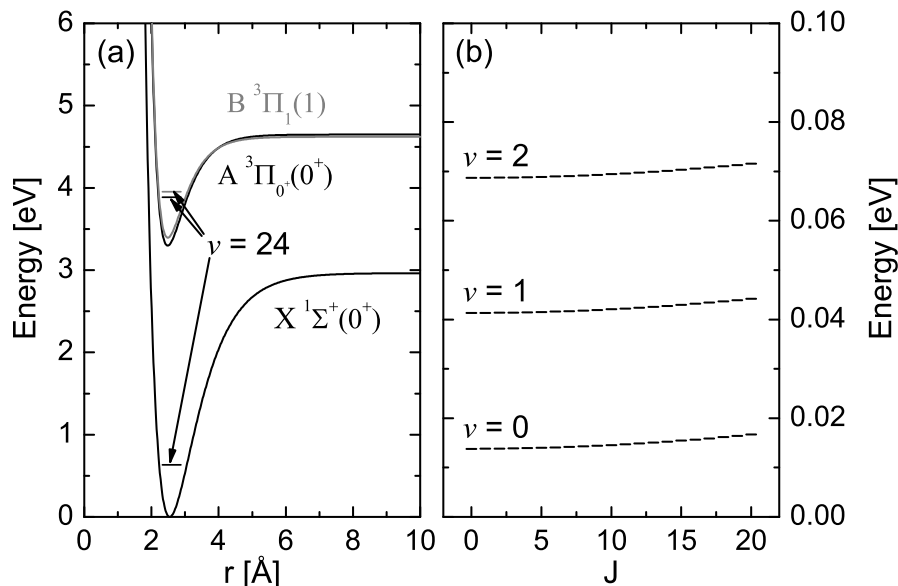


Figure 4.7: Part (a): Morse Potential curves of the X, A and B state of InBr calculated with the averaged isotopic mass. The energy of the state with vibrational quantum number $v = 24$ (and rotational quantum number $J = 0$) is plotted exemplarily for all electronic states. Part (b): Energy of rovibrational states in the electronic ground state of InBr with $v = 0, 1, 2$ plotted over J .

4.5.3 Fitting Procedure for InBr

The adjustment of the simulation to the measurement is basically done with the B – X transition of InBr as the details of the emission spectrum are slightly better reproduced than at the A – X transition. First of all, both the measured spectrum and the simulated one are normalized to the maximum intensity of the $\Delta v = +2$ sequence of the B – X transition. This sequence has a low intensity compared to the other sequences making distortions of the shape due to reabsorption unlikely as those effects occur first at the most intense transitions. After this step the $\Delta v = +1$ sequence of the B – X transition is used to adjust the rotational temperature of the B state T_{rot}^B . This sequence is ideal for this purpose as the different transitions $B, v' \rightarrow X, v''$ with $\Delta v = +1$ all have a very similar wavelength. Therefore, this sequence has only a slight vibrational structure and the shape of this sequence is almost independent on the vibrational population.

As InBr has a low vapour pressure at ambient temperature (see section 2.4), the intrinsically heating of the discharge vessel by the plasma is not high enough to evaporate a considerable amount of InBr which means the discharge vessel has to be heated up actively (see section 5). This results in $T_H \approx T_{gas}$ as also the heavy particles of the plasma are heated up. Hence, in the next step of fitting the

simulation to the measurement, T_{vib}^{gas} is set equal to the heating temperature of the discharge vessel, as it is assumed that the colder part of the vibrational population is excited due to heavy particle collisions. By varying T_{vib}^e and the weighting factor ξ the relative intensity and the vibrational structure of the particular sequences of the B – X transition are adjusted to the measurement. Afterwards the relative intensity of the A – X transition with respect to the B – X transition and the rotational temperature of the A state, T_{rot}^A , is adjusted. It turned out that T_{rot}^A always has to be 100 K higher than T_{rot}^B to achieve a good match. However, the energy difference of the rotational states in the A and B state is approximately the same. Therefore also the processes determining the rotational population in the excited electronic state should be the same. One reason for the deviation of T_{rot}^A and T_{rot}^B could be a slight inaccuracy of the molecular constants of the A state. These constants determine the energy of the particular rotational levels $F_v(J)$ in the simulation after equation (3.18). If $F_v(J)$ of the A state is slightly overrated in the simulation due to the inaccurate molecular constants, a higher rotational temperature is required to obtain the relative rotational population needed for a good match of simulation and measurement.

An exemplary fit of a measured spectrum together with the fitting parameters is shown in figure 4.8. The simulation reproduces the measured spectrum very well which implies that the assumptions made for the simulation, e. g. the use of the Hönl-London factors of Hund’s case (a) or using electron impact excitation out of the ground state as only population process, are reasonable. The errors of the obtained values are evaluated by varying the parameters until the simulation shows a remarkable deviation from the measured spectrum.

4.5.4 FCF , $A_{ik}^{v'v''}$ and Fitting Procedure for InCl

For InCl, neither vibrationally resolved Franck-Condon factors (FCF) nor transition probabilities $A_{ik}^{v'v''}$ can be found in the literature. Therefore they are calculated from potential curves and electronic dipole transition moments using the program TraDiMo [FW06]. Four different sets of potential curves for the relevant states of InCl are available: RKR potential curves [MYSR04], potential curves from quantum mechanical calculations [BD08, ZLYZ03] and those obtained by a pseudopotential approximation [SFD⁺95]. As the data for RKR potential curves are only available up to a vibrational quantum number of 16 they are fitted using Morse potential curves calculated from the molecular constants of InCl [MYSR04]. The electronic dipole transition moments are given by [BD08] and

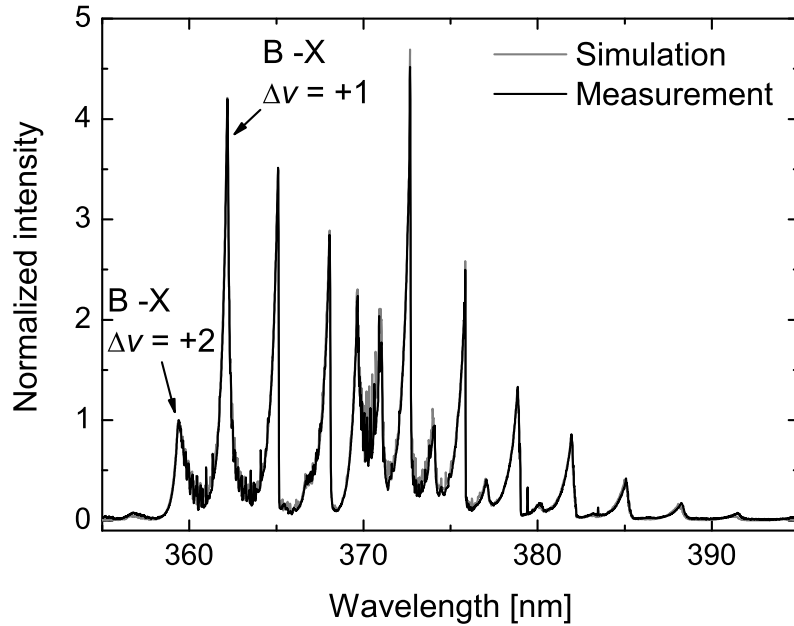


Figure 4.8: Measurement (axial LOS) and simulation of an exemplary InBr emission spectrum. The parameters of the simulation are: $T_{rot}^B = 900 \pm 50$ K, $T_{rot}^A = 1000 \pm 50$ K, $T_{vib}^{gas} = T_H = 830$ K, $T_{vib}^e = 2200 \pm 200$ K, $\xi = 0.35 \pm 0.1$. The relative intensity of the A – X transition is weighted with a factor of 1.01 ± 0.05 .

by [KH07]. Similar to InBr, simulations were carried out with all sets of obtained FCF and $A_{ik}^{v'v''}$ (calculated with the appropriate mass of the isotopes) and compared to measured emission spectra.

For the A – X transition a good match of the measured and simulated spectra can be achieved with the data derived using the Morse potential curves and the electronic dipole transition moments of [KH07]. They are given after equations (4.37) & (4.38) with $D_{AX}(r_{eX}) = 0.067$ atomic units and $D_{BX}(r_{eX}) = 0.071$ atomic units. The corresponding calculated FCF and $A_{ik}^{v'v''}$ values can be found online⁴. However, a satisfying match of the B – X transition could not be achieved at all. This can be seen in figure 4.9 where an exemplary measured spectrum and the fitted simulation is shown. The A – X transition reproduces the measured spectrum only if both T_{vib}^{gas} and T_{rot}^A are set differently from the heating temperature of the discharge vessel T_H . Furthermore, the values of T_{vib}^{gas} and T_{rot}^A also have to be set differently. However, as the populations described by T_{vib}^{gas} and T_{rot}^A are assumed to be caused by inelastic heavy particle collisions, these temperatures should coincide with T_H . A reason for the deviation of these tem-

⁴at http://www.physik.uni-augsburg.de/epp/FCF_and_Aik.pdf

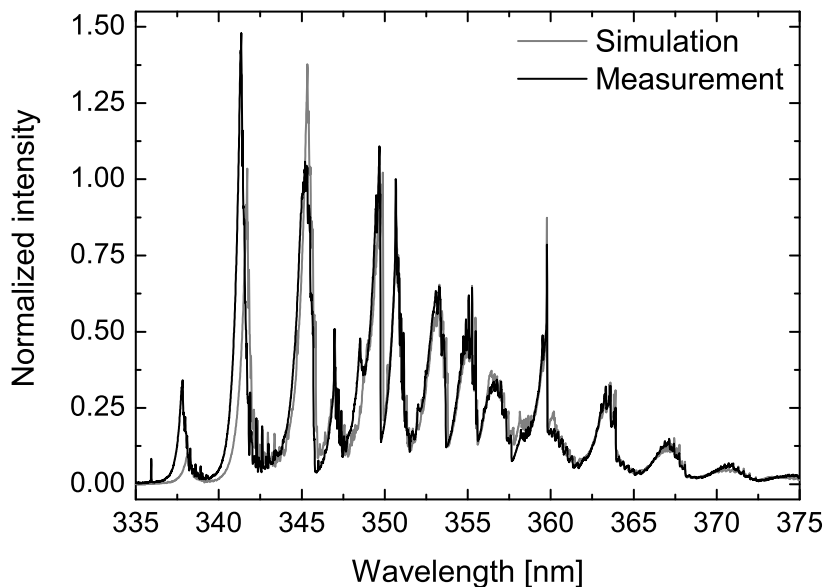


Figure 4.9: Measurement (axial LOS) and simulation of an exemplary InCl emission spectrum. The parameters of the simulation are: $T_{rot}^A = 1450 \pm 50$ K, $T_{vib}^{gas} = 1900 \pm 200$ K, $T_{vib}^e = 2500 \pm 300$ K, $\xi = 0.25 \pm 0.05$. T_{rot}^B and the weighting factor of the relative intensities of the A – X and B – X transitions cannot be determined due to the mismatch of the simulation and the measurement. The heating temperature of the discharge is $T_H = 800$ K.

peratures from T_H could be inaccurate values of the electronic dipole transition moments which greatly influence the transition probability values and therefore the relative intensity of the emission. For the B – X transition neither the wavelength of the emission nor the relative intensity could be matched with any input parameters. As the wavelength of the emission only depends on the molecular constants, the mismatch of the position of the sequences is caused by inaccuracies of these values. The mismatch of the relative intensities can be assigned to both inaccurate electronic dipole transition moments and molecular constants.

To summarize, the A – X transition can be simulated whereas the measured relative intensity from the B – X transition cannot be reproduced. However, for a good match of the A – X spectrum, rotational and vibrational temperatures have to be used that do not reflect the population processes assumed in the simulation. This limits the significance of the obtained relative rovibronic populations and in turn limits the population densities determined spectroscopically with the A – X transition for InCl. Despite these limitations, the simulation can still be used to obtain relative trends which allow for a qualitative investigation of the InCl population processes and densities.

5 Experimental Setup

5.1 Plasma Generation

Discharge Vessels and Fillings

Due to the high deliquescence of indium halides the discharges have been generated in sealed quartz vessels with a defined filling of indium halide and background gas. The cylindrical geometry of the vessel with an outer diameter of 25 mm is commensurate with conventional T8 fluorescent lamps. The cylinder is closed with quartz windows of optical quality at each end to allow for spectroscopic investigations in the visible and ultraviolet spectral range at an axial line of sight. The windows have a wall thickness of 2 mm whereas the wall thickness of the tube is 1.5 mm. The volume of the vessels is $6.1 \times 10^{-5} \text{ m}^3$. A sketch with the dimensions of the vessels can be seen in figure 5.1.

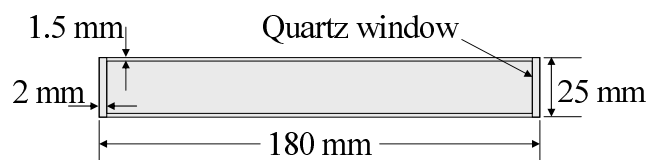


Figure 5.1: *Sketch of the discharge vessels.*

Previous investigations performed with a background gas pressure of 1, 2 and 2.5 mbar argon showed that lower pressures result in a more intense radiation from the indium halide and from indium [Bri08]. A further reduction of the pressure may again increase the radiation but this may also reduce the stability of the discharge which is a critical aspect especially if neon is used. To allow for systematic investigations of the background gases argon, neon and krypton a filling pressure of 1 ± 0.02 mbar has been used for all vessels. The filled amount of indium halide is an uncritical point as the evaporated amount in plasma operation is adjusted via the cold spot temperature. However, the amount should explicitly exceed the evaporated amount at the highest cold spot temperature of interest.

Otherwise a defined cold spot would not longer be assured. Therefore all vessels contain 1.5 ± 0.1 mg of indium halide which fulfils this demand [Bri08]. Table 5.1 gives an overview of the fillings of the different vessels. The purity of the filling of each vessel was checked by means of emission spectroscopy. This was done after one hour of plasma operation to evaporate possible impurities. No impurities were traceable in any vessel.

Table 5.1: *Fillings of the vessels.*

Amount of indium halide	Background gas
1.5 mg InBr	1 mbar argon
1.5 mg InBr	1 mbar neon
1.5 mg InBr	1 mbar krypton
1.5 mg InCl	1 mbar argon
1.5 mg InCl	1 mbar neon
1.5 mg InCl	1 mbar krypton

RF-Setup

To identify the most advantageous RF-coupling method for lighting applications both the inductively (ICP) and the capacitively (CCP) coupled plasma generation have been investigated (for details on the coupling see section 3.1). An RF-generator at a frequency of 13.56 MHz is used which has a tunable RF-power between zero and 300 W (Cesar 133 by Dressler). For the ICP setup which is shown in figure 5.2(a), a commercially available matching network is used (Variomatch 1500 W-ICP by Dressler). The plasma solenoid has 8 windings and is made out of a copper tube with an outer diameter of 6 mm and a wall thickness of 1 mm.

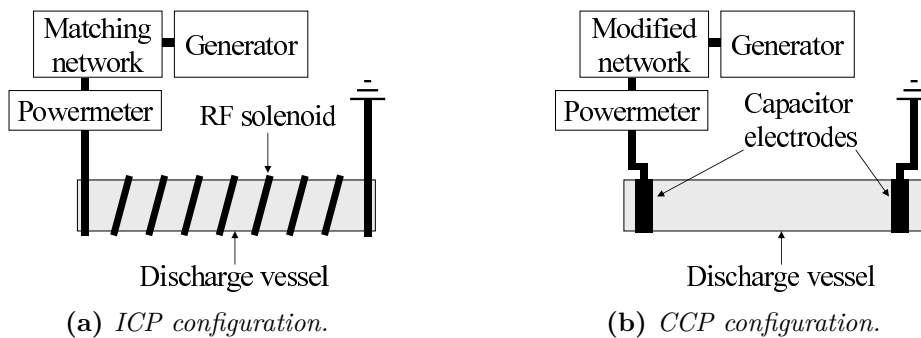


Figure 5.2: *Sketches of the RF-setup in ICP and CCP configuration.*

The CCP setup (shown in figure 5.2(b)) requires a different kind of matching network. Therefore a coil has been added to the ICP matching network which allows its utilization as CCP matching network. The capacitor electrodes are made of copper strand with a width of 15 mm and a thickness of 2 mm. The supply lines are made of copper tubes (outer diameter 6 mm, wall thickness 1 mm).

As a considerable amount of generator power may be dissipated in the matching network, a powermeter (V/I probe 350 by MKS instruments) is introduced in the RF-circuit to measure the power that is delivered to the plasma (measurement error $\pm 5\%$ [MKS97]). In the following the power is always defined as the delivered power measured by the powermeter and not the adjusted generator power.

5.2 Spectroscopic Setup

A sketch of the spectroscopic setup can be seen in figure 5.3 exemplary for ICP configuration. The discharge vessel has to be heated due to the low vapour pressure of the indium halides which makes a thermal insulation necessary (see section 5.3). To allow for spectroscopic measurements quartz windows in optical quality have been used with a wall thickness of 2 mm. The OES and white light absorption measurements have been carried out at an axial line of sight (LOS) which results in a detected discharge length of 176 mm. As light source for absorption spectroscopy a stabilized high pressure xenon discharge lamp (XBO 450 W/1 by OSRAM) has been used. For lighting applications the radial emission of the discharge is important. It is measured using a radial line of sight which results in a plasma length of 23 mm. The radial LOS is rotated slightly from the perpendicular direction to avoid blocking of the radiation by the windings of the plasma solenoid in ICP configuration.

The spectroscopic measurements of both lines of sight are performed using lens tubes to collimate the radiation into an optical fibre leading to the spectrometer. The lens tubes consist of a 2 mm aperture to limit the diameter of the LOS and a quartz lens with a focal length of 75 mm. The entrance aperture of the UV-enhanced optical fibre (diameter 400 μm) is placed in the focal point of the lens so that only light which enters the lens tube parallel to the optical axis is collimated into the fibre. This results in a limitation of the solid angle from which emission is detected which is important for calibration purposes.

A spectrometer in Czerny-Turner setup (Acton Spectra Pro by Princeton Instruments) with a focal length of 750 mm and a grating with 1800 grooves per

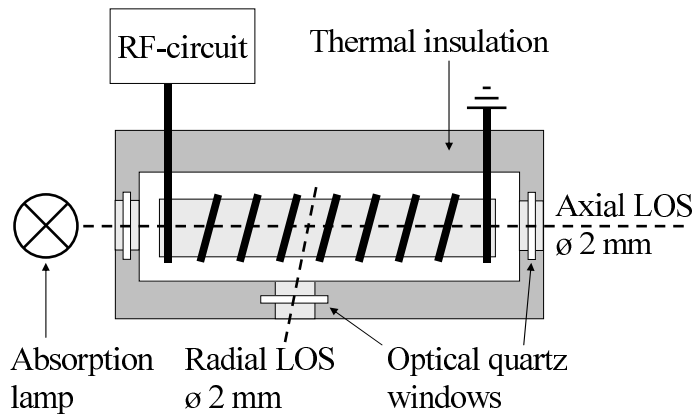


Figure 5.3: Sketch of the spectroscopic setup. The axial line of sight is used for the optical emission and absorption measurements whereas the radial LOS is only used to determine the radial radiation which is important for lighting applications.

mm is used for the spectroscopic measurements. The width of the entrance slit of the spectrometer influences the spectral resolution (smaller width is better) but also determines the transmitted intensity (larger width is better). A width of $30\ \mu\text{m}$ proved to assure a high resolution at a sufficient intensity. As detector an UV-enhanced CCD camera (NTE/CCD 2500×600 by Princeton Instruments) is used with a chip size of 2500×600 pixels each having a size of $12\ \mu\text{m} \times 26\ \mu\text{m}$. To minimize thermal noise the chip is cooled thermoelectrically to $-35\ ^\circ\text{C}$.

Due to the use of quartz lenses and a UV-enhanced optical fibre a wavelength range from 230 to 1000 nm can be investigated with this spectroscopic setup. To prevent the detection of higher diffraction orders of lower wavelength an edge filter is used for measurements above 520 nm. The filter can be placed in the lens tubes and only transmits light above 500 nm. The Gaussian apparatus profile of the setup is 26 pm at 300 nm decreasing to 16 pm at 850 nm.

Wavelength and Intensity Calibration

OES measurements require a wavelength and an intensity calibration of the spectroscopic setup whereas white light absorption spectroscopy only needs the wavelength calibration. The latter is carried out using a low pressure mercury discharge lamp. With the precise knowledge of the wavelength of several mercury lines [NIST] the calibration is performed using an internal routine of the spectrometer software.

The intensity calibration is performed using an integrating sphere, also known as Ulbricht sphere, and a deuterium arc lamp. An Ulbricht sphere is a diffuse

radiator which fulfils Lambert's cosine law and acts as a secondary measurement standard. The spheres can be purchased with a specified absolute emission. Hence, by measuring the radiation of an Ulbricht sphere with the utilized spectroscopic setup (the transmission of the quartz windows has to be considered) a calibration factor f_{cal} can be derived. As the emission from the Ulbricht sphere only ranges from around 390 nm to the infrared another measurement standard has to cover the UV spectral range. A deuterium discharge lamp is applied for this purpose which emits from the far UV into the visible range. As it is very elaborate to adjust the collimating optics correctly to the very small arc of the discharge lamp the deuterium lamp is only used to determine a relative calibration factor from 230 to 400 nm. The overlap between 390 and 400 nm of the two calibration factors is used to shift the relative UV calibration factor to the absolute value of the factor obtained from the Ulbricht sphere.

The calibration factor $f_{cal}(\lambda)$ [$1/(\text{m}^2 \text{ s nm} \{\text{counts/s}\})$] of the applied spectroscopic system which is normalized to one second integrating time can be seen in figure 5.4. It is used to calculate the number of photons radiated from the plasma $\epsilon_{photons}(\lambda)$ [$1/(\text{m}^3 \text{ s nm})$] into the whole solid angle from the measured intensity $I_{meas}(\lambda)$ [counts/s] and the plasma length l_{plasma} [m]:

$$\epsilon_{photons}(\lambda) = \frac{I_{meas}(\lambda) f_{cal}(\lambda)}{l_{plasma}}. \quad (5.1)$$

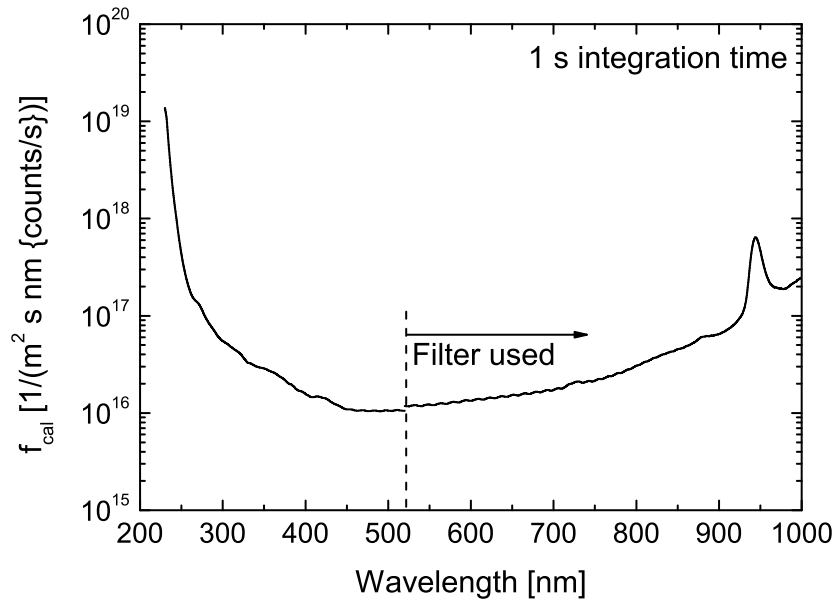


Figure 5.4: Calibration factor for the applied spectroscopic setup.

5.3 Cold Spot Setup

The evaporated amount of indium halide is determined by the coldest spot of the discharge vessel wall. To allow for an adjustment of the cold spot temperature the vessel is heated actively. However, by simply heating up the whole vessel the position of the cold spot is not well-defined. Increasing the heating temperature may then lead to a change of the cold spot location but not necessarily to a change in the cold spot temperature. To allow for systematic investigations of the dependence of the plasma parameters and the radiation on the evaporated indium halide amount an adjustable and well-defined cold spot is indispensable.

A sketch of this setup is shown in figure 5.5. The whole vessel is actively heated up via a hot air blower (LE Mini Sensor 800 by Leister/Klappenbach), keeping one spot of the vessel wall considerably cooler. The discharge vessel is placed inside a heat container which is made out of autoclaved aerated concrete to reach high heating temperatures. Using this material has proved to assure a good heat insulation. In addition the space for the discharge vessel and the diagnostic ports can easily be carved out. To define the cold spot a copper plunger is connected via thermal conductance paste to the vessel. The temperature of this spot is measured by a thermocouple that is placed in a small groove between the plunger and the vessel. A heat pipe is used to assure the thermal connection between the copper plunger and an aluminium cube that is placed outside the thermal insulation. Cooling the aluminium cube by a thermoelectric cooler or heating it by a heating wire allows for an adjustment of the cold spot temperature T_{CS} [°C].

It is important that the temperature that is adjusted with the cold spot setup really represents the coldest temperature of the vessel wall. Therefore the hot air heating temperature T_H [°C] has to be considerably above the adjusted cold

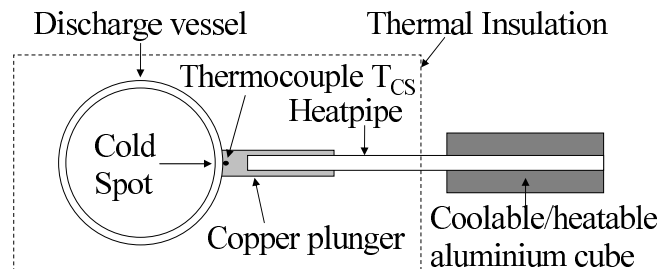


Figure 5.5: Sketch of the cold spot setup. The cold spot temperature T_{CS} can be adjusted by heating or cooling the aluminium cube.

spot temperature. T_H is determined by the averaged measured temperatures of three thermocouples inside the heat container. As the particular temperatures usually differ by ± 20 K, the error of T_H is estimated by this value. Figure 5.6 shows a sketch of the experimental setup where the position of the cold spot setup and the position of the thermocouples for the measurement of the heating temperature are shown. Experiments revealed that T_H must exceed the adjusted cold spot temperature at least by 150 °C to assure a proper operation of the cold spot setup. Furthermore, the plasma must fill out the whole volume of the discharge vessel, as the plasma heats the wall intrinsically. As T_{CS} is typically varied between 140 and 240 °C the heating temperature is kept above 500 °C in all measurements.

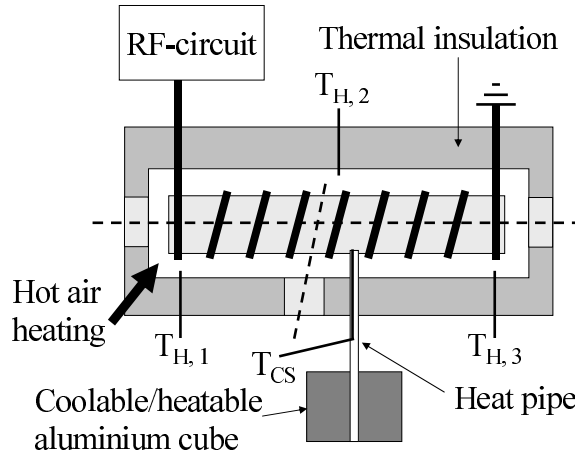


Figure 5.6: Sketch of the experimental setup with the positions of the thermocouples and the cold spot setup exemplary for ICP configuration.

Verification of the Performance of the Cold Spot Setup

To check the performance of the cold spot setup absorption measurements of the InBr band in gas phase were carried out. The vessel containing InBr and krypton was heated up to 500 °C and the cold spot temperature was varied between 250 and 305 °C as the absorption signal of the InBr band is below the detection limit for $T_{CS} < 240$ °C. Figure 5.7 shows a comparison between the ground state density derived from absorption measurements and the InBr density calculated with T_{CS} , the ideal gas law assuming $T_{gas} = T_H$ and the different vapour pressure curves ([SL60, KH07, TRBO89], see section 2.4). The effective transition probabilities which are needed for the evaluation of the absorption measurements are calculated after equation (4.8) assuming a Boltzmann distribution of the vibrational states according to the heating temperature. As expected from a well-defined

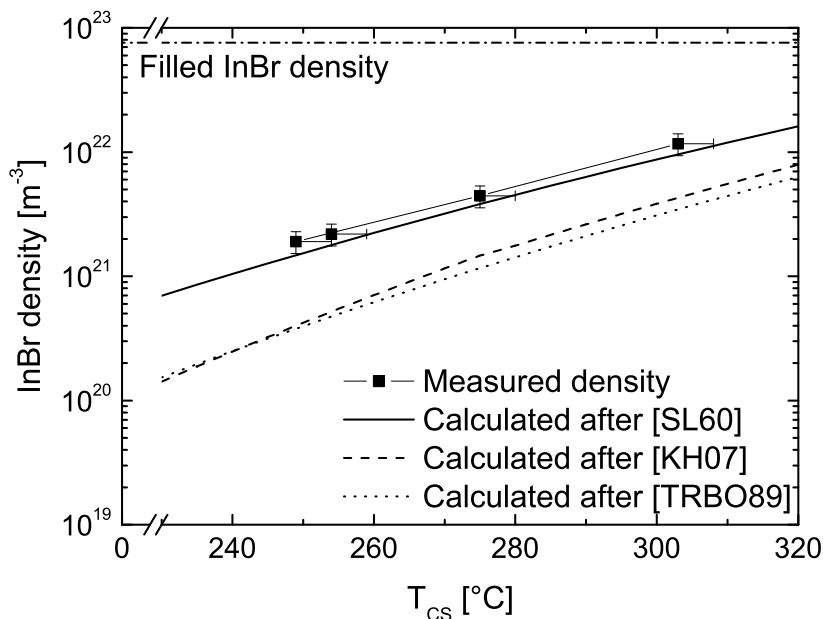


Figure 5.7: *InBr* density measured with absorption spectroscopy without plasma operation (vessel with 1 mbar Kr) compared to density calculated after the vapour pressure curves of different references. The heating temperature was 500 K.

cold spot setup, increasing T_{CS} results in an increase of the measured density. The experimental error of the density from absorption measurements is estimated to be $\pm 20\%$. It can be seen that the *InBr* densities obtained after the vapour pressure curve from [SL60] are within the errors of the measured densities whereas the other two vapour pressure curves are at least a factor of three too small. If one of these two curves was correct this would imply a very large error of the cold spot temperature measurement of at least 30 °C which is not reasonable. Therefore the evaporated *InBr* density is calculated after the vapour pressure curve of [SL60] in the following.

Further measurements showed that during several days of plasma operation the thermal conductance paste degrades which results in an underestimation of T_{CS} (more *InBr* is evaporated than expected). Hence it is necessary to connect the copper plunger to the vessel with thermal conductance paste each time prior to measurements. This assures a proper operation of the cold spot setup.

It can be summarized that the main goal of the cold spot setup is achieved: allowing for a controlled adjustment of the evaporated *InBr* density. According to the absorption measurements the error of T_{CS} in gas phase measurements is estimated to be +5 °C as drawn in figure 5.7. As the plasma also heats the vessel and hence influences T_{CS} the error in plasma operation is estimated to be +10 °C.

6 Investigation of the RF-Coupling Method

As described in section 3.1 the capacitive RF-coupling method permits a design of the lamp and its fitting that is very similar to conventional fluorescent lamps which reduces the necessary effort required for replacing those lamps. Inductively coupled discharges however usually generate a more intense light output than CCPs due to the higher coupling efficiency. On the other hand, high efficiencies are reported for capacitively coupled indium halide/rare gas discharges [HHK⁺10]. In order to investigate the potentials of both RF-coupling methods for rare gas plasmas with indium halide additives a systematic spectroscopic investigation of the light output obtained from CCP and ICP coupling at the same experimental parameters has been performed.

6.1 Using Sealed Discharge Vessels

Earlier investigations showed that inductively coupled InBr/rare gas plasmas (experimental setup of figure 5.2 (a)) provide a high axial uniformity and a high light output [Bri08]. A picture of the ICP discharge is shown in figure 6.1 exemplarily at low cold spot temperature T_{CS} . To compare the uniformity and the light output of the ICP to those of a CCP for the same experimental parameters, the CCP setup shown in figure 5.2 (b) was used. If T_{CS} is low, i. e. very little InBr is evaporated, the uniformity of the CCP-discharge is distorted: A strong alternation of the intensity occurs as shown in figure 6.2. This phenomenon is called “striations” and is caused by ionization and diffusion instabilities in the discharge



Figure 6.1: *Picture of the uniform emission from an ICP InBr/argon discharge.*



Figure 6.2: Picture of the striations appearing in a CCP InBr/argon discharge at low T_{CS} .

[Kol06]. The formation of striations strongly depends on pressure, coupling method and the plasma parameters [LMP80, Kol06]. If the InBr density is increased by increasing the cold spot temperature (which results in changing plasma parameters, see section 7.1), the striations disappear completely and the discharge turns uniform similar to figure 6.1. Therefore measurements in CCP-mode are restricted to high cold spot temperatures above 150 °C).

However, systematic investigations of InBr/rare gas CCP discharges could not be performed due to their lack of temporal stability. In figure 6.3 the temporal evolution of the InBr emission integrated from 350 to 400 nm measured along the axial LOS (see figure 5.3) is plotted. The filling of the discharge vessel was 1 mbar argon and 1.5 mg InBr, the RF-power was 58 W and the cold spot temperature was set to 200 °C to avoid striations. Quickly after adjusting T_{CS} to the desired value at $t = 0$ InBr evaporates which results in an increase of the InBr emission

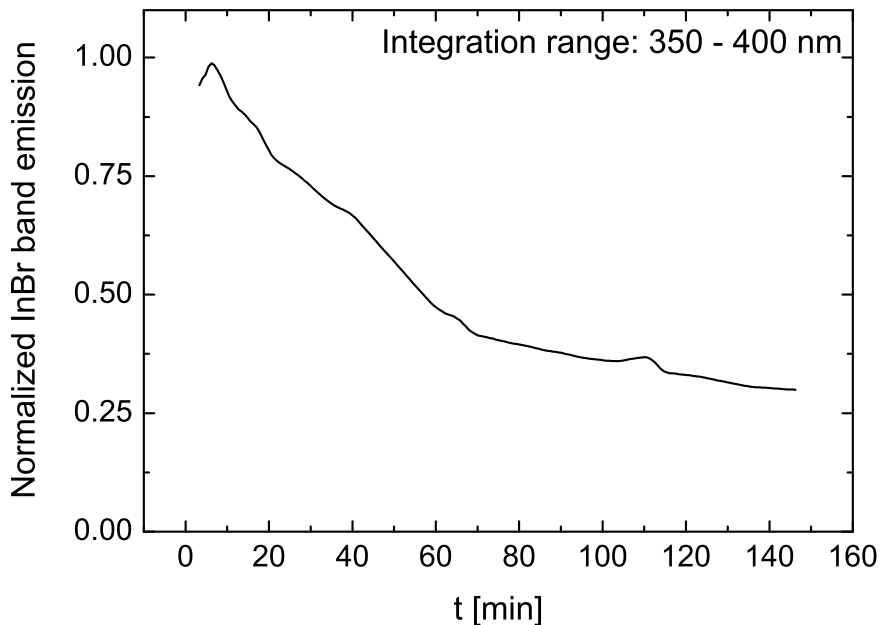


Figure 6.3: Time dependent InBr band emission in CCP-operation (vessel filled with 1 mbar argon and 1.5 mg InBr, RF-power 58 W, $T_{CS} = 200$ °C).



Figure 6.4: *Picture of the blackening of the inner wall of the discharge vessel in the region of the CCP-electrode.*

for a few minutes. This increase is followed by a steady decrease of the emission which lasts for more than two hours. Disassembling the setup revealed a strong blackening of the inner side of the discharge vessel especially in the region of the CCP-electrodes (see figure 6.4).

A chemical analysis [Wei08] proved that the metallic film that is deposited at the inner wall of the discharge vessel consists of atomic indium. The result was confirmed by EDX-measurements [Kör09] which revealed that indium is rather implanted into the quartz glass of the wall than only deposited onto the surface during CCP-operation. This can be explained as follows: In the discharge indium ions (besides other ions) are generated due to dissociation and ionization processes. If the ions reach the RF-sheaths at the CCP-electrodes they are strongly accelerated as explained in section 3.1. During this process the ions can reach kinetic energies which allow for an implantation into the quartz substrate. The implanted indium amount can be considered lost as a recombination with atomic bromine to InBr is strongly reduced. This leads to a constant reduction of the InBr and indium density in the discharge which had been observed in the measurement.

Reducing the RF-power can result in a reduction of the sheath voltage [LL94] which in turn reduces the kinetic energy of the indium ions. At low RF-powers, the kinetic energy which is needed to implant the indium ions into the quartz glass might not be reached. Investigations at 48 W and 19 W RF-power have been performed which both showed a complete loss of InBr after several hours of operation and strong blackening of the discharge vessel. A further reduction of the RF-power is not possible with the experimental setup used in this work. But it should be noted that in [HHK⁺10] CCP indium halide/rare gas discharges had been investigated at very low RF-powers of 1.5 to 4 W. However, no information about the long-term stability of the indium halide density is available.

6.2 Using a Variable Vacuum Setup

Since the capacitive coupling does not allow for systematic investigations of discharges containing indium halides, a comparison of CCP and ICP discharges with respect to the generated light output has been performed using rare gas plasmas. For this purpose a vacuum setup has been assembled where the gas is supplied using a mass flow controller, as a variation of pressure and gas type would require a large amount of sealed discharge vessels. A sketch of the setup is shown in figure 6.5. The pressure is adjusted by reducing the pumping rate of the pumping station which consists of a turbomolecular pump and a membrane pump. The background pressure is measured using a cold cathode pressure gauge and the operating pressure is determined by a capacitive pressure gauge which measures independently of the gas type. The discharge vessel which is connected to the vacuum setup by a connection flange has the same dimensions as the sealed vessels which allows for the use of the same RF-setup. To reduce the background pressure and therefore the impurities, the vacuum setup is baked out at 80 °C for several days. After the bake-out procedure the achieved background pressure is in the range of 10^{-7} mbar. The investigations are carried out in steady-state operation, which means both the gas supply and the pumps are separated by closed valves from the discharge vessel and the pressure gauges.

The spectroscopic investigation concerning the light output at CCP and ICP operation has been carried out at the axial line of sight (see figure 6.5). As the occurrence of striations can influence the measured radiation output strongly, care

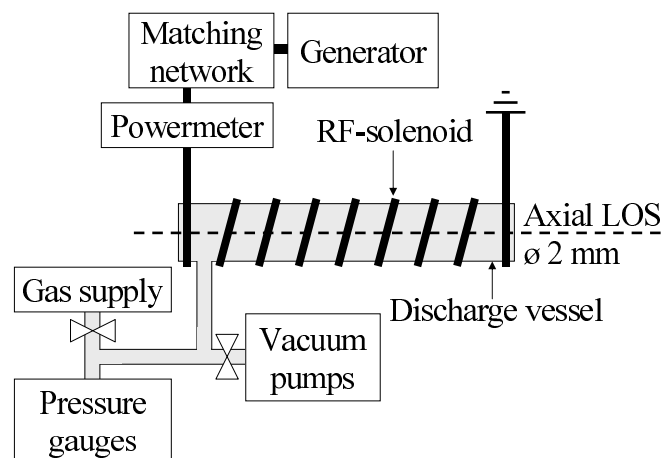


Figure 6.5: Sketch of the vacuum setup used for the systematic investigations of CCP and ICP rare gas discharges. The setup is shown exemplarily in ICP configuration.

should be taken to avoid this effect. In CCP-mode striations appeared with all background gases except for argon; therefore the systematic comparison between CCP and ICP is solely carried out using argon discharges. In the following, the emissivity I_{ik} of the argon line at 750.4 nm is used as representative benchmark of the generated light output.

The variation of the RF-power and the pressure could only be performed within certain thresholds which depend on the rare gas type: At high power (for argon above 80 W) and at low pressure (below 1 mbar), the plasma volume expanded through the connection flange from the discharge vessel into the vacuum setup. If this happens, the RF-power is coupled into a much larger plasma volume which results in changing plasma parameters according to section 3.2.7. At low power (threshold value dependent on coupling method and pressure) and at high pressure (above 10 mbar), the plasma constricts which also changes the plasma volume. To allow for a comparison of the radiation output, care has been taken for both CCP and ICP operation that the plasma volume fills out the whole discharge vessel and does not expand through the connection flange.

The dependence of the emission on the pressure between 1 and 10 mbar at a constant RF-power of 80 W is shown in figure 6.6(a). The plotted errors arise from the error of the spectroscopic measurement of $\pm 10\%$ (see section 5.2). In CCP-mode, an increase of the pressure from 1 mbar to 3 mbar results in an increase of I_{ik} of almost one order of magnitude. Further increasing the pressure leads to a stagnancy of the emissivity. Using inductive coupling results in a high emissivity at low pressure and a decrease with increasing pressure. The maximum absolute value achieved in ICP-mode (at 1 mbar) is almost one order of magnitude higher than the maximum value of the emissivity in CCP-mode (between 3 – 10 mbar).

The emissivity of the argon line at 750.4 nm at varying RF-power is shown in figure 6.6(b). The pressure has been chosen according to the maximum emission at 80 W RF-power: 1 mbar for ICP and 3 mbar for CCP coupling. The low-power operation threshold is located at 15 W for CCP and at 50 W for ICP operation. It can be seen that the absolute emissivity is much higher with inductive coupling and that a decrease of the RF-power results in a decrease of the emissivity for both coupling methods. However, the decrease in CCP-mode is much stronger than in ICP operation. As described in section 3.2.7, a decrease of the input power results in a decrease of the product $V_{plasma}n_e$. As care has been taken that V_{plasma} is constant, the decrease of the emissivity can be assigned to be caused by a smaller excitation rate of argon atoms due to a decrease of the electron density.

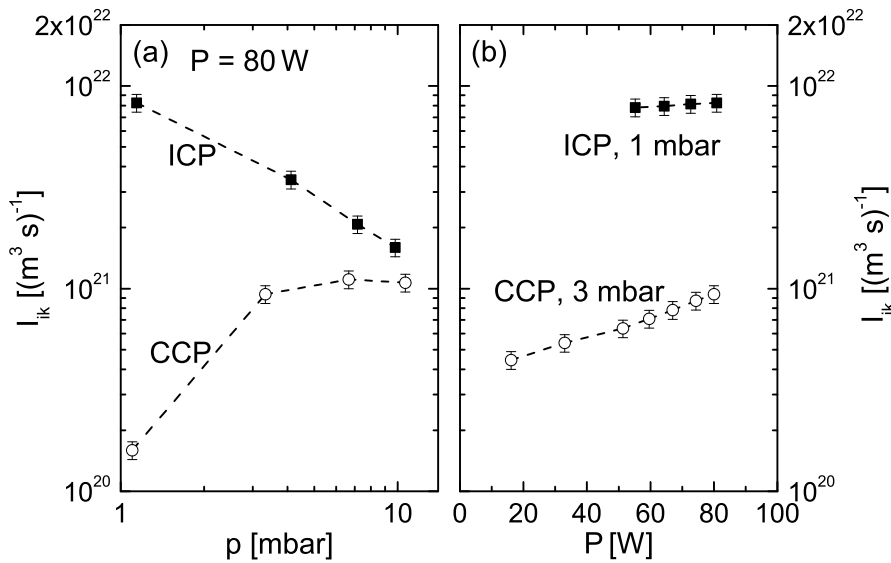


Figure 6.6: Emissivity of the argon line at 750.4 nm (axial line of sight) dependent (a) on the pressure and (b) on the power for CCP and ICP operation.

To summarize, the inductive coupling method for the generation of indium halide discharges for lighting applications has two beneficial characteristics compared to capacitive coupling: First, the implantation of indium ions into the quartz glass wall of the discharge vessel does not occur. Second, the generated light output at same input power is much higher. On the other hand, a CCP allows for a larger RF-power operating range at low powers. However, as the low-power threshold depends on the pressure and rare gas type, the threshold can also be expanded to about 15 W for ICP operation if krypton or xenon is used at 1 mbar instead of argon. Therefore, inductive coupling is used for the following fundamental investigations of indium halide discharges.

7 Investigation of InBr as Radiating Species

7.1 Variation of the Cold Spot Temperature

Preliminary investigations proved that the amount of evaporated InBr which is determined by the cold spot temperature T_{CS} has a strong influence on the discharge characteristics [Bri08]. Most evident is the change of the plasma emission: at low InBr density, the radiation is dominated by a variety of argon lines (primarily above 700 nm) which results in a pink colour of the discharge emission. Increasing T_{CS} causes a vanishing of the argon emission and a strong increase of the emission arising from InBr (between 350 and 400 nm) and indium (especially the lines at 410.2 and 451.1 nm) which is generated by dissociation processes in the plasma. The emission of bromine is generally very weak and can be neglected. As the emission of InBr is in the near UV spectral range and is therefore not visible, the plasma emission has a bright blue colour arising from the indium emission. In an InBr/In dominated discharge, the amount of light output is distributed between the InBr band, the indium line at 410.2 nm and the one at 451.1 nm each having a share just under one third. The share of the other indium emission lines which are primarily located between 270 and 330 nm is roughly 10%. Therefore the efficiency considerations of the generated radiation are focused on the InBr band and the two indium emission lines at 410.2 and 451.1 nm. Nevertheless, for lighting applications the whole emission can be utilized.

However, the results on the discharge characteristics with varying T_{CS} described in [Bri08] were obtained without a defined cold spot setup, which means T_{CS} could not be adjusted in a controlled way. Furthermore the determination of the electron temperature was based on an estimated and fixed value of the electron density and reabsorption or saturation effects were not considered in the spectroscopic determination of the population densities. Therefore, an InBr/argon discharge (vessel with 1 mbar pressure and 1.5 mg InBr, $T_H = 550$ °C) at 100 W

RF-power was again investigated within the scope of this work with the defined cold spot setup described in section 5.3. The possibility of deriving T_e and n_e from spectroscopic measurements and the further development of the relative-intensity simulation of the InBr emission allows for a more detailed understanding of the physical processes determining the light output and the efficiency of the discharge.

Densities of InBr and Indium

The evaporated amount of InBr is determined by the cold spot temperature. Since the value of T_{CS} is known, the InBr density in gas phase can be calculated with the vapour pressure curve from [SL60] and the heating temperature T_H of the discharge vessel after the ideal gas law. If the cold spot temperature is increased, more InBr evaporates which is shown in figure 7.1. It should be noted, that the calculated volume-averaged InBr density can only be used as estimate for the ground state density as excitation, dissociation and ionization processes occur in the plasma. A direct measurement of the ground state density via white light absorption spectroscopy is not possible, as the evaporated amount is below the detection threshold.

Also the indium ground state density which is measured via white light ab-

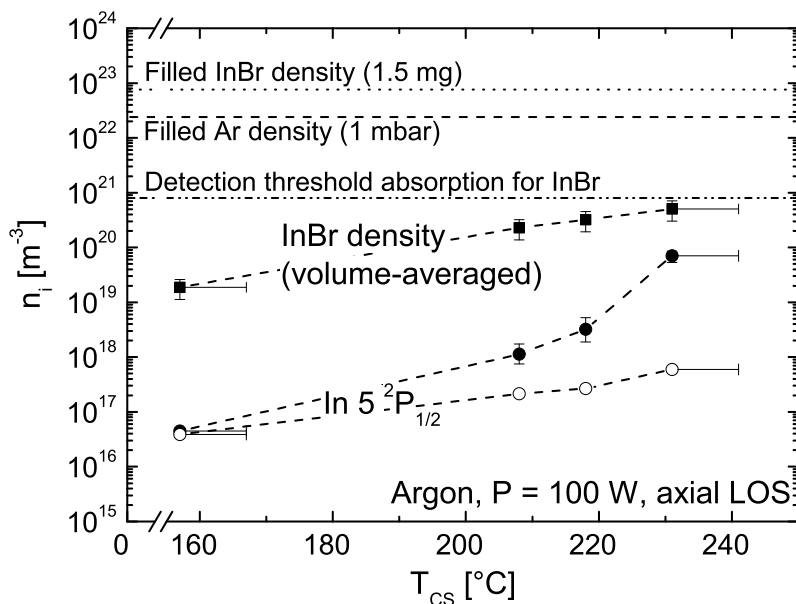


Figure 7.1: Volume-averaged density of InBr (calculated after the vapour pressure curve and the ideal gas law) and ground state density of indium measured via white light absorption spectroscopy (open symbols without and filled symbols with considering saturation effects) at varying T_{CS} .

sorption spectroscopy at the axial line of sight increases with increasing T_{CS} (see figure 7.1). This can be explained by the increasing dissociation rate of InBr which in turn results from the increasing InBr ground state density. The influence of saturation effects on the determined indium ground state density is also demonstrated in figure 7.1: The open symbols show the density without considering saturation, whereas the filled symbols show the values obtained with considering saturation effects. It can be seen that neglecting these effects at low cold spot temperature does not affect the obtained density as the optical depth is low and f_{WLABS} is almost unity. However, at high T_{CS} a negligence of saturation leads to an underestimation of the ground state density of In by about two orders of magnitude which proves the necessity of considering saturation effects.

Electron Temperature

The electron temperature of the discharge is determined with the extended corona model of indium (see section 4.3). To validate these results the collisional-radiative model Yacora argon (see section 4.4) has been utilized at low T_{CS} where the discharge emits radiation both from indium and argon.

Figure 7.2 shows the obtained electron temperature values. Saturation and

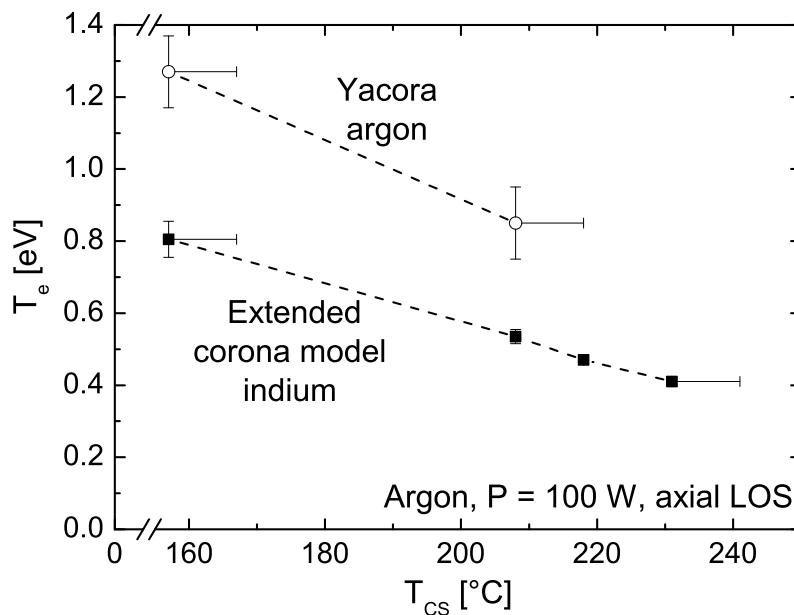


Figure 7.2: Electron temperatures obtained from the extended corona model of indium (filled symbols) and from the collisional-radiative model Yacora argon (open symbols) at varying cold spot temperature.

reabsorption effects have been considered for all spectroscopic measurements. The plotted errors arise from the evaluation of the population models. Increasing T_{CS} results in a decrease of the electron temperature both for the values obtained from the extended corona model of indium and from Yacora argon (the deviation of the absolute values is discussed below). This trend can be explained with the ionization balance according to section 3.2.6.

At low cold spot temperatures, the contributions of In, Br and InBr to the ionization balance can be neglected, as their density is too low compared to argon. Hence, the ionization balance is dominated by argon. If the cold spot temperature increases, more InBr is evaporated as shown in figure 7.1. This also results in an increase of the indium and bromine density in the plasma due to dissociation processes. Therefore, the contribution of indium, bromine and InBr to the ionization balance becomes more important, i. e. the occurrence of the corresponding ions must be considered. In general, the formation of bromine ions can be neglected as the ionization rate of bromine is much smaller than the one of indium due to the higher ionization energy of bromine. As $n_e = \sum_j n_{ion}^j$ has to be fulfilled, the occurrence of other ions leads to a decreasing amount of argon ions. Hence, an increase of T_{CS} causes a partial substitution of light-weight argon ions which have a large ionization energy by heavy-weight In and InBr ions which have a smaller ionization energy (the corresponding masses and ionization energies are given in table 7.1). According to section 3.2.6 this results in a decrease of T_e .

Table 7.1: Ionization energies and masses of indium, InBr and argon.

Species	Mass [amu]	E_{ion} [eV]	Reference
Indium	114.82	5.79	[San05]
Bromine	79.90	11.81	[San05]
InBr	194.72	9.41	[Lid05, BD72]
Argon	39.95	15.76	[San05]

The absolute values of T_e obtained with the collisional-radiative model of argon are higher than the ones obtained with the extended corona model of indium as shown in figure 7.2. As described in section 4.4 the collisional-radiative model Yacora argon considers all relevant population and depopulation processes for the 1s and 2p states. This is not necessarily the case for the extended corona model for indium as explained in section 3.2.5. Disregarding relevant population (depopulation) process for the indium states can result in a overestimation (underestimation) of T_e . If it is assumed that no additional processes have to be

included in the extended corona model to describe the steady-state population densities correctly, a non-Maxwellian EEDF of the discharge could still lead to the observed divergence of the absolute T_e -values.

The impact of a non-Maxwellian EEDF on the T_e determination is demonstrated exemplarily with a so-called Bi-Maxwellian EEDF [GMS95]. Such an EEDF is described by two temperatures, $T_{e,1}$ characterizing the EEDF in the low-energy range and a higher temperature $T_{e,2}$ characterizing it in the high-energy range. The excitation energy of the electronic states determines which temperature characterizes the population process via electron impact excitation. The indium states which have rather low excitation energies ($3.0 \leq E_{exc}^{In} \leq 4.5$ eV [GGV90]) could be populated according to $T_{e,1}$ whereas the argon states ($11.5 \leq E_{exc}^{Ar} \leq 13.5$ eV [San05]) could be populated according to $T_{e,2}$. Therefore, a determination of T_e according to the measured population densities of excited indium states results in a lower value than the one obtained according to the measured densities of the argon states. Other EEDFs which follow more complex distributions like the Druyvestein distribution [DP40] can also lead to the described deviation of the obtained electron temperatures.

Despite the deviation of the absolute values of T_e obtained from the extended corona model of indium and from the collisional-radiative model Yacora Argon, the electron temperature can still be used for statements on the T_e dependency of the discharge characteristics. This can be done as the relative T_e trends obtained from the extended corona model could be validated.

Electron Density

The electron density of the discharge is also determined spectroscopically using the extended corona model of indium (see section 4.3) and the collisional-radiative model Yacora argon (see section 4.4). The values of n_e at varying cold spot temperature obtained with the two methods are shown in figure 7.3. In contrast to the electron temperature where the values obtained with the two methods differ from each other, the electron density agrees well within the errors which arise from the evaluation of the population models.

To explain the increase of n_e with increasing cold spot temperature, the power balance has to be considered according to section 3.2.7. The quantitative dependencies of $V_{plasma}n_e$ in the InBr/argon discharge can be discussed after equation (3.37) which indicates that the value of $V_{plasma}n_e$ is proportional to the product of the input power and the ion-confinement time. As the plasma fills out the whole

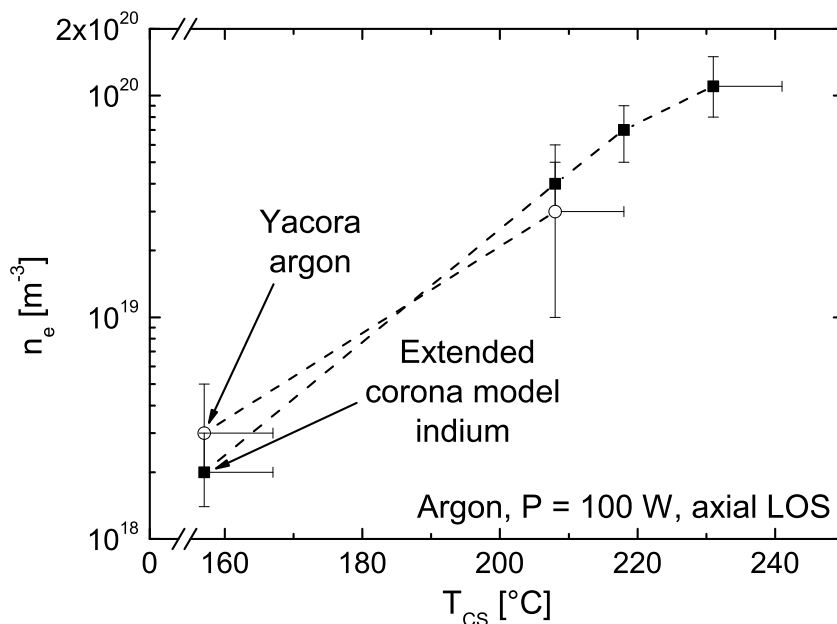


Figure 7.3: Electron densities obtained from the extended corona model of indium (filled symbols) and from the collisional-radiative model Yacora argon (open symbols) at varying T_{CS} . The larger error at $T_{CS} = 208$ °C corresponds to n_e obtained from Yacora argon.

discharge vessel at the performed investigations, V_{plasma} stays constant. Furthermore, the RF-power is kept constant at 100 W. Together with the definition of the confinement time τ_{ion}^{lam} (see equation 3.11) this yields:

$$n_e \propto \tau_{ion}^{lam} \propto \frac{\sqrt{m_{ion}}}{T_e}. \quad (7.1)$$

As described in the previous section, an increase of T_{CS} results in a partly substitution of light-weight argon ions by heavy-weight indium and InBr ions. Moreover, the electron temperature decreases with increasing cold spot temperature. According to equation (7.1), both trends lead to an increase of n_e .

Population Densities of Excited States

Figure 7.4 shows the population densities of the exemplary indium $6^2S_{1/2}$ and argon $1s_2$ states and the population densities of the InBr A and B state determined via OES or white light absorption spectroscopy respectively. Saturation and reabsorption effects are considered for the indium and argon densities. The effective transition probabilities required for the determination of the InBr states have been calculated after section 4.1.1 while the relative vibrational population and

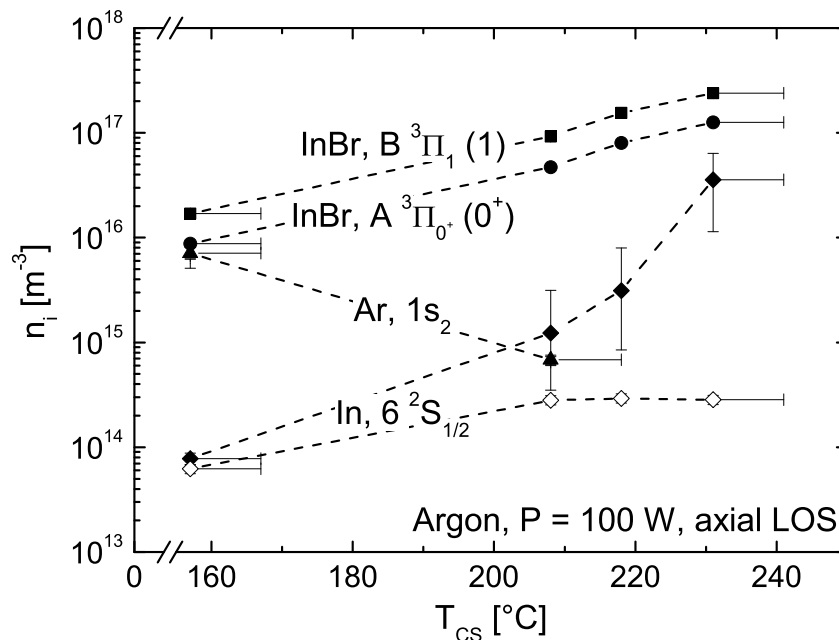


Figure 7.4: Population densities of the indium $6^2S_{1/2}$, the argon $1s_2$ and the A and B states of InBr measured at the axial LOS with varying T_{CS} . For the population density of indium the filled (open) symbols show the obtained values with (without) considering reabsorption effects.

the share of the emission between 350 and 400 nm arising from the A – X or from the B – X transition have been obtained from fitting the simulated InBr emission to the measured spectrum according to section 4.5.3. Above $T_{CS} \approx 210$ °C a determination of the population densities of the $1s$ and $2p$ states of argon was no longer possible as the emission and absorption signals were too low. It should be noted, that reabsorption effects are not considered for the population density of the InBr states because the required data on the FWHM of the particular broadening mechanisms (see section 4.1.2) is not available in the literature.

It can be seen that the population densities of the excited indium and InBr states increase with increasing cold spot temperature whereas those of the excited argon states decrease. The rate of electron impact excitation processes in a discharge is determined by the ground state density of the species, the electron density and the rate coefficient according to equation (3.20). Therefore, the increasing InBr and In ground state density and the increasing electron density with increasing T_{CS} (see figure 7.1 and 7.3 respectively) result in an increasing excitation rate of electronic indium and InBr states. However, the population density of the argon $1s_2$ state decreases despite the increasing value of n_e (the ground

state density of argon is constant). This converse behaviour can be explained by the steep dependence of the excitation rate on the electron temperature.

In figure 7.5 the rate coefficients for electron impact excitation out of the ground state into the $6^2S_{1/2}$ state of indium and into the $1s_2$ state of argon are shown. They have been calculated with the cross sections from [SN74] and [YCA05] after equation (3.22) assuming a Maxwellian EEDF. The obtained rate coefficient for excitation of the argon $1s_2$ state is much lower than the one for the indium $6^2S_{1/2}$ state. Furthermore, it decreases much more rapidly for decreasing T_e -values which means the excitation rate decreases much stronger. The rate coefficients for electron impact excitation of the other excited argon $1s$ and $2p$ states are also much lower than those for indium or InBr. This can be explained by the higher excitation energy of the argon $1s$ and $2p$ states ($11.5 \leq E_{exc}^{Ar} \leq 13.5$ eV [San05]) compared to the one of the first excited indium and InBr states ($3.0 \leq E_{exc}^{In, InBr} \leq 4.0$ eV [GGV90, MYSR04]). Therefore, the decreasing electron temperature at increasing T_{CS} has a much larger impact on the excitation rate of argon states than on the one of indium or InBr states which results in a decrease of the population densities of all $1s$ and $2p$ states of argon.

To demonstrate the impact of Θ_{line} on the determined population densities of indium, the uncorrected densities are also shown in figure 7.4 (open symbols). It

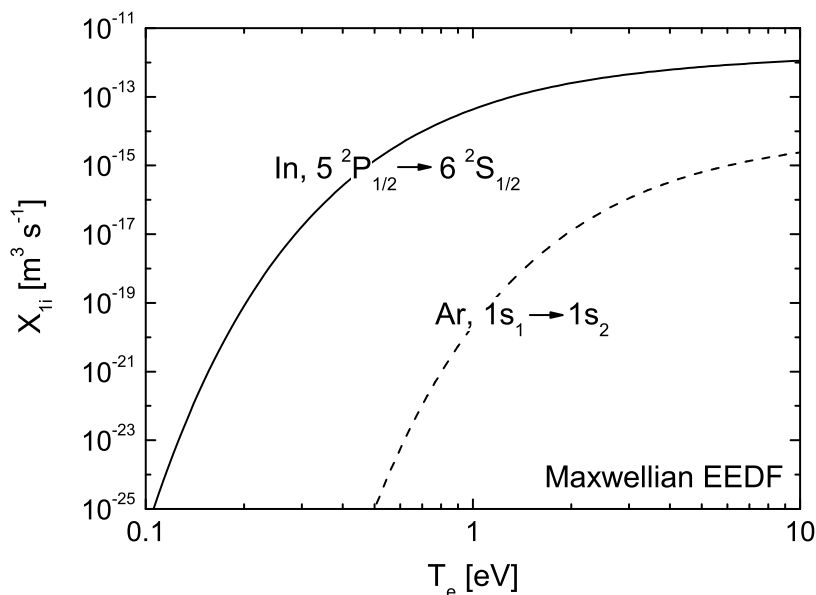


Figure 7.5: Rate coefficients for electron impact excitation out of the ground state into the $6^2S_{1/2}$ state of indium and into the $1s_2$ state of argon. They are obtained according to equation (3.22) assuming a Maxwellian EEDF.

can be seen, that the obtained correction is low at low cold spot temperatures where Θ_{line} is almost unity due to the low optical depth. However, at high T_{CS} the density of both components of the indium ground state and therefore the optical depth of the 410.2 and 451.1 nm lines which originate from the $6\ ^2S_{1/2}$ state is very high. This leads to low values of the line escape factor at $T_{CS} = 231\ ^\circ\text{C}$: $\Theta_{line}(410.2\ \text{nm}) = 0.007$ and $\Theta_{line}(451.1\ \text{nm}) = 0.0107$.

To summarize, the decreasing electron temperature leads to a decrease of the population density of excited argon states with increasing T_{CS} due to their high excitation energy. For indium and InBr, the decreasing excitation rate caused by the decreasing electron temperature is overcompensated by the increasing ground state and electron density. Therefore the population densities of excited electronic indium and InBr states increase with increasing cold spot temperature.

Molecular Temperatures

Fitting the simulated relative intensity of the InBr A,B \rightarrow X emission to the measured one as described in section 4.5.3 yields the relative vibrational and rotational molecular population. The temperatures describing this population if a Boltzmann distribution is assumed (see sections 3.2.3 & 3.2.4) are shown in figure 7.6 dependent on the cold spot temperature.

The rotational temperature of the B state T_{rot}^B coincides with the heating temperature of the discharge vessel T_H at low values of T_{CS} . As the active heating of the vessel also heats the heavy particles in the plasma, T_H can be assigned with the gas temperature. The rotational temperature might be equivalent to the gas temperature of the discharge if the energy difference of the single rotational states is much lower than $k_B T_{gas}$ (see section 3.2.4). For $T_H = T_{gas} = 550\ ^\circ\text{C}$ this relation holds for InBr:

$$\Delta E_{rot}(\text{InBr}) \approx 3 \times 10^{-5}\ \text{eV} \ll k_B T_{gas} \approx 7 \times 10^{-2}\ \text{eV}. \quad (7.2)$$

The rotational temperature of the A state, T_{rot}^A , exceeds T_{rot}^B slightly by 100 K independent of the cold spot temperature. The reason for this behaviour has been described in section 4.5.3.

Increasing the cold spot temperature causes a slight increase of both T_{rot}^A and T_{rot}^B despite the constant heating or gas temperature respectively. This trend can be explained by reabsorption effects of the InBr radiation. According to section 4.5.3, T_{rot}^B is adjusted at the intense $\Delta v = +1$ -sequence of the B – X transition.

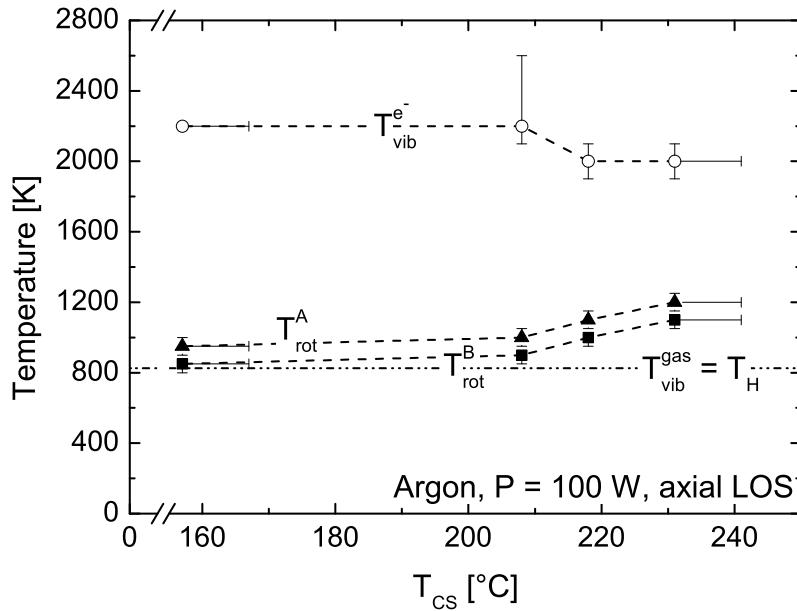


Figure 7.6: Temperatures describing the relative population of the rovibronic states of InBr according to section 4.5 at varying cold spot temperature. They are obtained by fitting the relative intensity of the simulated to the measured spectra.

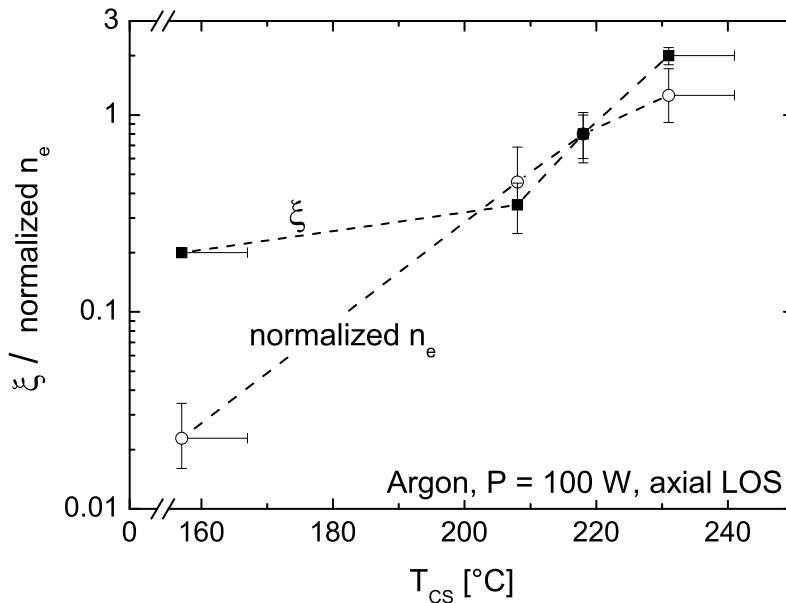


Figure 7.7: Comparison of the weighting factor ξ of the fraction of the vibrational population characterized by T_{vib}^{e-} and the relative trend of the electron density obtained from the extended corona model of indium at varying T_{CS} (see figure 7.3). The values of n_e are normalized to $\xi(T_{CS} = 218^\circ C) = 0.8$.

The occurrence of reabsorption effects results in a lowering of the emitted intensity especially at very intense transitions, as their optical depth is larger. Therefore the intensity reduction is more pronounced in the peak of the sequence which causes an apparently broadening of the whole sequence in the measured emission spectrum. This in turn requires a higher value of T_{rot}^B in the simulation for a good match. The same argumentation is valid for the particular sequences of the A – X transition where T_{rot}^A is adjusted. Hence, the higher value of the rotational temperature at high T_{CS} is caused by the increasing optical depth of the InBr emission due to the high ground state density.

Two population processes are included in the simulation for the vibrational molecular population (see section 4.5.3): inelastic heavy particle collisions characterized by T_{vib}^{gas} and electron impact excitation characterized by T_{vib}^{e-} (see section 4.5). In the simulation T_{vib}^{gas} is set equal to the heating temperature whereas T_{vib}^{e-} and the weighting factor ξ are varied to match the measured spectrum. For increasing cold spot temperature the value of T_{vib}^{e-} decreases slightly as shown in figure 7.6 whereas ξ shows a strong increase (see figure 7.7). The trend of the weighting factor can be explained by the increase of the electron density with increasing T_{CS} (as shown in figure 7.3) making electron impact excitation of the particular vibrational states more important.

According to equation 3.20 the excitation rate is directly proportional to the electron density i. e. the relative increase of ξ should be the same than the one of n_e . In figure 7.7 also the relative trend of the electron density (normalized to the value of ξ at $T_{CS} = 218\text{ °C}$) with increasing T_{CS} is plotted. The relative trends of n_e and ξ agree very well (except for the value at $T_{CS} = 157\text{ °C}$) which reinforces the assignment of the vibrational population characterized by T_{vib}^{e-} to electron impact excitation processes. For $T_{CS} = 157\text{ °C}$, the weighting factor has to be very small ($\xi = 0.2$) to achieve a good match of simulation and measurement i. e. the vibrational population is dominantly caused by inelastic heavy particle collisions. However, due to the low value of ξ the influence of T_{vib}^{e-} on the population is very low which results in a very large error of T_{vib}^{e-} . It is also possible to achieve a good match at $T_{CS} = 157\text{ °C}$ by arbitrarily reducing the value of ξ and increasing the value of T_{vib}^{e-} correspondingly which makes the determination of error bars difficult. Hence, the value of ξ at $T_{CS} = 157\text{ °C}$ is chosen to be as high as possible resulting in the lowest possible value of T_{vib}^{e-} as only this results in non-arbitrary values. This approach can explain the deviation of ξ and the normalized value of n_e at $T_{CS} = 157\text{ °C}$.

Radial Discharge Emission and Efficiency

Figure 7.8(a) shows the power Φ_{ik} emitted by the InBr band and the indium lines at 410.2 and 451.1 nm with varying cold spot temperature T_{CS} . As the radial emission is relevant for lighting purposes, the measurements are carried out at the radial LOS (see section 5.2). As described above, increasing T_{CS} results in an increasing population density of excited InBr and indium states which in turn causes the increase of Φ_{ik} both for the InBr band and the indium emission. For indium (InBr), the radiated power peaks at 208 °C (218 °C) and decreases as T_{CS} is increased further. This can be explained by the high optical depth of indium and InBr radiation at high cold spot temperature due to the high ground state density (see figure 7.1 and 7.4). A high optical depth leads to strong reabsorption effects and therefore to radiation trapping.

Figure 7.8(b) shows the corresponding efficiency of the indium and InBr radiation which is defined after equation (4.4). The relative trend of the efficiency follows the dependence of Φ_{ik} on the cold spot temperature as the RF-power is kept constant. If the emission from the indium lines and the InBr band is added up, an efficiency of $\eta_{InBr,In}^{Ar,100W} = 10.0 \pm 2.0\%$ can be reached.

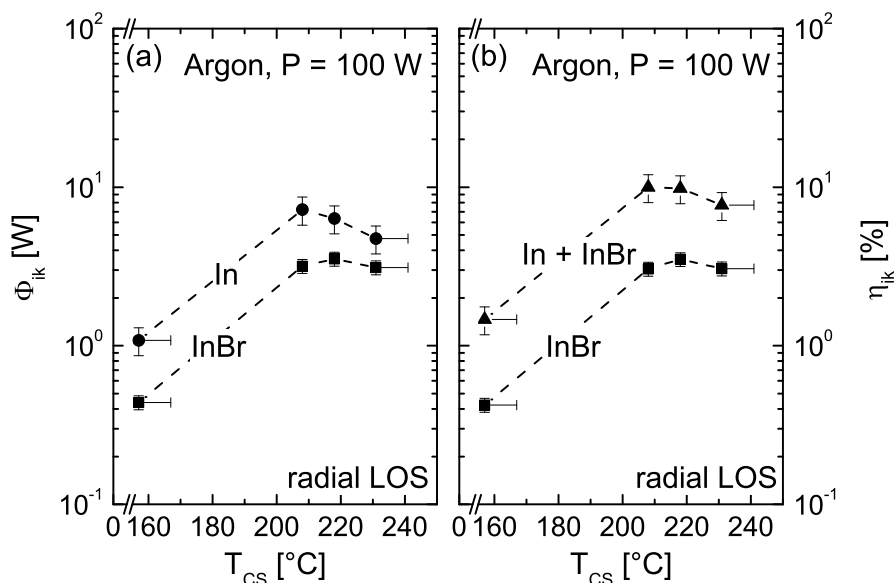


Figure 7.8: Part (a): power radiated by InBr (350 – 400 nm) and by indium (at 410.2 and 451.1 nm) with varying T_{CS} . Part (b): efficiency of the InBr band radiation and of both the InBr and the indium emission with varying T_{CS} .

Summary

The most evident impact of an increasing cold spot temperature and therefore the InBr density on the InBr/argon discharge is the change of the plasma emission colour from argon dominated pink to indium dominated blue (the near UV emission of InBr is not visible). The increasing InBr density leads to a gradually substitution of the light-weight argon ions which have a high ionization energy by heavy-weight InBr/indium ions which have a comparatively low ionization energy. This causes a decrease of the electron temperature from 0.8 eV at $T_{CS} = 160$ °C to 0.4 eV at $T_{CS} = 230$ °C and an increase of the electron density from $2.0 \times 10^{18} \text{ m}^{-3}$ to $1.1 \times 10^{20} \text{ m}^{-3}$. The population densities of the excited InBr and indium states which determine the amount of radiation emitted by the discharge increase strongly with increasing cold spot temperature despite the decreasing electron temperature due to the increasing corresponding ground state density and the increasing electron density. In converse, the population density of excited argon states decreases which can be explained by the much stronger dependence of the excitation rate of argon on the decreasing electron temperature due to the higher excitation energy compared to indium and InBr.

The relevant population processes of InBr have been identified by fitting the simulated relative emission to the measured spectra. It turned out that the vibrational levels of the ground state are populated both via inelastic heavy particle and electron collisions in the discharge. The share of the population by electrons changes according to the change of the electron density. The population of vibrational states in the electronic A or B state is determined by electron impact excitation out of the electronic ground state whereas the rotational population is determined by inelastic heavy particle collisions. As the measured spectrum is reproduced well by the simulation, the contribution of additional population processes to the rovibrational states of the A and B state can be regarded negligible in the investigated discharge. At high cold spot temperatures, the relative intensity of the InBr emission is distorted slightly due to reabsorption effects. The opacity of the InBr radiation could be reduced if the emission would be distributed in a broader wavelength range. However, the observed variation of the molecular temperatures does not lead to a considerable broader distribution due to the small molecular constants of InBr.

If the discharge emission is dominated by InBr and indium, the radiated power is distributed almost equally between the InBr band, the indium line at 410.2 nm and the one at 451.1 nm each having a share just under one third. Indium

emission lines located between 270 and 330 nm also contribute to the emission by a share of roughly 10%. For lighting applications the complete discharge emission can be utilized but the efficiency considerations focus on the InBr band and the two intense indium lines. An increase of the cold spot temperature results in a increasing emission due to the increasing population density of the excited InBr and indium states. At high T_{CS} -values the intensity of the emission decreases again as the indium lines and the InBr band become optically thick. The maximum efficiency of $\eta_{InBr,In}^{Ar,100W} = 10.0 \pm 2.0\%$ is achieved within a rather broad cold spot temperature range between 210 and 220 °C.

7.2 Variation of the RF-Power

In order to investigate the influence of the RF-power on the discharge characteristics at varying cold spot temperature, measurements have been carried out at $P = 40$ W using the same discharge vessel as for the studies of the previous section. A systematic investigation at a lower power was not possible, as the plasma constricted below 40 W and did not fill out the whole vessel volume anymore which is a prerequisite for a proper function of the cold spot setup.

The investigations at 40 W proved that the relative trends at varying T_{CS} for the population densities of the ground and excited states, T_e , n_e and of the molecular temperatures are the same as those for the measurements at 100 W presented in the previous section. Therefore the general discharge characteristics with varying cold spot temperature which is basically caused by the transition from an argon plasma to an InBr/In dominated discharge as described in section 7.1 is independent of the RF-power. This is shown exemplarily for the radially radiated power of the InBr and In emission in figure 7.9(a): The relative trend of the radiated power is the same for 100 W (filled symbols) and for 40 W RF-power (open symbols) and the maximum emission is located at the same cold spot temperature ($T_{CS} \approx 210$ °C for indium and $T_{CS} \approx 220$ °C for InBr). For 40 W RF-power the discharge stability at high cold spot temperature is worse than at 100 W. Therefore a measurement above $T_{CS} \approx 225$ °C is not possible.

However, the absolute values of the discharge parameters obtained at 40 W and at 100 W RF-power differ. As shown in figure 7.9(a) again exemplarily, the absolute values of the radiated power of InBr and indium at 40 W RF-power are lower than the ones obtained at 100 W. For example, the radiated power by the two indium lines at a cold spot temperature of 218 °C is $\Phi_{In}^{Ar,100W} \approx 6.4$ W

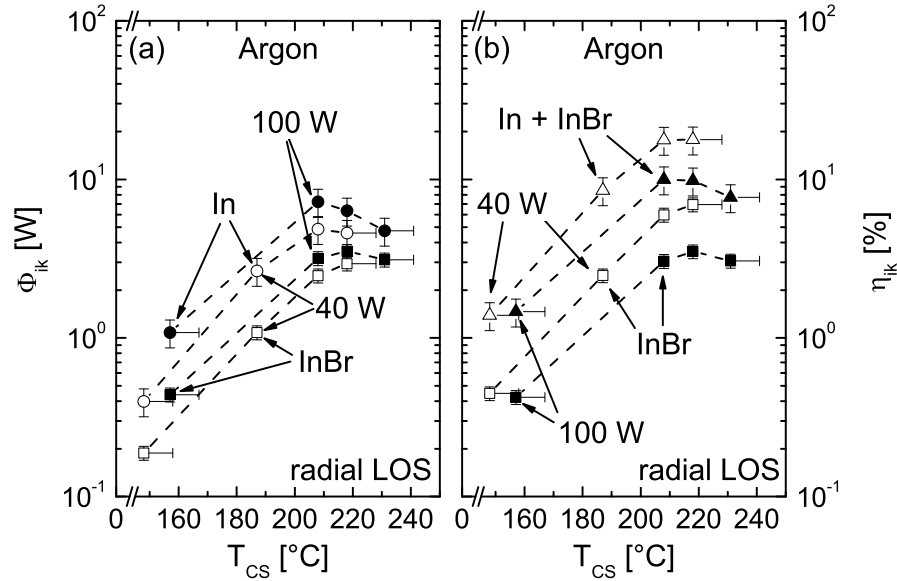


Figure 7.9: Part (a): power radiated by InBr (350 – 400 nm) and by indium (at 410.2 & 451.1 nm) with varying T_{CS} . Part (b): efficiency of the InBr band radiation and of both the InBr and the indium emission with varying T_{CS} . In both parts, the filled symbols represent the values obtained at 100 W RF-power whereas the open symbols represent the values at 40 W.

whereas $\Phi_{In}^{Ar,40W} \approx 4.6$ W, i. e. roughly 72% of the emission at 100 W are achieved at 40 W but only 40% of the RF-power is used. As the situation is similar for the InBr emission the maximum efficiency of the discharge at 40 W RF-power $\eta_{InBr,In}^{Ar,40W}(T_{CS} \approx 218 \text{ } ^\circ\text{C}) = 17.8 \pm 3.6\%$ is about a factor of 2 higher than the one achieved at 100 W (see figure 7.9(b)).

To explain the better efficiency at lower RF-power, the population densities of the excited states have to be considered as they determine the emitted radiation and therefore the efficiency. The following considerations are carried out exemplarily for $T_{CS} \approx 218 \text{ } ^\circ\text{C}$ where the maximum efficiency is achieved. In a qualitative way, the explanations are also valid for other cold spot temperatures. The population densities of the A and B state of InBr and of the $6 \text{ } ^2\text{S}_{1/2}$ state of indium (from which the desired emission originates) obtained from OES measurements at the axial line of sight at 40 and 100 W are shown in table 7.2. For the indium population densities, reabsorption effects have been considered. The measured population densities of both the excited InBr and indium states are higher at 40 RF-power whereas the emission is lower compared 100 W as shown in figure 7.9(a). It should be noted that the densities are measured at the axial line of sight whereas the emission shown in figure 7.9(a) is measured at the radial

LOS. As the spectroscopic measurement only provides a line-of-sight averaged value (see section 4.1), a consideration of the radial population density profiles may explain the lower emission at 40 W despite the higher population density.

Table 7.2: Population densities of the A and B state of InBr and of the $6^2S_{1/2}$ state of indium measured via OES at the axial LOS at $T_{CS} \approx 218^\circ\text{C}$.

State	Population density [m^{-3}]	
	at 40 W	at 100 W
InBr, A	9.7×10^{16}	6.1×10^{16}
InBr, B	1.9×10^{17}	1.2×10^{17}
Indium, $6^2S_{1/2}$	5.9×10^{15}	3.1×10^{15}

Radial Profiles of the Population Densities of Excited States

The radial profiles of the population densities of the A state of InBr (the B state has the same profile) and of the $6^2S_{1/2}$ state of indium which are shown in figure 7.10 have been obtained by OES measurements at a stepwise radially shifted axial line of sight. Again, reabsorption effects are only considered for the indium population densities. It can be seen that for both excited states, the radial profile is lowest at the central axis of the cylinder and the population density increases towards the discharge vessel wall. A measurement of the densities closer to the wall was not possible due to a partly blocking of the line of sight by the thermal insulation of the experimental setup (see section 5). At 100 W RF-power a correction of reabsorption effects in the determination of the indium population density was not possible, as the white light absorption measurements of the ground state could not be evaluated due to distortions in the signal. Therefore, no value of the population density of the $6^2S_{1/2}$ state is shown.

For higher RF-power, the population density at the central axis is lower but increases more rapidly to the wall. To explain the relative trends and the differences at low and high RF-power, the relevant population processes and their dependencies on the plasma parameters have to be considered. As described in section 3.2.1, the main excitation process is electron impact excitation out of the ground state (or a lower metastable state). According to equation (3.20) the excitation rate is determined by the density of the ground (or metastable) state of the species, the electron temperature and the electron density which means their radial profiles have to be considered.

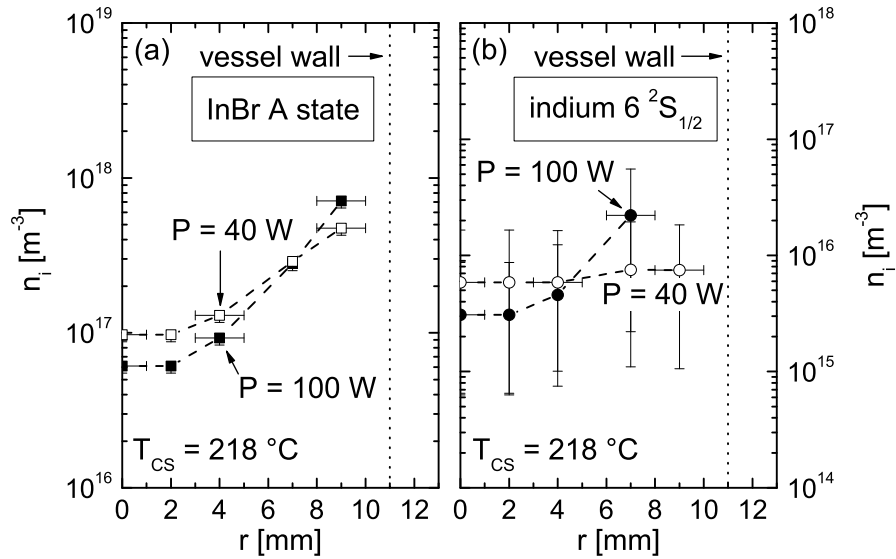


Figure 7.10: Radial profiles of the population densities of (a) the A state of InBr and (b) the $6^2S_{1/2}$ state of indium obtained via OES. The filled symbols represent the values obtained at 100 W RF-power whereas the open symbols represent the values at 40 W in both parts of the figure.

Radial Profiles of the Electron Temperature and Density

The radial profiles of T_e and n_e are obtained from spectroscopic measurements of the indium population densities and the extended corona model of indium according to section 4.3. As shown in figure 7.11(a), the electron temperature shows a slight decrease from the central axis towards the discharge vessel wall. As described in section 3.2.6 the value of the electron temperature is determined by the ionization balance. A qualitative explanation of the radial T_e -trend is difficult as this would require a spatial evaluation of the ionization balance which is not possible. However, close to the wall the influence of the sheath formed due to ambipolar diffusion can have a considerable influence on T_e [SCC00], which could explain the decrease of the electron temperature towards the wall qualitatively. The absolute values of T_e for 40 and 100 W coincide within the error bars as the ionization balance is independent of the RF-power.

In converse to the T_e -profile, the radial profiles of the electron density obtained at high and low power have a different shape as shown in figure 7.11(b). The values of n_e at 100 W RF-power increase towards the vessel wall which indicates a hollow profile. Such a profile is typical for cylindrical discharges at high pressure ($p \geq 20$ mbar) [RTMS96], but atypical for low pressure where the n_e profile is usually more bell-shaped (maximum in the centre, minimum at the wall). This

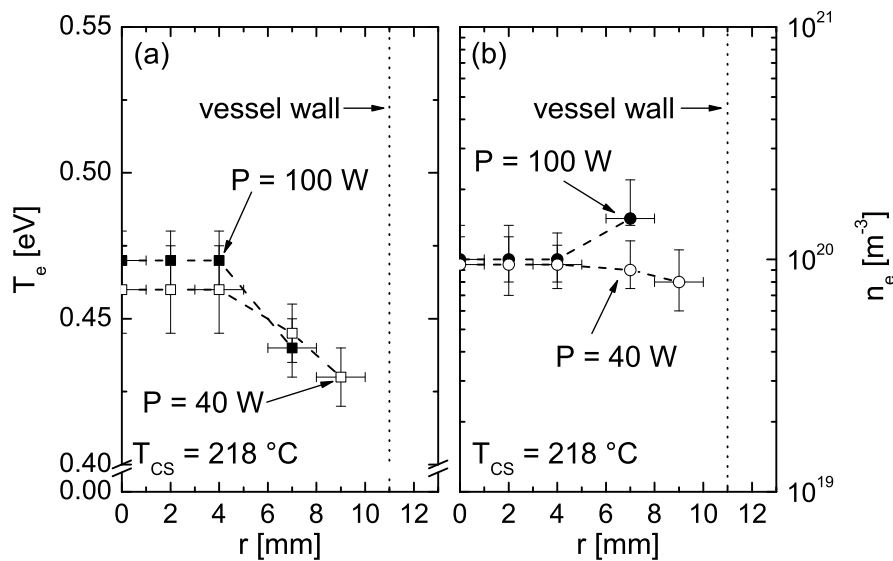


Figure 7.11: Radial profile of (a) the electron temperature and (b) the electron density obtained from the extended corona model of indium. The filled symbols represent the values obtained at 100 W RF-power whereas the open symbols represent the values at 40 W in both parts of the figure.

bell-shaped profile is obtained at 40 W RF-power where the electron density is highest at the central axis and shows a slight decrease towards the vessel wall. Such a profile is developed as electrons are primarily created in the discharge volume due to ionization processes and lost at the wall due to ambipolar diffusion [LL94, NGB00]. The reason for the differing radial electron density distribution at 40 and 100 W RF-power cannot be figured out as this would require a quantitative spatial evaluation of the power balance which is not possible.

Radial Profiles of the $5^2P_{1/2}$ & $5^2P_{3/2}$ States of Indium

The radial profile of the population density of the indium ground ($5^2P_{1/2}$) and metastable ($5^2P_{3/2}$) state obtained at 40 and 100 W RF-power measured via white light absorption spectroscopy is shown in figure 7.12. Saturation effects are considered according to section 4.3.

The profiles of the ground state density show a minimum at the central axis and an increase towards the wall which is more pronounced at high RF-power. This is a typical distribution for a species with low ionization energy in a low pressure rare gas discharge [NGB00, GGK⁺03, DRS05]. In general, the low density at the centre is caused by the large ionization rate due to the typically higher value of n_e at the central axis compared to the electron density close to the wall.

Furthermore, the recombination of ions at the wall and the diffusion of the former ions back into the discharge lead to an increase of the ground state density close to the wall.

For 40 W RF-power, a slight bell-shaped electron density profile is obtained as shown in figure 7.11. Also the electron temperature profile shows a slight decrease toward the vessel wall. Both profiles lead to a smaller ionization rate towards the wall which explains the measured radial profile of the indium ground state density.

For 100 W RF-power, only the radial T_e profile shows a decrease towards the vessel wall whereas the n_e density is minimal at the central axis and increases towards the wall. These effects have an opposite influence on the ionization rate. The consideration of their absolute impact on the ionization rate shows that both effects nearly cancel each other. Hence, the radial distribution of the ground state cannot be explained by a different ionization rate of the indium atom at 100 W. However, as atomic indium is generated by electron impact dissociation of InBr, the radial profile of the InBr ground state density also determines the distribution of the indium ground state density. Therefore, the different radial profiles of the indium ground state density obtained at 40 and at 100 W could be caused by a different radial distribution of the InBr ground state density.

Considering the metastable $5^2P_{3/2}$ state, its population is determined by elec-

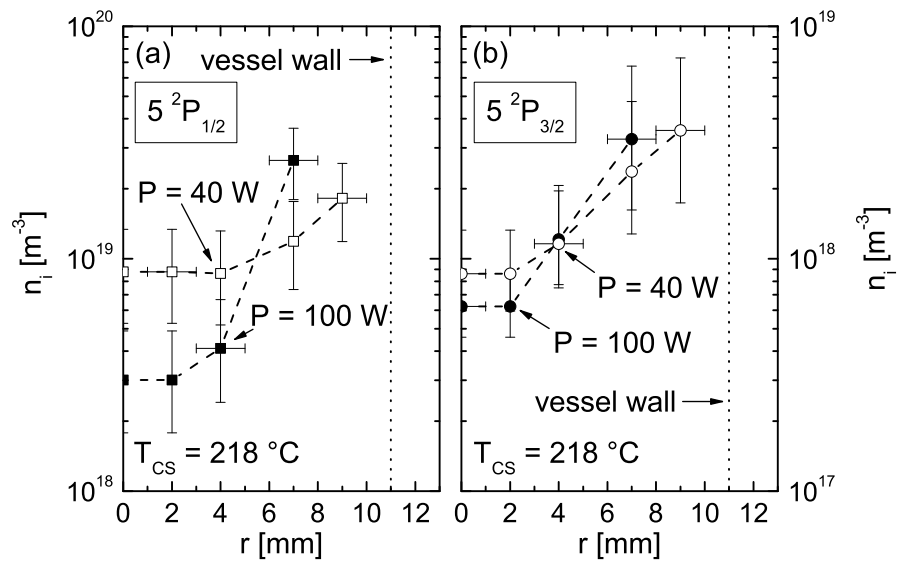


Figure 7.12: Radial profile of (a) the ground state ($5^2P_{1/2}$) density and (b) the population density of the metastable $5^2P_{3/2}$ state of indium at 40 and 100 W RF-power. The filled symbols represent the values obtained at 100 W RF-power whereas the open symbols represent the values at 40 W in both parts of the figure.

tron impact excitation out of the ground state and by radiative decay from excited states. Therefore, the radial profile of the metastable state density is determined by the profiles of the indium ground state, of T_e and n_e (due to the electron impact excitation process) and of the profile of the excited indium states (due to the radiative decay).

The electron temperature and density profiles at 40 W show only a slight decrease towards the wall whereas the profiles of the ground and excited states show a strong increase towards the wall. Therefore, the radial profile of the population density of the metastable $5^2P_{3/2}$ state reflects the profile of the indium ground state and of the excited indium states.

The profile of the metastable $5^2P_{3/2}$ state obtained at 100 W coincides with the profile obtained at 40 W within the error bars despite the different ground state and n_e & T_e profiles. This can be explained by a large influence of radiative decay from excited indium states on the population of the $5^2P_{3/2}$ state as the radial distribution of excited states is very similar for 40 and 100 W (see figure 7.10).

Influence of the Power-dependent Radial Profiles on the Efficiency

For high and low RF-power, the relative radial distribution of the population density of both the excited InBr and indium states are maximal close to the discharge vessel wall and minimal at the central axis of the cylindrical vessel. If the RF-power is decreased, the population density of the excited states decreases at the wall whereas the one at the central axis increases. This trend can be explained by the power-dependent radial profiles of those parameters that determine the population of these states by electron impact excitation: the ground (or metastable) state density, the electron temperature and the electron density.

The T_e -profile is independent of the RF-power whereas the radial profile of n_e shows a decrease of the values close to the wall but a constant n_e at the central axis at decreasing power. The profile of the indium ground (or metastable) state shows a decreasing density close to the wall and an increasing density at the centre at decreasing power. Therefore, the changing profile of the population density of the excited indium states is caused by the changing profile of the indium ground (or metastable) state density and the increase of n_e close to the wall.

In summary, a higher RF-power leads to an increase of the density of excited indium and InBr states close to the discharge vessel wall, i. e. the majority of radiation is generated there. But also the ground (and metastable) state density

of indium increases close to the wall which results in a higher optical depth at high RF-power. The correction factors Θ_{line} obtained for the different radial positions of the axial line of sight are shown exemplarily for the indium emission line at 410.2 nm in table 7.3 for low and high RF-power. At $r = 7$ mm the optical depth is roughly a factor of 2 higher at 100 W RF-power than at 40 W which results in a Θ_{line} that is a factor of 3 lower, i. e. reabsorption effects in the indium line are stronger at 100 W by a factor of 3 compared to 40 W. Hence, the higher optical depth near the discharge vessel wall (where the majority of excited atoms and molecules are located) limits the increase of the radiation output with increasing power as the influence of reabsorption processes increase. This results in a smaller efficiency of the discharge at higher RF-power which makes an operation at low RF-power advantageous for lighting applications.

Table 7.3: Θ_{line} of the indium 410.2 nm line at $T_{CS} \approx 218^\circ C$ for different radial positions.

Radial position [mm]		0	2	4	7	9
Θ_{line}	at 40 W	0.03	0.03	0.03	0.03	0.02
	at 100 W	0.08	0.08	0.06	0.01	–

Summary

A reduction of the RF-power from 100 to 40 W results in an increase of the maximum efficiency by almost a factor of 2 from $\eta_{InBr,In}^{Ar,100W} = 10.0 \pm 2.0\%$ to $\eta_{InBr,In}^{Ar,40W} = 17.8 \pm 3.6\%$. This behaviour is caused by the power-dependent radial profiles of the population densities of the ground and the excited states of InBr and indium. At high power, the impact of reabsorption effects is larger especially close to the discharge vessel wall where the majority of InBr and indium radiation is generated. Therefore, a higher RF-power increases the radiated power only slightly which results in a better efficiency at lower RF-power.

7.3 Variation of the Background Gas

As described in section 2.2, the choice of the background gas type and its pressure influences the values of plasma parameters like the electron temperature or the gas temperature. In general, all rare gases could be used as background gas for a low pressure discharge. However, the application of helium in a plasma for lighting

purposes is not reasonable as helium permeates through glass and metal with a high rate. This leads to a constant decrease of the helium amount in the lamp vessel which would strongly limit the lamp lifetime [Mos09]. Furthermore, the large-scale use of xenon in lamps for general lighting is not reasonable due to the very high price of xenon [Mos09]. Therefore, only the rare gases neon, argon and krypton have been investigated as background gases. To allow for a determination of the sole influence of the rare gas type on the discharge parameters and efficiency, the filling pressure of the discharge vessels had been kept constant at 1 mbar.

As shown in the previous section for argon as background gas, an operation at low RF-power increases the efficiency of the InBr and indium light output. To investigate the power dependence of the discharge efficiency for the background gases neon and krypton, measurements at 100 W and at the lowest possible power were carried out. As already mentioned, the threshold value for argon - which is defined by the demand that the plasma has to fill out the whole vessel volume - is located at 40 W. The same value is valid for krypton, but for neon the threshold is located at 70 W. This high value is caused by instabilities of the discharge which lead to oscillations of the plasma volume and a flickering of the emission especially at low cold spot temperature.

The measurements with varying cold spot temperature carried out at high and low RF-power always showed the same relative trends for the population densities of the ground and excited states, T_e , n_e and of the molecular temperatures as for argon independently of the background gas type. As described in section 7.1, these trends can be explained by the transition of the discharge from a rare gas dominated plasma to an InBr/In dominated discharge. Furthermore, the better efficiency at low RF-power (see section 7.2) also occurred with neon and krypton. As a good efficiency is desirable for lighting applications, the following comparisons of the results obtained using different background gases is restricted to low-power operation.

Electron Temperature and Density

The transition from the rare gas dominated discharge to an InBr/indium dominated plasma is shown exemplarily in figure 7.13 for the electron temperature and density obtained from the extended corona model of indium (see section 4.3). For krypton, an evaluation of the extended corona model was not possible below $T_{CS} \approx 170$ °C as the absorption signals of the ground and metastable indium states are below the detection threshold.

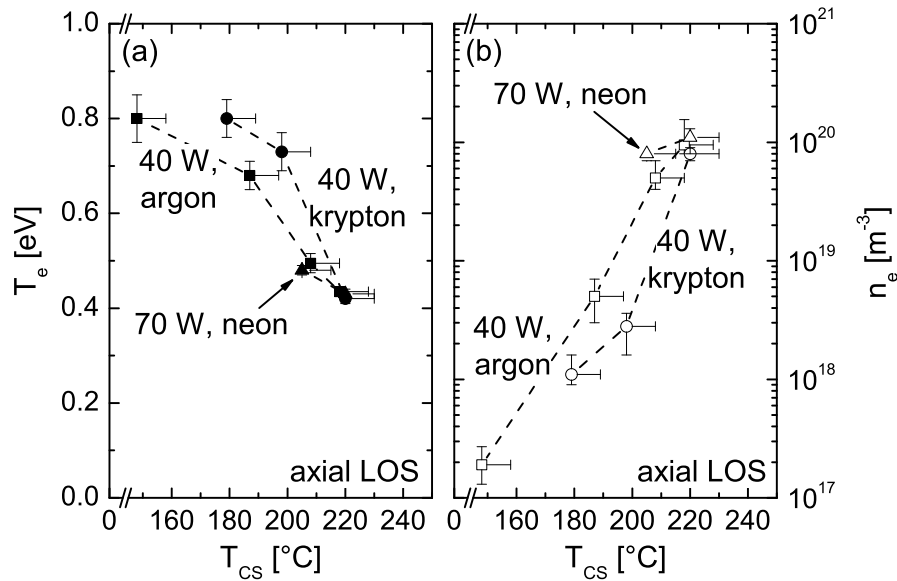


Figure 7.13: Part (a) electron temperature and part (b) electron density obtained from the extended corona model of indium at varying cold spot temperature for different background gases.

The absolute values of T_e obtained for argon and krypton at low cold spot temperature differ from each other. According to the section 3.2.6 the electron temperature of an argon discharge should be higher than the one of a krypton plasma (the ionization energy of krypton is smaller and the ion mass larger) but the measured T_e -values show the contrary behaviour. However, also indium and InBr have an impact on the ionization balance despite the low cold spot temperature. Their influence can be described qualitatively by considering the corresponding ground state density in the discharge. The indium ground state density determined by white light absorption spectroscopy is shown in figure 7.14 (saturation effects have been considered). It can be seen that the values obtained at low cold spot temperature for the InBr/krypton discharge are much lower than those of the InBr/argon plasma. Therefore also the impact of indium on the ionization balance is reduced with krypton as background gas. According to section 7.1 a smaller influence of indium results in a higher electron temperature. As the indium densities are measured at the axial line of sight, the different ground state densities could be caused by different radial density profiles for argon and krypton.

Increasing the cold spot temperature results both for argon and krypton in an increased influence of indium and InBr on the ionization balance and a reduction of the influence of the rare gas. As the indium ground state density at high cold

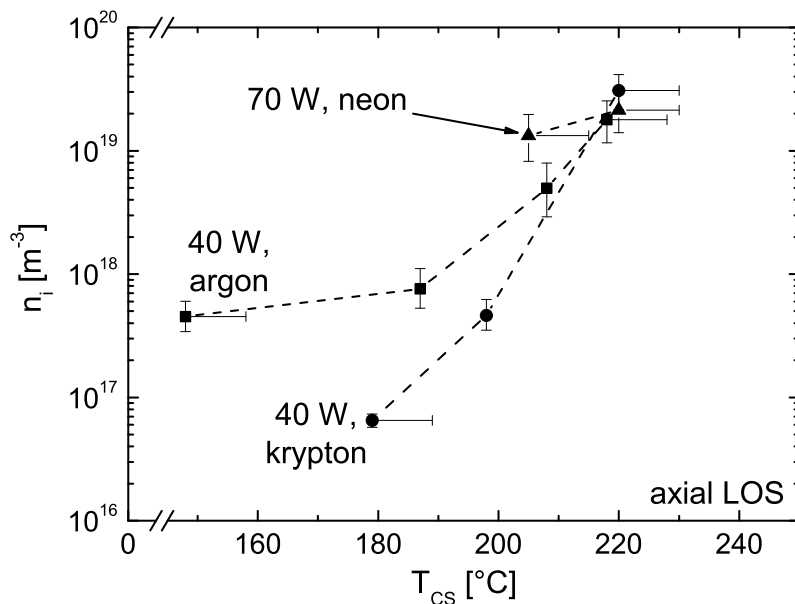


Figure 7.14: Ground state density of indium at varying cold spot temperature for different background gases obtained from white light absorption spectroscopy.

spot temperature is independent on the background gas type, a similar influence of indium on the ionization balance for all background gases can be assumed. Therefore, at high T_{CS} the values of the electron temperature coincide for the background gases neon, argon and krypton.

Also the electron density shows differing values for the InBr/argon and the InBr/krypton discharges at low cold spot temperature as shown in figure 7.13(b). According to section 3.2.7, the value of n_e is determined by the power balance. As described in section 7.1, for InBr/rare gas discharges the power balance of an atomic discharge has to be considered due to the low excitation energies of the rovibrational states. As described in section 7.1 only the quantitative dependencies of the power balance can be considered: a larger ion mass and a smaller electron temperature lead to a larger value of n_e (see section 3.2.7). As the electron density of the InBr/argon discharge (smaller ion mass and smaller electron temperature) exceeds the value of n_e of the InBr/krypton plasma (larger ion mass and larger T_e -value), it must be assumed that the influence of the larger electron temperature exceeds the influence of the ion mass on the power balance.

At high cold spot temperature, where the discharge parameters are primarily determined by indium and InBr, the obtained electron density values are independent on the rare gas type like the values of the electron temperature.

Radial Discharge Emission and Efficiency

Figure 7.15(a) shows the efficiency of the radial InBr emission (between 350 and 400 nm) and figure 7.15(b) shows the one of the added InBr and indium emission (350 to 400 plus 410.2 & 451.1 nm) at varying cold spot temperature using the different background gases. As described previously, the relative trends of the efficiencies are independent on the background gas type. The maximal efficiency is reached at a cold spot temperature of $T_{CS} \approx 220$ °C for each background gas. Also the obtained absolute values coincide within the error bars for all background gases: $\eta_{InBr,In}^{Ne,70W} = 15.6 \pm 3.1\%$, $\eta_{InBr,In}^{Ar,40W} = 17.8 \pm 3.6\%$ and $\eta_{InBr,In}^{Kr,40W} = 13.5 \pm 2.7\%$.

A gas type dependence of the efficiency is not obtained for the InBr/argon and InBr/neon discharges. The slightly lower efficiency of the InBr/krypton plasma is primarily caused by the lower efficiency of the InBr radiation as shown in figure 7.15(a) (the efficiency of the indium radiation is comparable at high cold spot temperatures to the one with the background gases argon or neon). A reason for the lower InBr radiation could be a gas-type dependent radial profile of the InBr ground state density. If the density close to the vessel wall is larger with krypton, the InBr emission is lowered due to radiation trapping (see section 7.2).

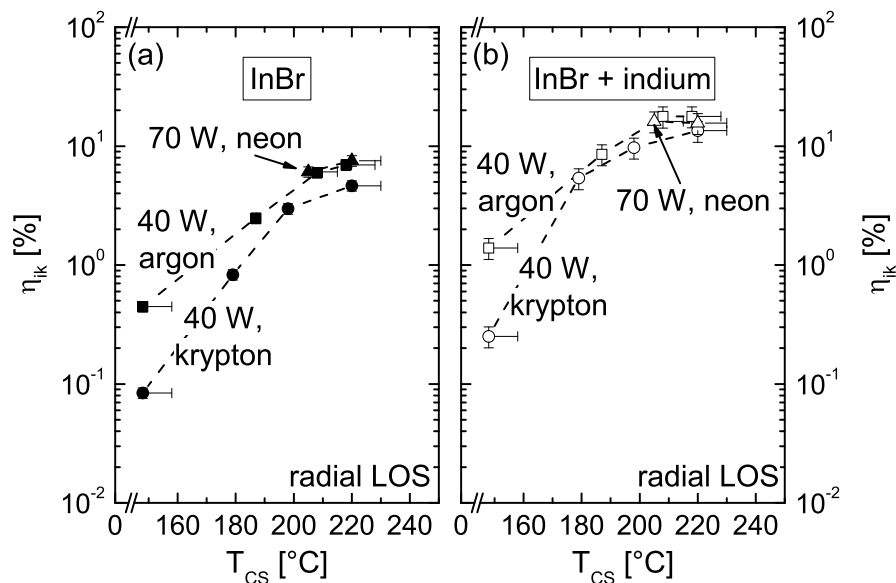


Figure 7.15: Efficiency (a) of the InBr radiation between 350 and 400 nm and (b) of the added InBr and indium emission at varying cold spot temperature for different background gases.

Summary

The higher efficiency of the InBr and indium radiation at lower RF-power occurs for all investigated background gases. Therefore, the impact of the background gas type on the discharge characteristics has been investigated using the particular lowest possible RF-power: 40 W for argon and krypton and 70 W for neon. If the cold spot temperature is low the discharge is dominantly influenced by the rare gas and the electron temperature and density values depend on the utilized background gas type. At high T_{CS} -values, the discharge is completely dominated by InBr and indium, i. e. also the plasma parameters are independent on the rare gas type. The maximum efficiency of the InBr and indium radiation is achieved in the InBr/indium dominated regime and the values obtained for the different background gases coincide within the error bars. The highest efficiency of $\eta_{InBr,In}^{Ar,40W} = 17.8 \pm 3.6\%$ is reached using argon as background gas at 40 W RF-power between a cold spot temperature of 210 to 220 °C.

The utilization of neon as light-weight background gas, which might be favoured for the lamp application to reach the optimum cold spot temperature without external heating, allows for a similar efficiency as argon. However, the instability issues of InBr/neon discharges at low cold spot temperatures have to be solved (e. g. by applying mixtures of argon and neon) as low T_{CS} -values occur in the initial starting phase of a lamp.

8 Investigation of InCl as Radiating Species

8.1 Variation of the Cold Spot Temperature

The discharge characteristics and the efficiency of the generation of molecular near UV and indium radiation of InCl/rare gas plasmas at varying cold spot temperature have been investigated using a discharge vessel which contained 1.5 mg InCl and 1 mbar argon. A RF-power of 100 W had been used to allow for a comparison between the properties of the InCl discharges and those of the InBr discharges described in section 7.1.

The fundamental transition of the plasma from low cold spot temperatures where argon dominates the discharge to high values of T_{CS} where the indium halide molecule and atomic indium dominate the plasma is also evident for InCl. The plasma emission changes accordingly from argon dominated to indium halide/indium dominated at increasing cold spot temperature. As the basic physical reasons for this transition are the same as described in section 7.1 for InBr, the focus of this section is put on the explanation of the differences between InCl/argon and InBr/argon discharges with varying T_{CS} .

Densities of InCl and Indium

The evaporated InCl amount can be calculated according to the vapour pressure curve but three curves differing about a factor 1.5 to 3 are available in the literature for InCl (see section 2.4). In order to identify the vapour pressure curve with the best agreement to the measured evaporated density white light absorption measurements in gas phase can be carried out (see section 5.3 for InBr). However, for InCl this approach is not possible as the absorption measurements require effective transition probabilities. They are obtained from the simulation of the relative molecular intensity (see section 4.5), but the simulation yields doubtful molecular temperatures for InCl as described in section 4.5.4.

Figure 8.1(a) shows the evaporated density of InCl which is calculated using the different vapour pressure curves. The calculated evaporated amount of InBr in the InBr/argon discharge described in section 7.1 is also plotted. Increasing the cold spot temperature results in an increase of the InCl density, but a comparison of the absolute values to those of InBr cannot be carried out.

The ground state density of indium in the InCl/argon discharge which is obtained from white light absorption measurements at the axial line of sight is shown in figure 8.1(b) together with the one measured in the InBr/argon discharge (see section 7.1). Saturation effects have been considered in the evaluation. In the InCl/argon discharge, a measurement below $T_{CS} \approx 200$ °C could not be performed as the absorption signal is below the detection threshold. For all cold spot temperatures, the values of the indium ground state density are roughly one order of magnitude smaller in the InCl/argon discharge. As indium is primarily generated due to electron impact dissociation processes in the plasma, this behaviour can be explained by a smaller dissociation rate of InCl compared to InBr.

A comparison between the InBr and the InCl ground state density which influences the dissociation rate cannot be carried out as described above. The cross

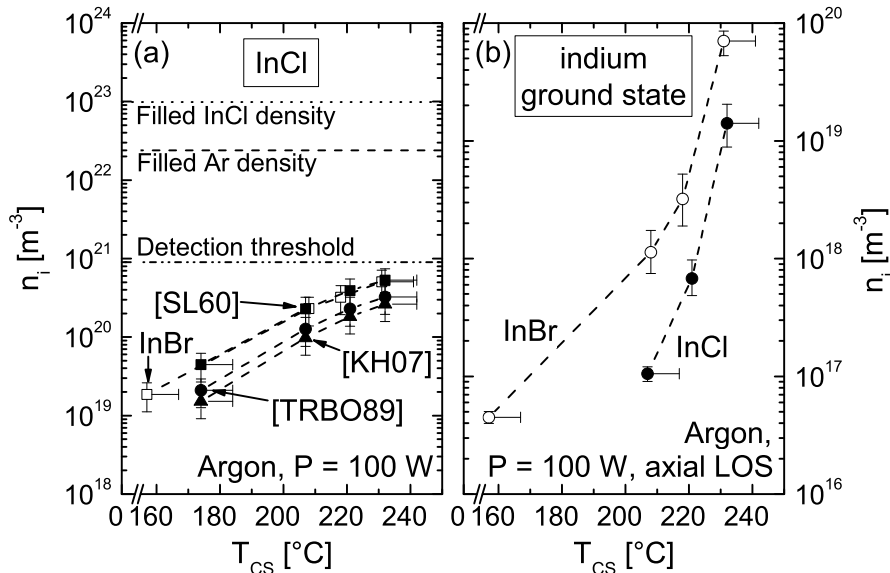


Figure 8.1: Part (a): volume-averaged InCl density calculated from the different vapour pressure curves (see section 2.4) at varying T_{CS} . For comparison the evaporated InBr amount of the investigations of section 7.1, the detection threshold for absorption measurements of InCl and the filled InCl and argon density are shown. Part (b): ground state density of indium measured in the InCl/argon (labelled InCl) and in the InBr/argon discharge (see section 7.1, labelled InBr).

sections for electron impact dissociation of InCl and InBr are both not available in the literature but for a quantitative statement the dissociation energies of the electronic ground state can be considered. The dissociation energy of InCl (4.44 eV, see section 2.4) is larger than the one of InBr (3.99 eV) which results in general in a smaller dissociation rate and therefore a smaller indium density in the InCl/argon discharge.

Electron Temperature and Density

The values of T_e and n_e obtained from the extended corona model of indium for the InCl/argon and the InBr/argon discharge are shown in figure 8.2. In the InCl/argon discharge, the electron temperature is higher than in the InBr/argon plasma except for $T_{CS} \approx 230$ °C where the values coincide. The smaller ground state density of indium and potentially of InCl in the InCl/argon discharge results in a larger influence of argon on the ionization balance. Furthermore, the InCl ion has a smaller mass than the InBr ion, i. e. the ion confinement time is smaller for the InCl ion. As described in section 3.2.6 both effects cause a higher electron temperature. The cross sections for electron impact ionization of InBr and InCl are almost identical as shown in figure 3.1 therefore the influence of InBr and InCl on the ionization balance is the same in this point.

For $T_{CS} \approx 230$ °C, the above considerations are also valid but the values of

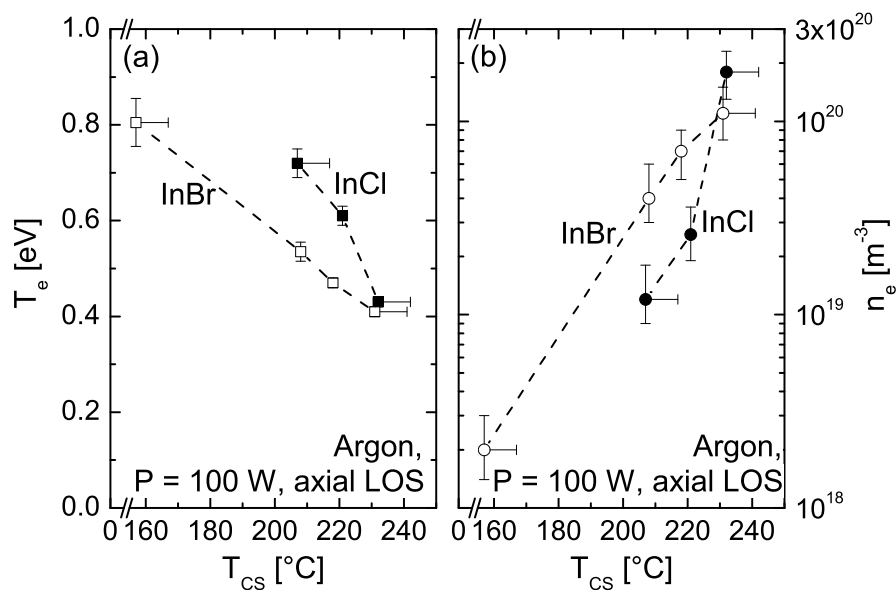


Figure 8.2: Part (a) electron temperature and part (b) electron density obtained from the extended corona model of indium at varying T_{CS} .

T_e are the same for the InCl/argon and the InBr/argon discharge. Therefore the ionization balance is completely dominated by atomic indium at high cold spot temperatures in both discharges whereas the influence of the rare gas and even of the indium halide molecule on the ionization balance is negligible.

In contrast to the higher T_e -values in the InCl/argon discharges, the electron density is lower than in the InBr/argon plasma again except for the value at $T_{CS} \approx 230$ °C. The smaller electron density of the InCl/argon discharge can be explained qualitatively by the impact of the smaller confinement time of the InCl ion (due to the smaller mass) on the power balance and by the higher electron temperature compared to the InBr/argon plasma. As indium dominates the discharge completely at high cold spot temperatures, the n_e -values are the same for the InCl/argon and InBr/argon discharge at $T_{CS} \approx 230$ °C.

Molecular Temperatures

An evaluation of the molecular temperatures has been carried out to compare the relative trends to those of InBr despite the insignificant absolute values (see section 4.5.4). Figure 8.3(a) shows the molecular temperatures obtained from fitting the simulated relative A – X emission spectrum to the measured one.

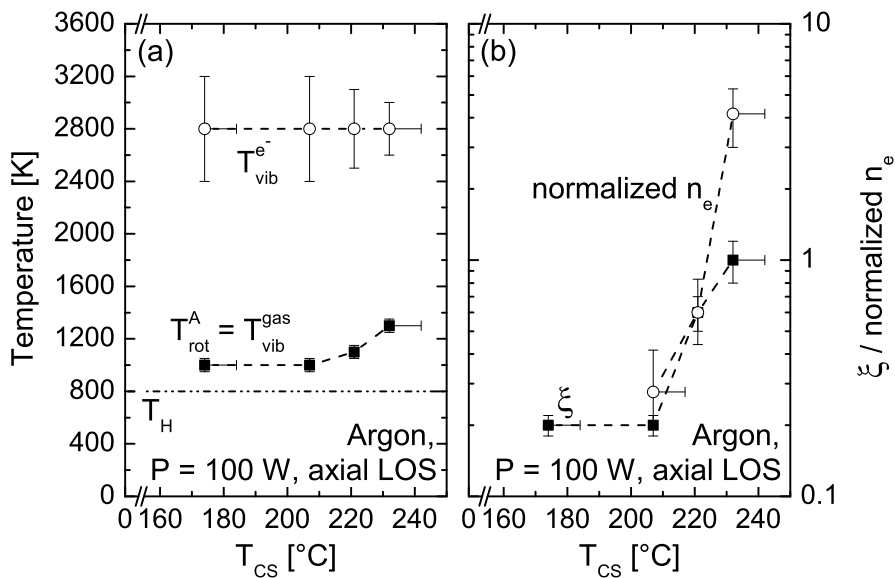


Figure 8.3: Part (a): temperatures describing the relative population of the rovibrational states of the InCl A state according to section 4.5 at varying T_{CS} . Part (b): comparison of the weighting factor ξ and the relative trend of the electron density obtained from the extended corona model of indium. The values of n_e are normalized to $\xi(T_{CS} = 221$ °C) = 0.6.

Similar to the rotational temperatures of InBr, the value of T_{rot}^A increases with increasing cold spot temperature. The obtained values of T_{vib}^{e-} are independent on the cold spot temperature for InCl but the values decrease slightly for InBr in the InBr/argon discharges. However, the slight decrease of T_{vib}^{e-} for InCl could be concealed by the large errors.

Figure 8.3(b) shows the weighting factor ξ of the fraction of the vibrational population characterized by T_{vib}^{e-} and the normalized values of the electron density. As for InBr in the InBr/argon discharge the relative trend of both quantities is similar. The deviation for InCl between ξ and the normalized electron density at high cold spot temperature can be explained by the limited significance of the parameters obtained from the simulation.

Population Densities of Excited States

The relative trends of the population density of the InCl A state has been evaluated according to section 4.1.1 to allow for a comparison to InBr. Figure 8.4(a) shows the density of the InCl A state together with the population density of the InBr A state measured in the InBr/argon discharge described in section 7.1. It can be seen that the relative trend of both population densities shows a similar increase with increasing cold spot temperature.

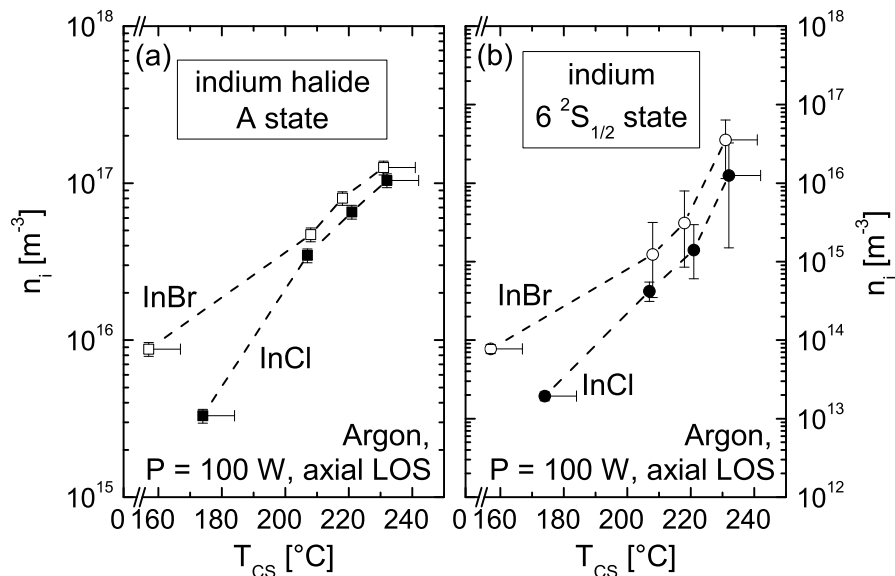


Figure 8.4: Population density (a) of the InCl A state together with the InBr A state measured in the InBr/argon discharge described in section 7.1 and (b) of the indium 6²S_{1/2} state measured in both the InCl/argon (labelled InCl) and the InBr/argon discharge (labelled InBr) at varying T_{CS} .

Figure 8.4(b) shows the population density of the excited $6\ ^2S_{1/2}$ indium state obtained from OES measurements at the InCl/argon and at the InBr/argon plasma. It can be seen that the values measured at the InBr/argon discharge are larger than the ones obtained in the InCl/argon plasma. This can be explained by the smaller excitation rate of indium atoms in the InCl/argon discharge which is caused by the smaller indium ground state density and the smaller electron density despite the higher electron temperature.

Radial Discharge Emission and Efficiency

The power which is radiated by the indium halide molecule in the InCl/argon and InBr/argon discharges at varying cold spot temperature is shown in figure 8.5(a). The corresponding power radiated by the indium lines at 410.2 and 451.1 nm is shown in figure 8.5(b). For both discharges the increase of Φ_{ik} with increasing cold spot temperature can be explained by the increasing population density of excited indium and indium halide states whereas the decrease at high T_{CS} -values is caused by the increasing opacity of the indium and indium halide emission. Considering the indium halide emission, the absolute values of Φ_{ik} are comparable for InCl and InBr. The lower emission at low cold spot temperature for InCl arises from the lower population density of the excited states as shown exemplarily for the A state in figure 8.4. However, the decrease of the emission of the indium lines at high values of T_{CS} is stronger for the InBr/argon discharge. This can be explained by the higher impact of radiation trapping due to the higher ground state density of indium (see figure 8.1(b)). Therefore at high cold spot temperature, the power radiated by the indium lines is lower in the InBr/argon plasma than in the InCl/argon discharge.

As the power radiated by the indium halide is similar in the InCl/argon and the InBr/argon discharge, also the efficiency of the InCl and InBr emission, which is shown in figure 8.6(a), is comparable. The higher power radiated by the indium lines in the InCl/argon discharge at high cold spot temperatures results in a larger efficiency considering the added indium halide and indium emission as shown in figure 8.6(b). The highest achieved efficiency for the InCl/argon discharge is $\eta_{InCl,In}^{Ar,100W} = 12.8 \pm 2.6\%$ whereas with the InBr/argon plasma only $\eta_{InBr,In}^{Ar,100W} = 10.0 \pm 2.0\%$ can be reached. It should be noted that for both discharges the maximum efficiency is obtained at $T_{CS} \approx 220\ ^\circ\text{C}$.

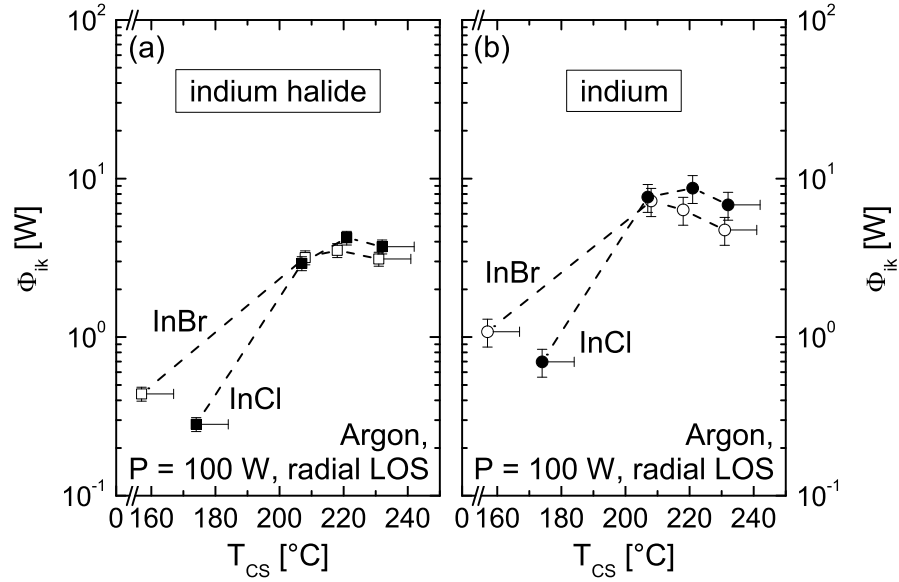


Figure 8.5: Part (a): power radiated by InCl (330 – 380 nm, InCl/argon discharge) and InBr (350 – 400 nm, InBr/argon discharge) at varying cold spot temperature. Part (b): power radiated by indium (at 410.2 and 451.1 nm) with varying T_{CS} for both discharges.

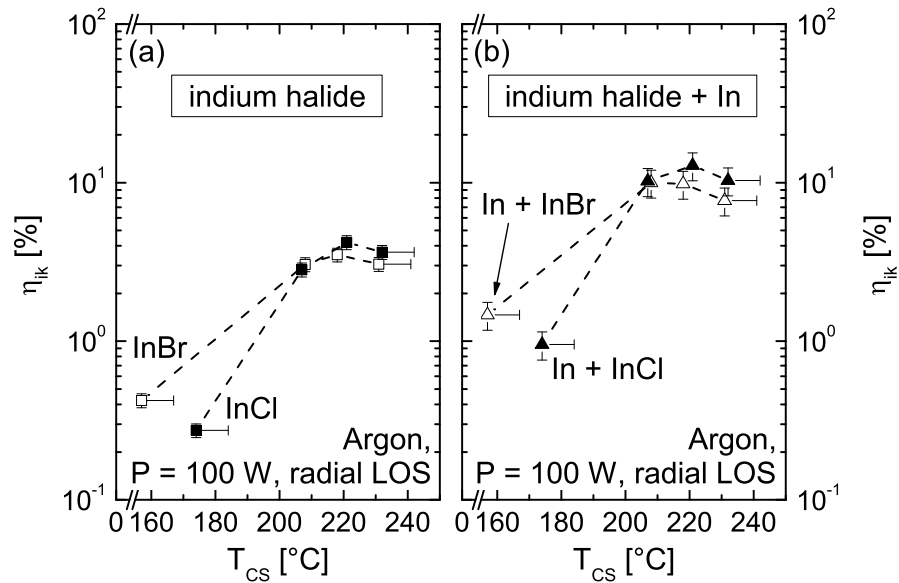


Figure 8.6: Part (a): efficiency of the indium halide emission of the InCl/argon and InBr/argon discharge with varying T_{CS} . Part (b): efficiency of the added indium halide and indium emission for both discharges with varying T_{CS} .

Summary

In general, the relative trends of the plasma parameters at increasing T_{CS} are the same for both InBr and InCl whereas the absolute values differ. For example the indium ground state density is lower in the InCl/argon discharge by roughly one order of magnitude due to the higher dissociation energy of InCl. As this results in a higher influence of the background gas on the discharge, the electron temperature is higher but the electron density is smaller in the InCl/argon discharge than in the InBr/argon plasma. At high cold spot temperatures, the discharge is solely dominated by atomic indium which causes similar plasma parameters for the InCl and the InBr discharge.

The relative trends of the molecular temperatures for InCl and InBr at varying cold spot temperature are similar despite the poor reproduction of the InCl spectrum by the simulation. Therefore, the relevant population processes of the rovibronic indium halide states can be assumed to be the same in the InCl/argon and in the InBr/argon discharge.

The smaller indium ground state density in the InCl/argon discharge results in a smaller impact of reabsorption effects on the indium emission. As the emission of the indium lines at 410.2 and 451.1 nm contribute roughly two thirds to the radiated power, the maximum efficiency of the added indium halide and indium emission of $\eta_{InCl,In}^{Ar,100W} = 12.8 \pm 2.6\%$ is higher than the one achieved in the InBr/argon discharge despite a similar indium halide radiation. For both indium halides, the maximum efficiency is also obtained at cold spot temperatures between 210 and 220 °C.

8.2 Variation of the RF-Power

As the measurements with InBr at 100 and 40 W RF-power proved a better efficiency of the InBr and indium emission at lower power (see section 7.2), also the InCl/argon discharge has been investigated at 40 W and a varying cold spot temperature. The same discharge vessel filled with 1 mbar argon and 1.5 mg InCl had been used as for the investigations of the previous section. As for InBr, systematic measurements below 40 W were not possible as the plasma constricted.

Similar to the InBr/argon discharge, the relative trends of the plasma parameters in InCl/argon discharges at varying cold spot temperature are independent of the RF-power but the absolute values are different. As with InBr (see section 7.2), reabsorption effects of the indium halide band and the indium lines limit

the amount of radiation that escapes from the InCl/argon discharge which in turn limits the efficiency of the discharge at high RF-power. In figure 8.7(a) the efficiency of the generation of InCl radiation and in figure 8.7(b) the one of the added InCl and indium radiation is shown at varying cold spot temperature for 40 and 100 W. For a RF-power of 40 W no InCl-emission is detectable below a cold spot temperature of 170 °C. The decrease of the power results in a higher efficiency of the added InCl and indium emission from $\eta_{InCl,In}^{Ar,100W} = 12.8 \pm 2.6\%$ to $\eta_{InCl,In}^{Ar,40W} = 24.1 \pm 4.8\%$ which is an increase of about a factor of 2. The same efficiency increase is achieved by reducing the RF-power from 100 to 40 W in the InBr/argon discharge.

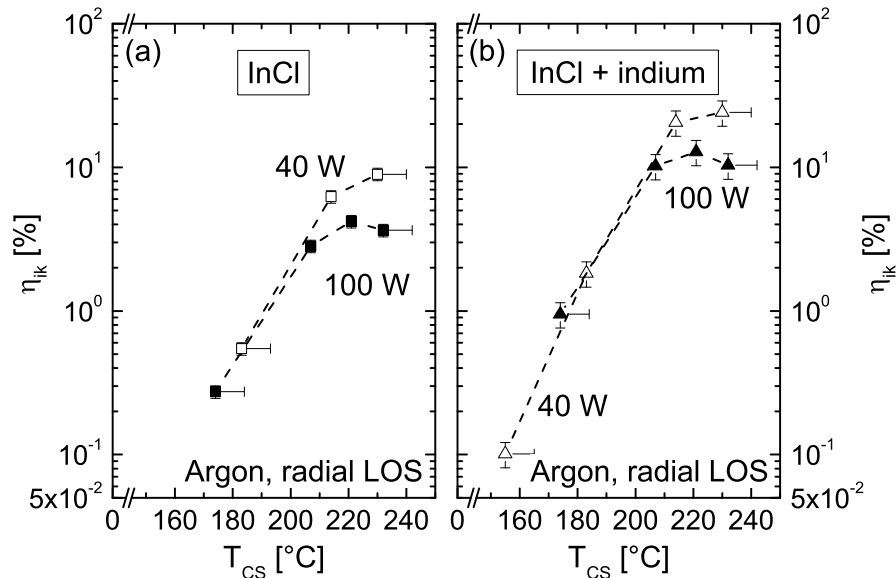


Figure 8.7: Efficiency of (a) the InCl emission (330 – 380 nm) and (b) of the added InCl and indium emission (at 410.2 and 451.1 nm) with varying cold spot temperature for 40 and 100 W RF-power.

8.3 Variation of the Background Gas

Like the background gas variation in the InBr/rare gas discharge, also for InCl the rare gases neon, argon and krypton have been investigated. As a lower RF-power results in a higher efficiency (see sections 7.2 & 8.2), the discharges have been operated at the lowest possible power which is defined by the requirement that the plasma has to fill out the whole discharge vessel volume. The same threshold-powers as in the InBr/rare gas plasmas (see section 7.3) have been

obtained for InCl: 40 W for argon and krypton as background gas and 70 W for neon. However, if krypton is used as background gas for InCl, the stability at high cold spot temperatures is worse than with InBr. Therefore no measurement above $T_{CS} = 215$ °C could be carried out in the InCl/krypton discharge.

Independently of the rare gas type the same relative trend of the discharge characteristics at varying cold spot temperature is obtained for the InCl/rare gas discharges which is caused by the transition from a rare gas dominated plasma to an indium halide/indium dominated discharge. Figure 8.8 shows the achieved efficiencies of the generation of the InCl emission and of the added InCl and indium emission. Similar to the InBr/rare gas discharges, the best efficiencies are obtained with neon or argon as background gas at a cold spot temperature between 220 and 230 °C: $\eta_{InCl,In}^{Ne,70W} = 22.7 \pm 4.5\%$ and $\eta_{InCl,In}^{Ar,40W} = 24.1 \pm 4.8\%$. It should be noted that only the utilization of argon provides a stable discharge over the whole cold spot temperature range which favours its utilization in the lamp application.

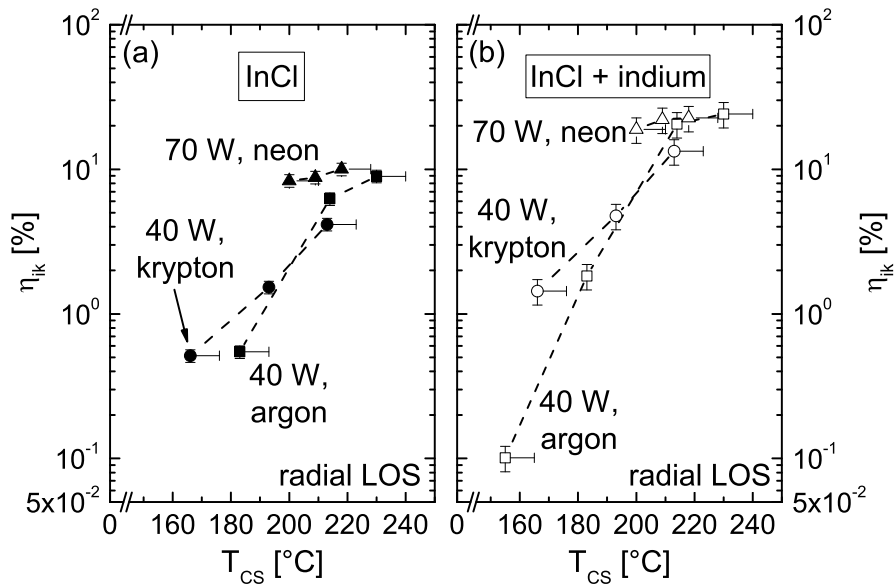


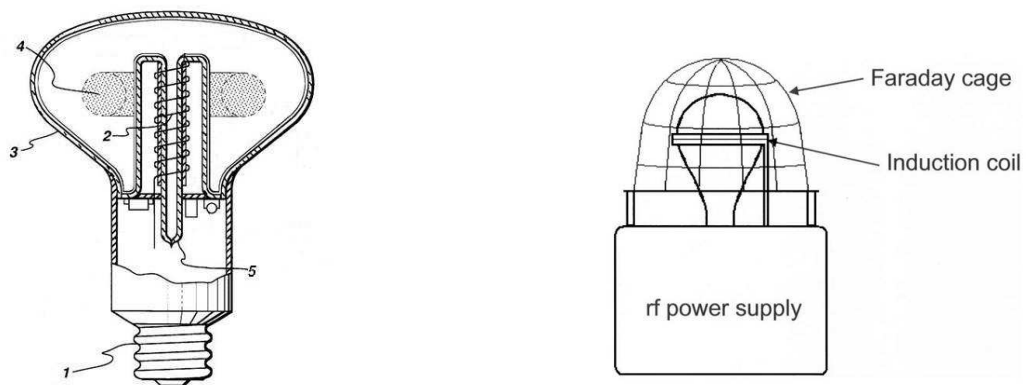
Figure 8.8: Efficiency (a) of the InCl radiation between 330 and 380 nm and (b) of the added InCl and indium emission at varying cold spot temperature for different background gases.

9 Outlook on a Low Pressure Indium Halide Lamp

Lamp Design

An indium halide/rare gas low pressure discharge lamp requires inductive RF-coupling and a high cold spot temperature around 220 °C (see sections 6 & 7.1). These requirements have to be considered in the lamp design which makes a direct “drop-in” substitution of mercury in conventional fluorescent lamps difficult.

The space required for the RF-generator is not an issue as conventional fluorescent lamps with an electronic ballast are also equipped with a RF-generator (operating at several 10 kHz) which is placed in the lamp mount or, in the case of compact fluorescent lamps, in the lamp socket. As already mentioned in section 2.3, several inductively coupled low pressure discharge lamps have already been designed for mercury/rare gas discharges [Lap10, LLLG04, Wha93]. Two examples of such lamps are shown in figure 9.1. The lamp shown in part (a) is designed in a way suitable for an installation in a conventional bulb socket (labelled 1). The RF-solenoid (2) is located on the inner side of the bulb (3) which results



(a) After [BGAS98].

(b) After [LLLG04].

Figure 9.1: Sketches of inductively coupled low pressure discharge lamp designs.

in a toroidal plasma shape (4). The cold spot is located on the inner stem (5) and reaches the optimum temperature intrinsically. In the lamp design shown in part (b) the RF-solenoid is wound around the bulb and a Faraday cage is applied to prevent electromagnetic interference issues. To avoid a partly blocking of the emitted radiation by the outer RF-solenoid, the turns could be manufactured out of transparent conducting oxides.

Low pressure sodium lamps operate at a slightly higher cold spot temperature (260 °C, see section 2.2) than required for indium halide/rare gas discharge lamps (220 to 230 °C). Care has been taken in the design of low pressure sodium lamps to reach the optimum T_{CS} -value intrinsically in lamp operation. The infrared reflective additional jacket which is placed around the actual discharge vessel can be seen in figure 9.2 where an exemplary sketch of the setup of a low pressure sodium lamp is shown. A lamp setup suitable for indium halide/rare gas discharges can be designed as a mixture of the setups of figure 9.1 where the RF and bulb design could be adopted and of figure 9.2 where the additional jacket with the infrared reflective coating could be adopted. Furthermore, in low pressure sodium lamps neon is used as background gas which enhances the wall temperature as described in section 2.2. However, if neon is utilized in the inductively coupled discharges investigated in this work, instabilities occurred especially at low cold spot temperatures. Such low values of T_{CS} are obtained during the starting phase of a lamp which makes an operation of an indium halide/neon discharge lamp problematic without additional heating. Nevertheless, the instabilities could possibly be avoided by varying the neon pressure or by applying mixtures of argon and neon as background gas.

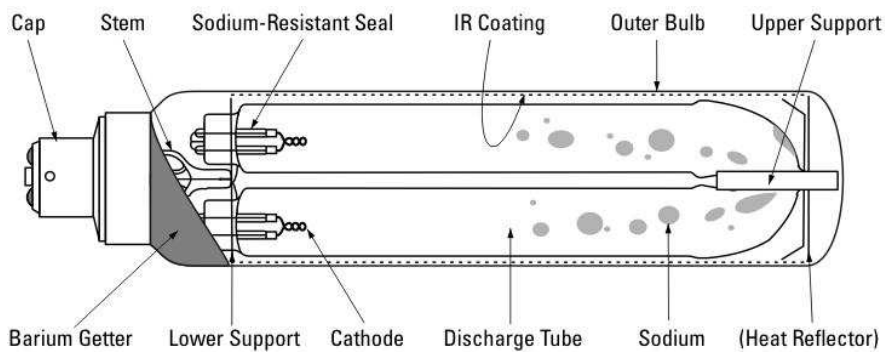


Figure 9.2: Sketch of the design of a low pressure sodium lamp [Hoo11].

Phosphors and Lamp Emission

As the radiation of indium halide/rare gas discharges is primarily located in the near UV spectral range, phosphors have to be utilized which convert the UV radiation into visible light. They could be applied to the inner wall of the additional outer jacket together with the infrared reflective coating to avoid interactions between the phosphor and the plasma. The choice of phosphors depends on their absorption spectrum which has to match the discharge's UV emission, and their emission spectrum which determines the properties of the emitted "white" light described by the colour rendering index (CRI) and the colour temperature. For a discussion of the basic concepts of phosphors, the underlying physics and application methods the reader is referred to [YSY06a, YSY06b]. Conventional fluorescent lamps achieve a CRI between 50 and 100 (which is the CRI of an incandescent lamp by definition). As a good CRI is in trade-off with the over-all efficiency, in general lighting lamps with a CRI of at least 80 are usually applied (the colour temperature is typically between 3000 and 4000 K). The application of phosphors to the indium halide/rare gas emission can be simulated in the following way:

If the emission spectrum $\epsilon(\lambda)$ [W/(m³ nm)] of the indium halide/rare gas discharge is multiplied with the absorption curve $\kappa(\lambda)$ of the phosphor and integrated over the whole wavelength range, the amount of power P_{abs} [W/m³] which is absorbed by the phosphor is obtained:

$$P_{abs} = \int \epsilon(\lambda)\kappa(\lambda) d\lambda. \quad (9.1)$$

The quantum efficiency QE of a phosphor describes its efficiency of converting the absorbed UV photons into visible ones. Therefore, the amount of power which is reemitted by the phosphor in the visible spectral range P_{ems} is given by the product of the quantum efficiency and P_{abs} .

If the integral of the known relative phosphor emission spectrum is set equal to P_{ems} the spectral emission coefficient of the visible light is obtained. For the utilization of a blend of several phosphors, P_{ems} of each phosphor has to be weighted according to the blend composition. Folding the calculated emission in the visible spectral range with the eye sensitivity curve yields the lamp efficiency [lm/W] of generating visible light.

This approach is demonstrated for the InCl/argon discharge with 40 W RF-power at $T_{CS} = 230$ °C where the highest efficiency of generating indium ha-

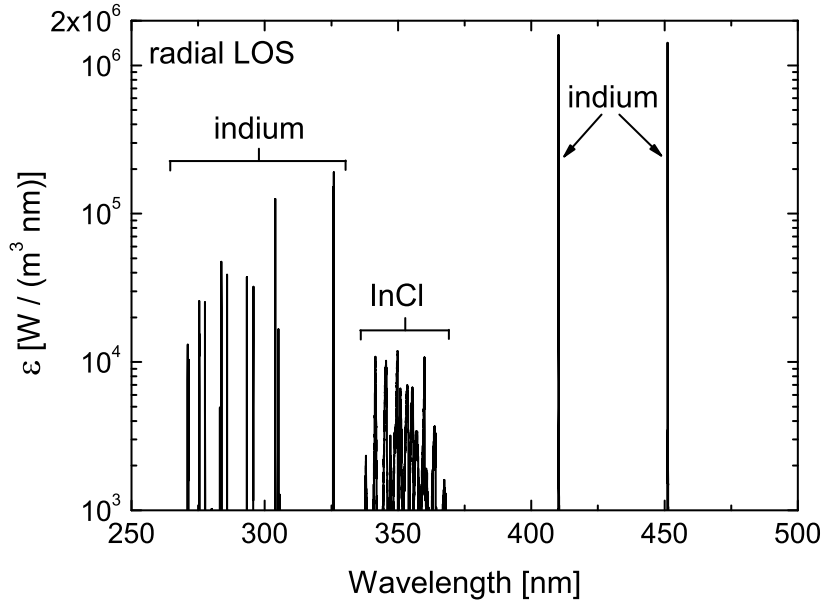


Figure 9.3: Emission spectrum of the InCl/argon discharge operated at 40 W and a cold spot temperature of $T_{CS} = 230^\circ\text{C}$. Above 500 nm no emission could be detected. The complete discharge emission is used for the conversion via phosphors.

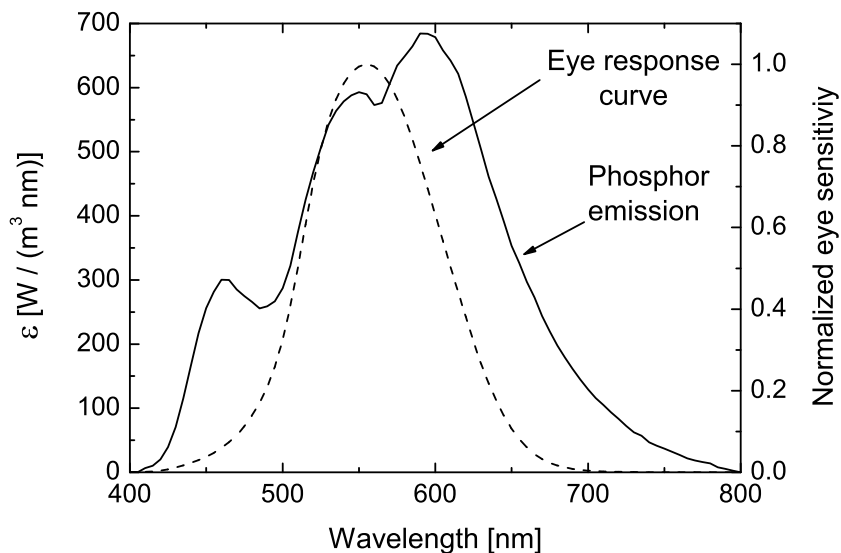


Figure 9.4: Simulated emission spectrum $\epsilon(\lambda)$ of a phosphor blend chosen in a way that a CRI of 80 is reached. The dashed line marks the photopic eye response curve.

lide/indium radiation is achieved. The corresponding emission spectrum is shown in figure 9.3 and the resulting emission spectrum of the phosphor is shown in figure 9.4. The complete discharge emission between 250 and 500 nm has been considered for the conversion into white light. With the utilized phosphor blend which has been chosen that a CRI of 80 is reached, an over-all lamp-efficiency of 60 lm per W RF-power and a colour temperature of 3760 K is achieved.

Summary

Concepts of inductive RF-coupling and of an intrinsic cold spot temperature control are already realized in commercially available lamps. For the lamp design of a low pressure indium halide discharge lamp these concepts can be adopted and merged. The near UV discharge emission of indium and of the indium halide molecule has to be converted into visible “white” light by the application of phosphors. If the phosphor blend is chosen to reach a colour rendering index of at least 80 which allows for the general lighting application, an over-all lamp efficiency of 60 lm/W and a colour temperature of 3760 K can be achieved. This efficiency is about a factor of two lower than the one of the best linear fluorescent lamps but similar to compact fluorescent lamps. An important point that still has to be investigated is the operating lifetime of the lamp. However, as this requires long-term stability measurements of the light output, these investigations have not been carried out yet.

In summary, the requirements concerning the efficiency and the colour rendering index for the utilization of a low pressure indium halide discharge lamp for general lighting are reached. The next steps towards a commercially available lamp are the manufacturing of a prototype and lifetime investigations.

10 Summary

As the role of fluorescent lamps for general lighting will have a continuing large importance in the near future, a substitution of the toxic mercury which is utilized in these light sources for the generation of UV emission is highly desirable. Therefore, the applicability of the diatomic indium monohalide molecules InBr and InCl in a RF-coupled low pressure discharge lamp has been investigated fundamentally in this work. The aim was to identify and understand the physical processes which determine the discharge characteristics and the efficiency of the generated near-UV emission of the indium halide and of indium.

Preliminary investigations which were performed within the scope of a diploma thesis showed that the evaporated indium halide amount has a great impact on the discharge characteristics. As this density is determined by the temperature T_{CS} of the coldest spot of the discharge vessel wall, an experimental setup with a well-defined cold spot was realized which allows for a controlled adjustment of the evaporated indium halide density. A comparison of density values obtained from white light absorption measurements of InBr in gas phase at varying cold spot temperature with those calculated according to the corresponding value of T_{CS} after the ideal gas law proved the proper performance of this setup.

In order to identify the RF-coupling type most advantageous for lighting applications, the inductive and capacitive coupling method have been compared. In addition, the impact of the cold spot temperature, the RF-power and the background gas type on the discharge characteristics and the efficiency have been investigated for InBr and InCl low pressure discharges. The plasmas have been generated in sealed cylindrical quartz vessel which contained 1.5 mg indium halide and on of the rare gases neon, argon and krypton at a pressure of 1 mbar. The whole discharge vessel is heated to allow for an evaporation of a considerable indium halide amount. As thermal insulation autoclaved aerated concrete is applied. The spectroscopic measurements are carried out at an axial line of sight whereas the radially emitted radiation relevant for lighting purposes has been measured at a radial line of sight.

The population density of excited atomic and molecular states determines the discharge radiation. Thus the diagnostic methods white light absorption and optical emission spectroscopy have been applied as these methods directly yield population densities. As the effects of absorption-signal saturation and reabsorption of emitted radiation within the plasma volume could lead to an underestimation of the determined population densities by orders of magnitude, these effects have been considered in the data evaluation. For this purpose radiation transport calculations which are based on the line profile of the transitions were carried out for the particular atomic emission and absorption lines. It has been shown that besides Doppler broadening, also the rather small contributions of pressure and natural broadening to the line profile have to be included in these calculations. For InBr and InCl a consideration of these effects is not possible as the required line broadening data is not available in the literature. Thus the absolute molecular population density values obtained from spectroscopic measurements can be assumed to underestimate the actual densities in the discharge. The measured relative trends of the molecular population densities are still significant.

In order to determine plasma parameters from spectroscopic measurements adequate population models are required. As the background gas emission vanishes in an indium halide rare gas discharge with increasing cold spot temperature, an extended corona model of indium (which is generated by the dissociation processes in the discharge) has been set up. The obtained values of the electron density n_e and the electron temperature T_e have been benchmarked by an evaluation of the established collisional-radiative model Yacora argon. The required population densities have been measured in an InBr/argon discharge at 100 W RF-power at low cold spot temperatures, where emission both from argon and indium is detectable. It turned out that the T_e -values obtained with the extended corona model of indium show the same relative trend as those obtained from Yacora argon but the absolute values are larger. The n_e -values obtained from the two population models coincide within the error bars. The deviation of T_e could be caused by disregarding relevant population processes in the extended corona model or by a non-Maxwellian energy distribution function of the electrons in the discharge. However, a consideration of additional processes or a determination of the electron energy distribution function is not possible. But the electron temperature and density obtained from the extended corona model of indium can be used for a qualitative understanding of the fundamental discharge characteristics dependencies as the relative T_e and n_e trends can be considered reliable.

The molecular temperatures which describe the rovibrational population of the indium halides determine the shape of the molecular emission spectra. These temperatures are obtained via adjusting the simulated emission spectra arising from the $A - X$ and $B - X$ transitions to the measured ones by varying the input parameters of the simulation. The simulation of the InBr spectrum which had initially been set up during the preliminary diploma thesis has been improved to allow for a consideration of both electron impact and inelastic heavy particle collisions as population processes. In the case of InBr, the simulated spectrum reproduces the measurement very well. The obtained relative vibrational population of the excited states is used to calculate effective transition probabilities which are required for the evaluation of spectroscopic measurements. The simulation has also been extended to the emission spectrum of InCl where the same calculation routine as in the InBr simulation is used but the molecular properties of InCl are applied. It turned out that the measured InCl spectrum is not reproduced very well by the simulation most probably due to inaccuracies of the available molecular constants and electronic dipole transition moments of InCl. But the simulation of the InCl emission can still be used for a qualitative evaluation of the population density of the InCl A.

As the utilization of indium halide molecules in low pressure plasmas requires energy-coupling with external electrodes, the methods of capacitive and inductive RF-coupling have been investigated with respect to their applicability and to the intensity of the light output. Using capacitive coupling for the generation of InBr/rare gas discharges, a strong implantation of indium ions into the discharge vessel wall occurred. This effect - which can be assigned to the capacitive RF-sheath formed in front of the electrodes - causes a blackening of the discharge vessel and a constant and rapid decrease of the indium halide and indium density in the plasma which makes systematic investigations impossible. Therefore, the comparison of the light output of the two RF-coupling methods has been carried out at a vacuum setup using rare gas discharges without indium halide additive. However, stationary or moving spatial intensity alterations, the so-called striations, occurred for all background gases except for argon. As this effect influences the light output, the measurements were solely carried out with argon. The pressure dependence of the emitted intensity which has been investigated at 80 W RF-power proved that the maximum light output of inductive coupling (achieved at 1 mbar argon pressure) exceeds the one of capacitive coupling (achieved at 3 mbar) by roughly one order of magnitude. A variation of the RF-power confir-

med the higher light output of inductive coupling for all applied RF-powers but it revealed that an operation of the capacitively coupled discharges is possible to much lower values of RF-power. For inductive coupling, the power reduction is only possible to a certain threshold value which depends on the pressure as below this value the plasma volume constricts. This would result in an improper operation of the well-defined cold spot setup for rare gas discharges with indium halide additive. Despite the smaller accessible RF-power range the inductive coupling method is more appropriate for generating indium halide/rare gas discharges for lighting applications than the capacitive method as the light output is higher and the implantation of indium ions is avoided. Thus inductive RF-coupling has been used for the performed investigations.

The impact of a variation of the cold spot temperature and therefore of the evaporated indium halide amount on the discharge characteristics has been investigated at an InBr/argon discharge at 100 W RF-power. Most evidently is the change of the plasma colour from argon dominated pink to indium dominated bright blue with an increasing T_{CS} . The measurements showed that also the plasma parameters T_e and n_e are influenced by the cold spot temperature. If the evaporated InBr amount is increased from $1.9 \times 10^{19} \text{ m}^{-3}$ to $5.1 \times 10^{20} \text{ m}^{-3}$ by increasing T_{CS} from 160 °C to 230 °C, the value of T_e decreases strongly from 0.8 eV to 0.4 eV. On the contrary, the electron density increases from $2.0 \times 10^{18} \text{ m}^{-3}$ to $1.1 \times 10^{20} \text{ m}^{-3}$. Via the ionization and power balance these trends can be assigned to the gradually substitution of light-weight argon ions which have a high ionization energy by heavy-weight InBr/indium ions which have a comparatively low ionization energy with increasing cold spot temperature. The population densities of the excited InBr and indium states increase strongly with increasing T_{CS} despite the decreasing T_e -values. E. g. the population density of the InBr A (indium $6 \text{ }^2\text{S}_{1/2}$) state increases from about $8.8 \times 10^{15} \text{ m}^{-3}$ ($7.8 \times 10^{13} \text{ m}^{-3}$) at $T_{CS} = 160 \text{ }^\circ\text{C}$ to $1.3 \times 10^{17} \text{ m}^{-3}$ ($3.6 \times 10^{16} \text{ m}^{-3}$) at $T_{CS} = 230 \text{ }^\circ\text{C}$. This trend is caused by the increasing electron density and the increasing ground state density of the corresponding species (the ground state density of indium increases from $4.5 \times 10^{16} \text{ m}^{-3}$ to $7.1 \times 10^{19} \text{ m}^{-3}$). In converse, the population density of excited argon states decreases with increasing T_{CS} despite the increasing electron density. This can be explained by the much stronger dependence of the excitation rate of argon on the decreasing electron temperature due to the high excitation energy.

The investigation of the molecular temperatures via the simulation of the relative molecular emission showed that the vibrational levels of the InBr ground

state are populated both via inelastic collisions with heavy particles and electrons in the discharge. If the cold spot temperature is increased which results in an increasing electron density, also the importance of inelastic electron collisions increases accordingly. This vibrational population is transferred to the vibrational states of the excited A and B states via electron impact excitation in the plasma. The rotational population of the particular vibronic InBr states is determined by inelastic heavy particle collisions. At high cold spot temperatures the shape of the molecular emission is slightly distorted by reabsorption effects. Within the investigated cold spot temperature range, the obtained variation of the molecular temperatures does not lead to a broader distribution of the A – X and B – X emission spectra which would lower the impact of reabsorption effects.

The power radiated by the InBr/argon discharge is distributed almost equally between the indium emission line at 410.2 nm, the one at 451.1 nm and the indium halide emission each having a share of just under one third. Thus, the contribution of indium to the discharge emission is very important. Increasing the cold spot temperature results in an increase of both the InBr and indium emission due to the increasing population density of the corresponding excited states. However, above $T_{CS} \approx 210 - 220$ °C the intensity of the InBr and indium emission decreases again despite the increasing population density as radiation trapping occurs. The efficiency of generating InBr and indium emission is defined as the measured radiation output divided by the RF-power which is coupled into the plasma (measured by a powermeter). The InBr/argon discharge at 100 W RF-power exhibits an efficiency maximum of $\eta_{InBr,In}^{Ar,100W} = 10.0 \pm 2.0\%$ in a rather broad cold spot temperature range between 210 and 220 °C.

The above described transition of the discharge from rare gas dominated at low cold spot temperatures to indium halide and indium dominated at high T_{CS} -values is evident for all performed investigations independently on the background gas type, the applied RF-power and for both InBr and InCl. The relative trends of the plasma parameters are always similar but their absolute values depend on the particular discharge.

If the applied RF-power is decreased from 100 W to 40 W at an InBr/argon discharge, the maximum efficiency increases from $\eta_{InBr,In}^{Ar,100W} = 10.0 \pm 2.0\%$ to $\eta_{InBr,In}^{Ar,40W} = 17.8 \pm 3.6\%$. It has been demonstrated that this trend can be explained by the power-dependent radial population density profiles of InBr and indium. At high power, a higher ground state density close to the discharge vessel wall - where the majority of InBr and indium radiation is generated - increases the

impact of reabsorption effects which lowers the radiation output. Hence, a higher applied RF-power increases the radiated power only slightly which results in a better efficiency of generating InBr and indium emission at lower RF-power.

For the background gases neon and krypton, the better efficiency at lower RF-power has also been verified. Hence, the influence of the background gas type on the discharge characteristics has been investigated using the particular lowest possible RF-power where the discharge volume is not yet constricted. This threshold-power is located at 40 W for argon and krypton and at 70 W for neon. At low cold spot temperatures, where the discharge is still dominantly influenced by the rare gas, the absolute values of the obtained plasma parameters are dependent on the background gas type. For neon, an operation at low T_{CS} -values is not possible due to instability problems. At high cold spot temperatures, the discharge is completely dominated by InBr and indium, i. e. also the plasma parameters are independent on the utilized rare gas type. As the maximum efficiency is located in the InBr and indium dominated regime, the values obtained for the different background gases coincide within the error bars: $\eta_{InBr,In}^{Ne,70W} = 15.6 \pm 3.1\%$, $\eta_{InBr,In}^{Ar,40W} = 17.8 \pm 3.6\%$ and $\eta_{InBr,In}^{Kr,40W} = 13.5 \pm 2.7\%$.

The differences in the discharge characteristics at varying cold spot temperature between the utilization of InBr and InCl have been investigated at an InCl/argon discharge at 100 W RF-power. In general, the relative trends of the plasma parameters at increasing T_{CS} are the same for both indium halides. But the absolute value of the indium ground state density is lower in the InCl/argon discharge by roughly one order of magnitude compared to the InBr/argon plasma as the dissociation energy of InCl is larger. This results in a higher influence of the background gas on the ionization and power balance at low and mid-range cold spot temperatures, i. e. the electron temperature is about a factor of 1.3 higher and the electron density about a factor of 3 smaller in the InCl/argon discharge than in the InBr/argon plasma. At high cold spot temperatures, the obtained T_e and n_e -values are independent on the indium halide molecule type and the background gas which indicates that the ionization and power balance are both dominated by indium despite the different indium densities. The smaller indium ground state density in the InCl/argon discharge also results in a smaller population density of excited indium states and hence, in general a lower indium emission. But the smaller ground state density also strongly lowers the impact of reabsorption effects on the indium emission which results in a larger amount of indium radiation escaping from the discharge. Therefore, the maximum efficiency

of $\eta_{InCl,In}^{Ar,100W} = 12.8 \pm 2.6\%$ (obtained at $T_{CS} \approx 220$ °C) is higher than the one achieved in the InBr/argon discharge despite a similar indium halide radiation.

The better efficiencies of InCl/rare gas discharges are also evident at varying RF-power and at different background gas types. In general, the same dependencies are exhibited in the InCl/rare gas plasma as in the InBr/rare gas discharges but if krypton is used as background gas for InCl, plasma instabilities make measurements above $T_{CS} = 215$ °C (where the maximum efficiency is not yet reached) impossible. The maximum efficiencies for the InCl/rare gas discharges using argon and neon as background gas are $\eta_{InCl,In}^{Ar,40W} = 24.1 \pm 4.8\%$ and $\eta_{InCl,In}^{Ne,70W} = 22.7 \pm 4.5\%$ respectively. They are achieved at a cold spot temperature between 220 and 230 °C which is almost the same range as for InBr/rare gas discharges.

In order to discuss the applicability of low pressure indium halide discharges as light sources, an outlook on the design requirements of such a lamp has been given. The RF-coupling of commercially available inductively coupled mercury/rare gas discharge lamps could be applied but if the optimum cold spot temperature of 210 – 230 °C should be reached without external heating, an additional outer jacket with an infrared reflective coating and/or neon as background gas must be utilized. The instability problems arising with neon at low T_{CS} values which occur during the starting phase of a lamp could possibly be avoided by varying the neon pressure or using a mixture of neon and argon. The phosphor-generated “white” lamp emission has been simulated. If the phosphor blend is chosen to reach a colour rendering index of 80 - which allows for the general lighting application - an over-all efficiency of 60 lm/W can be achieved.

In summary, the application of InBr and InCl in low pressure discharges for lighting purposes has been investigated fundamentally. The physical processes which determine the discharge characteristics and the efficiency of the generated indium halide and indium near-UV emission have been identified. It has been demonstrated, that the plasma generation via inductive RF-coupling is more appropriate for the lamp application than capacitive coupling. The intensity of the discharge emission is strongly dependent on the evaporated indium halide amount and on the applied RF-power whereas the background gas type plays only a minor role. This favours the utilization of argon as no instability problems arise with this background gas. The main process which limits the achievable maximum efficiency of the generated indium halide and indium emission is the reabsorption of

emitted photons within the plasma volume. The impact of this effect decreases with decreasing RF-power and in addition, the opacity of the intense indium lines is smaller in the InCl/rare gas discharge, i. e. more indium radiation is emitted than from the InBr/rare gas plasma. Therefore, the utilization of InCl and the operation at the lowest possible RF-power yields the highest efficiencies. The maximum efficiency achieved in this work is $\eta_{InCl,In}^{Ar,40W} = 24.1 \pm 4.8\%$ which is reached in a rather broad cold spot temperature range between 220 – 230 °C. The requirements of a low pressure indium halide discharge lamp prototype suitable for general lighting have been discussed. The corresponding over-all light source efficiency of 60 lm/W is a factor of two lower than the one of the best linear fluorescent lamps but similar to compact fluorescent lamps. The pressure of the background gas which had been kept constant at 1 mbar in the performed investigations might still allow for an improvement of the efficiency. Also a variation of the diameter of the discharge vessel might have an influence on the radial density distributions and therefore on the efficiency-limiting reabsorption effects. In general, the obtained results and efficiencies encourage further research as the application of low pressure rare gas discharges with indium halide additives for lighting shows great promise.

Appendix

A Molecular Constants and Ionization Cross Sections

Table A.1: *Molecular constants of the relevant isotopes of InBr and InCl [MYSR04].*

Isotope	Electronic state	T_{el} [cm ⁻¹]	ω_e [cm ⁻¹]	$\omega_e x_e$ [cm ⁻¹]	$\omega_e y_e$ [cm ⁻¹]	r_e [Å]
¹¹⁵ In ⁷⁹ Br	$X^1\Sigma^+(0^+)$	0.0	222.930	0.5198	-0.003 50	2.543 179
	$A^3\Pi_{0^+}(0^+)$	26 597.850	228.163	1.1950	-0.008 80	2.483 092
	$B^3\Pi_1(1)$	27 381.250	224.328	1.2730	-0.016 50	2.486 253
¹¹⁵ In ⁸¹ Br	$X^1\Sigma^+(0^+)$	0.0	221.370	0.5121	-0.008 80	2.543 180
	$A^3\Pi_{0^+}(0^+)$	26 597.871	226.500	1.1820	-0.008 20	2.483 049
	$B^3\Pi_1(1)$	27 381.257	222.701	1.2600	-0.015 70	2.487 100
¹¹⁵ In ³⁵ Cl	$X^1\Sigma^+(0^+)$	0.0	317.389	1.0320	-0.000 51	2.402 024
	$A^3\Pi_{0^+}(0^+)$	27 778.209	340.040	1.8800	-0.006 58	2.333 273
	$B^3\Pi_1(1)$	28 563.630	339.100	2.1930	-0.029 02	2.338 645
¹¹⁵ In ³⁷ Cl	$X^1\Sigma^+(0^+)$	0.0	310.718	0.9860	—	2.401 192
	$A^3\Pi_{0^+}(0^+)$	27 778.209	332.923	1.8020	-0.006 18	—
	$B^3\Pi_1(1)$	28 563.630	332.003	2.1020	-0.029 72	—

Table A.2: Molecular constants of the relevant isotopes of *InBr* and *InCl* [MYSR04] (continued).

Isotope	Electronic state	B_e [cm ⁻¹]	$\alpha_e \times 10^4$ [cm ⁻¹]	$D_e \times 10^8$ [cm ⁻¹]	$\beta_e \times 10^{10}$ [cm ⁻¹]
¹¹⁵ In ⁷⁹ Br	$X^1\Sigma^+(0^+)$	0.055 671	1.907 60	1.364 30	0.060 33
	$A^3\Pi_{0^+}(0^+)$	0.058 323	2.450 00	1.550 00	—
	$B^3\Pi_1(1)$	0.058 255	2.790 00	1.580 00	—
¹¹⁵ In ⁸¹ Br	$X^1\Sigma^+(0^+)$	0.054 856	1.865 89	1.313 96	0.059 70
	$A^3\Pi_{0^+}(0^+)$	0.057 587	2.727 00	1.522 00	—
	$B^3\Pi_1(1)$	0.057 441	2.909 00	1.541 00	—
¹¹⁵ In ³⁵ Cl	$X^1\Sigma^+(0^+)$	0.108 980	5.173 70	5.161 21	0.241 00
	$A^3\Pi_{0^+}(0^+)$	0.115 220	6.678 00	5.266 00	9.690 00
	$B^3\Pi_1(1)$	0.114 970	7.874 00	5.900 00	—
¹¹⁵ In ³⁷ Cl	$X^1\Sigma^+(0^+)$	0.104 469	4.855 76	6.621 25	0.250 00
	$A^3\Pi_{0^+}(0^+)$	0.110 445	6.267 43	4.838 80	8.717 60
	$B^3\Pi_1(1)$	0.110 208	7.391 16	5.421 38	—

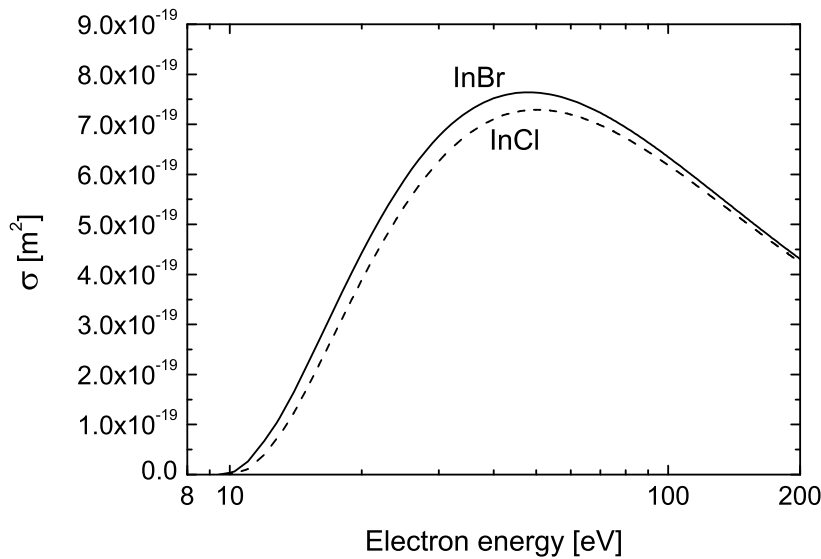


Figure A.1: Cross sections for electron impact ionization out of the ground state of *InBr* and *InCl* calculated after the Gryzinski-method as described in [BD65].

B Integration over Solid Angle in an Infinite Cylinder

For the calculation of the population escape factor an integration of a function $f(x)$ over the solid angle Ω has to be carried out. The variable $l(\Omega)$ denotes the length of the line of sight (which is along the x -axis) through the center of an infinite cylinder as shown in figure B.1 where the geometry of the setup is shown. To take advantage of the cylindrical symmetry the integration is performed using spherical coordinates:

$$d\Omega = \sin \vartheta' d\vartheta' d\phi, \quad (10.1)$$

where ϑ' and ϕ denote the angles according to figure B.1. However, it is easier to use the angle to the cross sectional area ϑ for the calculation as depicted in figure B.1. Then equation (10.1) turns into

$$d\Omega = \cos \vartheta d\vartheta d\phi. \quad (10.2)$$

The integral over the solid angle of a function $f(l(\Omega))$ is given by

$$\int f(l(\Omega)) d\Omega = \int_0^{2\pi} \int_{-\pi/2}^{+\pi/2} f(l(\Omega)) \cos [\vartheta(l(\Omega))] d\vartheta(l(\Omega)) d\phi. \quad (10.3)$$

If the length $l(\Omega)$ is defined according to figure B.1 the angle ϑ is correlated with $l(\Omega)$. As the physical quantities are cylindrically symmetrical the integration over ϕ simply yields 2π . Furthermore the symmetry with respect to the cross sectional

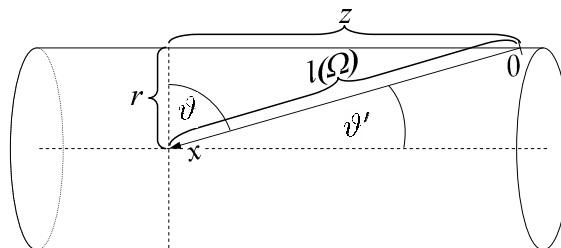


Figure B.1: Sketch of an infinite cylinder.

area results in:

$$\int_{-\pi/2}^{+\pi/2} f(l(\Omega)) \cos [\vartheta(l(\Omega))] d\vartheta(l(\Omega)) = 2 \int_0^{+\pi/2} f(l(\Omega)) \cos [\vartheta(l(\Omega))] d\vartheta(l(\Omega)x). \quad (10.4)$$

Therefore the integral over the solid angle of an infinite cylinder can be written as

$$\int f(l(\Omega)) d\Omega = 4\pi \int_0^{+\pi/2} f(l(\Omega)) \cos [\vartheta(l(\Omega))] d\vartheta(l(\Omega)). \quad (10.5)$$

For the integration it is advantageous to transfer the dependence of the function on $f(l(\Omega))$ to a dependence on the length z as depicted in figure B.1 which can be easily done as $l(\Omega) = \sqrt{r^2 + z^2}$. The substitution of the variable $l(\Omega)$ by the variable z in the integral leads to:

$$\int f(l(\Omega)) d\Omega = 4\pi \int_0^{\infty} f(l(\Omega)) \cos \left[\arctan \left(\frac{z}{r} \right) \right] \frac{r}{r^2 + z^2} dz. \quad (10.6)$$

As the integral is solved numerically, the integration from zero to ∞ cannot be carried out completely. Therefore the integral is only calculated from zero to a maximal value z_{max} and the integral from z_{max} to ∞ has to be approximated. This is done by calculating the solid angle of a spherical cap with a fixed radius l' as shown in figure B.2. The value of $l' = 1/2 (z_{max} + \sqrt{r^2 + z_{max}^2})$ is calculated after the intercept theorem and averages the lengths z_{max} and $\sqrt{r^2 + z_{max}^2}$. The integral of the function $f(l')$ over the solid angle of the spherical cap is given by

$$\int f(l') d\Omega = \int_{\vartheta_{min}}^{\pi/2} f(l') \cos \vartheta d\vartheta. \quad (10.7)$$

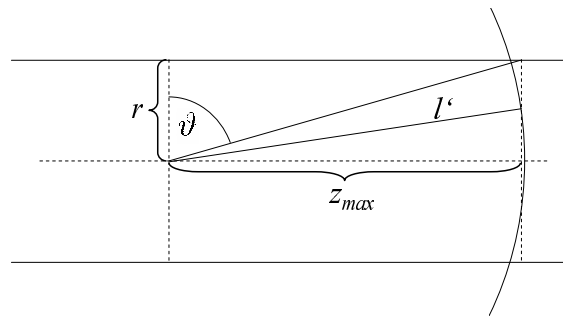


Figure B.2: Sketch of the spherical cap.

Substituting the angle ϑ with a length r' in direction of the radius r of the cylinder results in:

$$\int f(l') d\Omega = \int_0^r f(l') \frac{r'}{(l')^2} \frac{1}{\sqrt{1 - \frac{r'^2}{(l')^2}}} dr'. \quad (10.8)$$

As the value of z_{max} is chosen so that $r \ll l'$ is valid, the integral reduces to

$$\int f(l') d\Omega = \int_0^r f(l') \frac{r'}{(l')^2} dr' = \frac{f(l')}{(l')^2} \int_0^r r' dr' = \frac{r^2 f(l')}{2(l')^2}. \quad (10.9)$$

Therefore the integral over the solid angle of an infinite cylinder is calculated numerically by

$$\frac{1}{4\pi} \int f(l(\Omega)) d\Omega = \int_0^{z_{max}} f(l(\Omega)) \cos \left[\arctan \left(\frac{z}{r} \right) \right] \frac{r}{r^2 + z^2} dz + \frac{r^2 f(l')}{2(l')^2}. \quad (10.10)$$

C Data on the Hyperfine Splitting of Indium

The energy difference between the single hyperfine components (traditionally given in [MHz]) of the $5^2P_{1/2}$, $5^2P_{3/2}$, $6^2S_{1/2}$ (taken from [DMZ53]) and the $7^2S_{1/2}$ state (taken from [GGV90]) are shown in table C.1. The central wavelength of the lines resulting from the allowed transitions (selection rule $\Delta F = 0, \pm 1$) between the particular hyperfine split states and their relative intensity (after [DMZ53]) are summarized in table C.2. The wavelength of the lines is calculated by assuming that the central wavelength of the electronic transition coincides with the line with the lowest wavelength. This can be done as only the relative position of the particular lines is relevant for the calculation of Θ_{line} and f_{WLABS} . The single hyperfine lines of the transitions between the $6^2S_{1/2}$ ($7^2S_{1/2}$) state and the $5^2P_{1/2}$ or $5^2P_{3/2}$ states and the resulting line profile of the electronic transition are shown in figure C.1 (in figure C.2). The profiles have been calculated exemplarily for a gas temperature of 800 K and a argon background gas pressure of 3 mbar.

Table C.1: Energy difference between the particular hyperfine split states of the electronic $5^2P_{1/2}$, $5^2P_{3/2}$, $6^2S_{1/2}$ and $7^2S_{1/2}$ states.

State	Energy difference
$7^2S_{1/2}, F = 5$	} 2 710 MHz
$7^2S_{1/2}, F = 4$	
$6^2S_{1/2}, F = 5$	} 8 436 MHz
$6^2S_{1/2}, F = 4$	
$5^2P_{3/2}, F = 6$	} 1 753 MHz
$5^2P_{3/2}, F = 5$	
$5^2P_{3/2}, F = 4$	} 1 117 MHz
$5^2P_{3/2}, F = 3$	
$5^2P_{3/2}, F = 3$	} 669 MHz
$5^2P_{3/2}, F = 2$	
$5^2P_{1/2}, F = 5$	} 11 413 MHz
$5^2P_{1/2}, F = 4$	

Table C.2: Central wavelength and relative intensity [DMZ53] of the lines that arise from the transitions between the hyperfine split states of the electronic $5^2P_{1/2}$, $5^2P_{3/2}$, $6^2S_{1/2}$ and $7^2S_{1/2}$ states. The relative intensity can only be compared among one fine structure system.

Wavelength [nm]	Upper state	Lower state	Relative intensity
275.3909	$7^2S_{1/2}, F = 5$	$5^2P_{1/2}, F = 5$	0.668
275.3880	$7^2S_{1/2}, F = 5$	$5^2P_{1/2}, F = 4$	1
275.3916	$7^2S_{1/2}, F = 4$	$5^2P_{1/2}, F = 5$	1
275.3887	$7^2S_{1/2}, F = 4$	$5^2P_{1/2}, F = 4$	0.364
293.3638	$7^2S_{1/2}, F = 5$	$5^2P_{3/2}, F = 6$	1
293.3633	$7^2S_{1/2}, F = 5$	$5^2P_{3/2}, F = 5$	0.509
293.3630	$7^2S_{1/2}, F = 5$	$5^2P_{3/2}, F = 4$	0.185
293.3641	$7^2S_{1/2}, F = 4$	$5^2P_{3/2}, F = 5$	0.339
293.3638	$7^2S_{1/2}, F = 4$	$5^2P_{3/2}, F = 4$	0.509
293.3636	$7^2S_{1/2}, F = 4$	$5^2P_{3/2}, F = 3$	0.539
410.1824	$6^2S_{1/2}, F = 5$	$5^2P_{1/2}, F = 5$	0.668
410.1760	$6^2S_{1/2}, F = 5$	$5^2P_{1/2}, F = 4$	1
410.1871	$6^2S_{1/2}, F = 4$	$5^2P_{1/2}, F = 5$	1
410.1807	$6^2S_{1/2}, F = 4$	$5^2P_{1/2}, F = 4$	0.364
451.1329	$6^2S_{1/2}, F = 5$	$5^2P_{3/2}, F = 6$	1
451.1318	$6^2S_{1/2}, F = 5$	$5^2P_{3/2}, F = 5$	0.509
451.1310	$6^2S_{1/2}, F = 5$	$5^2P_{3/2}, F = 4$	0.185
451.1375	$6^2S_{1/2}, F = 4$	$5^2P_{3/2}, F = 5$	0.339
451.1367	$6^2S_{1/2}, F = 4$	$5^2P_{3/2}, F = 4$	0.509
451.1363	$6^2S_{1/2}, F = 4$	$5^2P_{3/2}, F = 3$	0.539

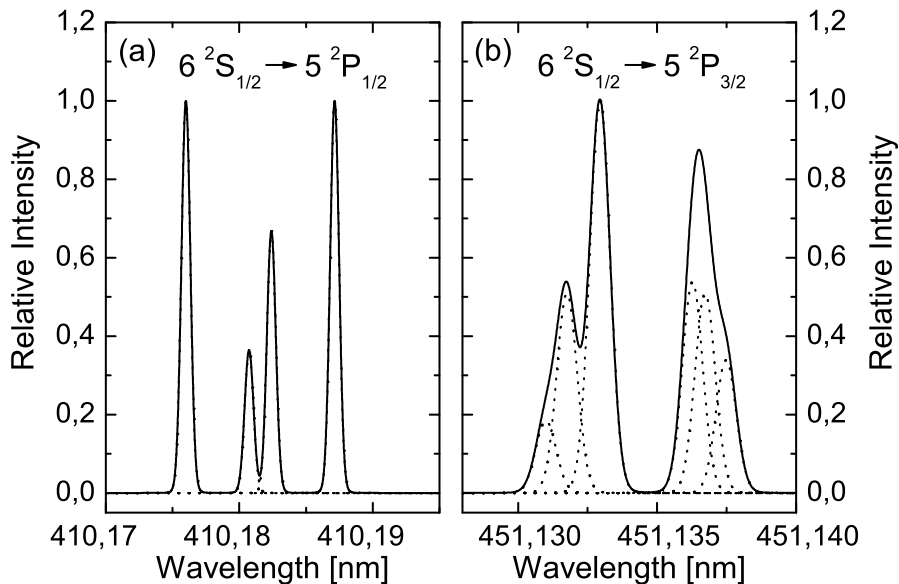


Figure C.1: The single hyperfine lines and the resulting line profile (a) of the $6\ ^2S_{1/2} \leftrightarrow 5\ ^2P_{1/2}$ transition and (b) of the $6\ ^2S_{1/2} \leftrightarrow 5\ ^2P_{3/2}$ transition. The profiles are calculated for a gas temperature of 800 K and a argon background gas pressure of 3 mbar.

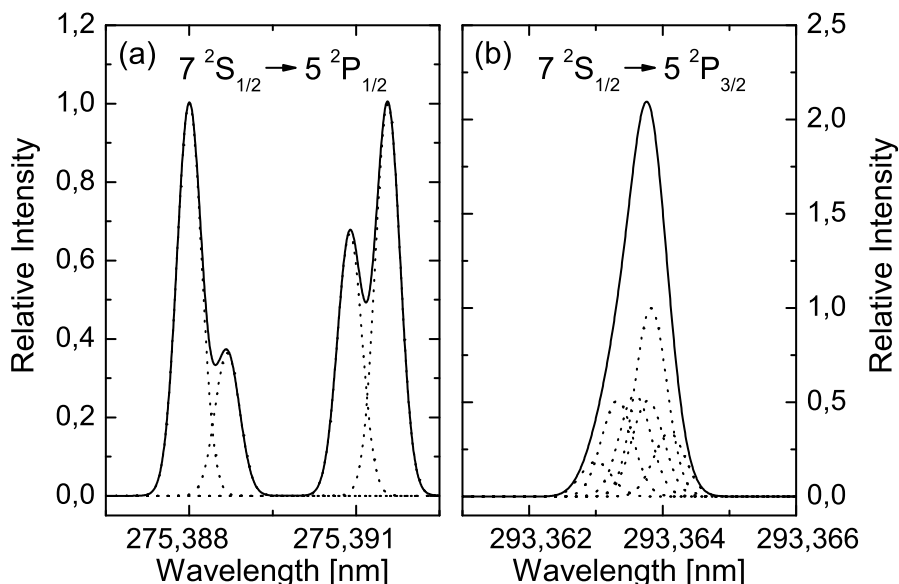


Figure C.2: The single hyperfine lines and the resulting line profile (a) of the $7\ ^2S_{1/2} \leftrightarrow 5\ ^2P_{1/2}$ transition and (b) of the $7\ ^2S_{1/2} \leftrightarrow 5\ ^2P_{3/2}$ transition. The profiles are calculated for a gas temperature of 800 K and a argon background gas pressure of 3 mbar.

Bibliography

- [AKK⁺96] S. A. Astashkevich, M. Käning, E. Käning, N. V. Kokina, B. P. Lavrov, A. Ohl, and J. Röpcke, *Radiative characteristics of $3p \Sigma$, Π ; $3d \Pi^-$, Δ^- states of H_2 and determination of gas temperature of low pressure hydrogen containing plasmas*, *Journal of Quantitative Spectroscopy and Radiative Transfer* **56** (1996), 725–751.
- [BD65] E. Bauer and C. Decker Bartky, *Calculation of Inelastic Electron-Molecule Collision Cross Sections by Classical Methods*, *Journal of Chemical Physics* **43** (1965), 2466–2476.
- [BD72] J. Berkowitz and J. L. Dehmer, *Photoelectron Spectroscopy of High-Temperature Vapors. II. Chemical Bonding in the Group III Monohalides*, *Journal of Chemical Physics* **57** (1972), 3194–3201.
- [BD08] A. Banerjee and K. K. Das, *Low-lying electronic states and spectroscopic properties of $InCl$ and $InCl^+$* , *Journal of Molecular Structure: THEOCHEM* **851** (2008), 134–146.
- [Beh91] K. Behringer, *Diagnostics and modelling of ECRH microwave discharges*, *Plasma Physics and Controlled Fusion* **33** (1991), no. 9, 997–1028.
- [Beh98] ———, *Escape Factors for Line Emission and Population Calculations*, IPP-Reoprt 10/11, Max-Planck-Institut für Plasmaphysik, Garching, 1998.
- [Ben90] C. Beneking, *Power dissipation in capacitively coupled rf discharges*, *Journal of Applied Physics* **68** (1990), 4461–4473.
- [Ber05] P.F. Bernath, *Spectra of atoms and molecules*, *Topics in Physical Chemistry Series*, Oxford University Press, 2005.

- [BF00] K. Behringer and U. Fantz, *The influence of opacity on hydrogen excited-state population and applications to low-temperature plasmas*, New Journal of Physics **2** (2000), no. 1, 23.1–23.19.
- [BF11] S. Briefi and U. Fantz, *Simulation of the A-X and B-X transition emission spectra of the InBr molecule for diagnostics in low-pressure plasmas*, Journal of Physics D: Applied Physics **44** (2011), no. 15, 155202–+.
- [BGAS98] J. C. Borowiec, S. Geoffrey, Malin S. A., and E. Soos, *United States Patent 5,841,229*, General Electric Company, Schenectady (NY), USA, 1998.
- [BLB⁺05] J. K. Böhlke, J. R. de Laeter, P. de Bièvre, H. Hidaka, H. S. Peiser, K. J. R. Rosman, and P. D. P. Taylor, *Isotopic compositions of the elements, 2001*, Journal of Physical and Chemical Reference Data **34** (2005), no. 1, 57–67.
- [BPCD09] A. Banerjee, A. Pramanik, S. Chakrabarti, and K. K. Das, *MRDCI studies on the electronic states of InBr and InBr⁺*, Journal of Molecular Structure: THEOCHEM **893** (2009), 37–47.
- [BPS55] R. F. Barrow, A. C. P. Pugh, and F. J. Smith, *The heats of sublimation of inorganic substances. part 4.-indium monobromide and monoiodide*, Transactions of the Faraday Society **51** (1955), 1657–1660.
- [Bri08] S. Briefi, *Spektroskopische Diagnostik an HF-angeregten Niederdruckplasmen mit Indiumbromid*, Diploma thesis, Universität Augsburg, 2008.
- [BWF11] S. Briefi, C. Wimmer, and U. Fantz, *Correction Factors for Saturation Effects in White Light and Laser Absorption Spectroscopy for Application to Low Pressure Plasmas*, submitted to Physics of Plasmas, 2011.
- [CB62] C. H. Corliss and W. R. Bozman, *NBS Monograph 53: Experimental Transition Probabilities for Spectral Lines of Seventy Elements*, United States National Bureau of Standards, 1962.

- [CC74] G. H. Copley and D. M. Camm, *Pressure broadening and shift of argon emission lines.*, Journal of Quantitative Spectroscopy and Radiative Transfer **14** (1974), 899–907.
- [Die10] S. Dietrich, *Verifikation von optischen Diagnostikmethoden an H_2 / D_2 – Plasmen*, PhD thesis, Universität Augsburg, 2010.
- [DMZ53] G. V. Deverall, K. W. Meissner, and G. J. Zissis, *Hyperfine structures of the resonance lines of indium (In^{115})*, Physical Review **91** (1953), no. 2, 297–299.
- [Doi95] P. Doidge, *A compendium and critical review of neutral atom resonance line oscillator strengths for atomic absorption analysis*, Spectrochimica Acta **50** (1995), 209–263.
- [DP40] M. J. Druyvesteyn and F. M. Penning, *The Mechanism of Electrical Discharges in Gases of Low Pressure*, Reviews of Modern Physics **12** (1940), 87–174.
- [DRS05] N. Denisova, G. Revalde, and A. Skudra, *Radial properties of high-frequency electrodeless lamps in argon mercury mixtures*, Journal of Physics D: Applied Physics **38** (2005), 3269–3274.
- [EHKU84] J. Eberz, G. Huber, T. Kuhl, and G. Ulm, *Pressure broadening and pressure shift of the 410 nm indium line perturbed by foreign gases*, Journal of Physics B: Atomic and Molecular Physics **17** (1984), no. 15, 3075–3082.
- [ES83] M. A. Zaki Ewiss and C. Snoek, *Lifetime measurements of low-lying S and D levels in indium*, Journal of Physics B: Atomic and Molecular Physics **16** (1983), no. 6, L153–L157.
- [FH98] U. Fantz and B. Heger, *Spectroscopic diagnostics of the vibrational population in the ground state of H_2 and D_2 molecules*, Plasma Physics and Controlled Fusion **40** (1998), 2023–2032.
- [FMM78] J. R. Fuhr, B. J. Miller, and G. A. Martin, *NBS Special Publication 505: Bibliography on Atomic Transition Probabilities*, United States National Bureau of Standards, 1978.

- [Fol46] H. M. Foley, *The pressure broadening of spectral lines*, Physical Review **69** (1946), 616–628.
- [Fro11] Frost & Sullivan, *The LED Revolution and Key Opportunities for Lighting Companies in the Global Market*, Frost & Sullivan market research, San Antonio (TX), USA, 2011.
- [FW06] U. Fantz and D. Wunderlich, *Franck Condon factors, transition probabilities, and radiative lifetimes for hydrogen molecules and their isotopomers*, Atomic Data and Nuclear Data Tables **92** (2006), 853–973.
- [GGK⁺03] A. Ganeev, Z. Gavare, V. I. Khutorshikov, S. V. Khutorshikov, G. Revalde, A. Skudra, G. M. Smirnova, and N. R. Stankov, *High-frequency electrodeless discharge lamps for atomic absorption analysis*, Spectrochimica Acta Part B: Atomic Spectroscopy **58** (2003), no. 5, 879–889.
- [GGV90] S. George, G. Guppy, and J. Verges, *Newly observed lines and hyperfine structure in the infrared spectrum of indium obtained by using a Fourier-transform spectrometer*, Journal of the Optical Society of America B **7** (1990), no. 3, 249–252.
- [GMS95] V. A. Godyak, V. P. Meytlis, and H. R. Strauss, *Tonks-Langmuir problem for a bi-Maxwellian plasma*, IEEE Transactions on Plasma Science **23** (1995), 728–734.
- [Gri64] H.R. Griem, *Plasma spectroscopy*, McGraw-Hill, 1964.
- [Gri74] ———, *Spectral line broadening by plasmas*, Pure and applied physics, Academic Press, 1974.
- [HAM52] T. Holstein, D. Alpert, and A. O. McCoubrey, *Isotope effect in the imprisonment of resonance radiation*, Phys. Rev. **85** (1952), 985–992.
- [Her50] G. Herzberg, *Molecular spectra and molecular structure, I. Spectra of diatomic molecules*, vol. 2, D. van Nostrand Company, Inc, 1950.
- [HHK⁺10] D. Hayashi, R. Hilbig, A. Körber, S. Schwan, R. Scholl, M. Boerger, and M. Huppertz, *Low-pressure indium-halide discharges for fluorescent illumination applications*, Applied Physics Letters **96** (2010), no. 6, 061503–+.

- [Hol47] T. Holstein, *Imprisonment of Resonance Radiation in Gases*, Physical Review **72** (1947), 1212–1233.
- [Hol51] ———, *Imprisonment of Resonance Radiation in Gases. II*, Physical Review **83** (1951), 1159–1168.
- [Hoo11] J. D. Hooker, *Homepage of the Museum of Electric Lamp Technology*, <http://www.lamptech.co.uk/Images/Illustrations/SOPg>, 2011.
- [Hop92] J. Hopwood, *Review of inductively coupled plasmas for plasma processing*, Plasma Sources Science Technology **1** (1992), 109–116.
- [HWF87] T. R. Hayes, R. C. Wetzell, and R. S. Freund, *Absolute electron-impact-ionization cross-section measurements of the halogen atoms*, Physical Review A **35** (1987), 578–584.
- [Hym79] H. A. Hyman, *Electron-impact ionization cross sections for excited states of the rare gases (Ne, Ar, Kr, Xe), cadmium, and mercury*, Physical Review A **20** (1979), 855–859.
- [IAE06] IAE report, *Light's Labour's Lost: Policies for Energy-efficient Lighting*, International Energy Agency, Paris, France, 2006.
- [Iro79] F. E. Irons, *The escape factor in plasma spectroscopy – I. The escape factor defined and evaluated*, Journal of Quantitative Spectroscopy and Radiative Transfer **22** (1979), 1–20.
- [KH07] A. Körber and D. Hayashi, *Absorption and emission spectra of gaseous indium monohalides*, ICPIG Proceedings (2007), 1224–1227.
- [Kol06] V. I. Kolobov, *Striations in rare gas plasmas*, Journal of Physics D: Applied Physics **39** (2006), no. 24, R487.
- [Kör09] T. Körner, *EDX-measurements, private communication*, AMU, Universität Augsburg, 2009.
- [Kov69] I. Kovács, *Rotational Structure in the Spectra of Diatomic Molecules*, Adam Hilger Ltd., London, 1969.
- [KS93] Hidetoshi Katori and Fujio Shimizu, *Lifetime measurement of the $1s_5$ metastable state of argon and krypton with a magneto-optical trap*, Physical Review Letters **70** (1993), no. 23, 3545–3548.

- [KZF09] S. Kitsinelis, G. Zissis, and E. Fokitis, *A strategy towards the next generation of low pressure discharge lamps: lighting after mercury*, Journal of Physics D Applied Physics **42** (2009), no. 4, 045209–+.
- [Lap10] W. P. Lapatovich, *Electrodeless Lamp Technology Overview*, LS12 White LED 3 Conference Proceedings, 2010.
- [Law68] G. M. Lawrence, *Radiance Lifetimes in the Resonance Series of Ar I.*, Physical Review **175** (1968), 40–44.
- [LDF78] T. Lubowiecka, T. Dohnalik, and L. Frasinski, *Measurement of the $6^2S_{1/2}$ state lifetime of In I by the Hanle effect*, Acta Physica Polonica A **54** (1978), 369–372.
- [LG98] M. A. Lieberman and V. A. Godyak, *From Fermi acceleration to collisionless discharge heating*, IEEE Transactions on Plasma Science **26** (1998), 955–986.
- [LH68] W. Lochte-Holtgreven (ed.), *Plasma diagnostics*, North-Holland publishing company, 1968.
- [Lid05] D. R. Lide (ed.), *Physical Constants of Inorganic Compounds in CRC Handbook of Chemistry and Physics, Internet Version 2005*, CRC Press, Boca Raton, FL, United States of America, 2005, <http://www.hbcpnetbase.com>.
- [Lis92] G. G. Lister, *Low-pressure gas discharge modelling*, Journal of Physics D: Applied Physics **25** (1992), 1649–1680.
- [LL94] M.A. Lieberman and A.J. Lichtenberg, *Principles of plasma discharges and materials processing*, Wiley-Interscience publication, J. Wiley & sons, 1994.
- [LLLG04] G. G. Lister, J. E. Lawler, W. P. Lapatovich, and V. A. Godyak, *The physics of discharge lamps*, Reviews of Modern Physics **76** (2004), 541–598.
- [LMP80] P. S. Landa, N. A. Miskinova, and I. V. Ponomarev, *Ionization waves in low-temperature plasmas*, Soviet Physics Uspekhi **132** (1980), 601–637.

- [MKS97] MKS instruments, *V/I probe 350 product manual*, Rochester (NY), USA, 1997.
- [Möl93] W. Möller, *Plasma and surface modeling of the deposition of hydrogenated carbon films from low-pressure methane plasmas*, Applied Physics A: Materials Science & Processing **56** (1993), 527–546.
- [Mor00] D. C. Morton, *Atomic Data for Resonance Absorption Lines. II. Wavelengths Longward of the Lyman Limit for Heavy Elements*, The Astrophysical Journal Supplement Series **130** (2000), no. 2, 403–436.
- [Mos09] P. Moskowitz, *private communication*, OSRAM SYLVANIA GmbH, Beverly (MA), USA, 2009.
- [Mul10] H. C. J. Mulders, *Spectroscopic Investigation of Indium Bromide for Lighting Purposes*, PhD thesis, Eindhoven University of Technology, 2010.
- [MYRS03] S. K. Mishra, R. K. S. Yadav, S. B. Rai, and V. B. Singh, *Potential energy curves and dissociation energies of diatomic indium halides*, Indian Journal of Physics **77B** (2003), 229–232.
- [MYSR04] S. K. Mishra, R. K. S. Yadav, V. B. Singh, and S. B. Rai, *Spectroscopic Studies of Diatomic Indium Halides*, Journal of Physical and Chemical Reference Data **33** (2004), 453–470.
- [Nat11] National Institute of Standard and Technologies, *NIST Atomic Spectra Database*, <http://physics.nist.gov>, 2011.
- [NF87] M. N'Dollo and M. Fabry, *Stark broadening of neutral and singly ionized gallium and indium lines*, Journal de Physique France **48** (1987), no. 5, 703–707.
- [NGB00] K. Y. Nagulin, A. K. Gil'Mutdinov, and O. R. Badrutdinov, *Spatial distribution of radiation intensity in high-frequency electrodeless discharge lamps*, Journal of Applied Spectroscopy **67** (2000), 14–21.
- [PS62] N. P. Penkin and L. N. Shabanova, *Oscillator Strengths of Spectral Lines of the Aluminum, Gallium and Indium Atoms*, Optics and Spectroscopy **14** (1962), 5–8.

- [RTMS96] J. M. de Regt, R. D. Tas, J. A. M. van der Mullen, and D. C. Schram, *A closed inductively coupled plasma for lighting purposes mapped by spectroscopical techniques*, Journal of Physics D: Applied Physics **29** (1996), 1489–1499.
- [San05] J. E. Sansonetti, *Handbook of Basic Atomic Spectroscopic Data*, Journal of Physical and Chemical Reference Data **34** (2005), 1559–2259.
- [SB58] F. J. Smith and R. F. Barrow, *The heats of sublimation of inorganic substances. part 6.-some halides of gallium and indium*, Transactions of the Faraday Society **54** (1958), 826–829.
- [SCC00] S.-H. Seo, C. Chung, and H.-Y. Chang, *Review of heating mechanism in inductively coupled plasma*, Surface and Coatings Technology **131** (2000), 1–11.
- [SFD⁺95] P. Schwerdtfeger, T. Fischer, M. Dolg, G. Igel-Mann, A. Nicklass, H. Stoll, and A. Haaland, *The accuracy of the pseudopotential approximation. I. An analysis of the spectroscopic constants for the electronic ground states of InCl and InCl₃ using various three valence electron pseudopotentials for indium*, Journal of Chemical Physics **102** (1995), 2050–2062.
- [SL60] K. Schäfer and E. Lax (eds.), *Landolt-Börnstein-Tabellenwerk Zahlenwerte und Funktionen aus Physik, Chemie, Astronomie, Geophysik und Technik*, 6th ed., Springer, 1960, Vol. IIa.
- [SMM⁺07] D. J. Smith, J. D. Michael, V. Midha, G. M. Cotzas, and T. J. Sommerer, *Efficient radiation production in a weakly ionized, low-pressure, nonequilibrium gallium-iodide positive column discharge plasma*, Journal of Physics D: Applied Physics **40** (2007), no. 13, 3842–3856.
- [SN74] L. L. Shimon and E. I. Nepiyov, *Effective cross sections of indium excitation by electron impact*, Ukrainskii Fizichnii Zhurnal (Ukrainian Journal of Physics, Ukrainian Edition) **19** (1974), 627–631.
- [Sob89] N.N. Sobolev (ed.), *Electron-excited molecules in nonequilibrium plasma*, Proceedings of the LEbedev Physics Institute, Academy of Sciences of the USSR, Nova Science Publishers, New York, 1989.

- [SRRR88] V. B. Singh, A. K. Rai, S. B. Rai, and D. K. Rai, *Studies in the A – X and B – X system of InBr*, Indian Journal of Physics **62B** (1988), 41–46.
- [SS91] B. D. Savage and K. R. Sembach, *The analysis of apparent optical depth profiles for interstellar absorption lines*, Astrophysical Journal **379** (1991), 245–259.
- [SVY81] I. I. Sobelman, L. A. Vainshtein, and E. A. Yukov, *Excitation of Atoms and Broadening of Spectral Lines*, Springer-Verlag, 1981.
- [SWF89] R. J. Shul, R. C. Wetzel, and R. S. Freund, *Electron-impact-ionization cross sections of the Ga and In atoms*, Physical Review A **39** (1989), 5588–5596.
- [TE90] M. F. Toups and D. W. Ernie, *Pressure and frequency dependence of ion bombardment energy distributions from rf discharges*, Journal of Applied Physics **68** (1990), no. 12, 6125–6132.
- [Tho88] A.P. Thorne, *Spectrophysics*, 2nd ed., Chapman and Hall, 1988.
- [THU82] K. Tachibana, H. Harima, and Y. Urano, *Measurements of collisional broadening and the shift of argon spectral lines using a tunable diode laser*, Journal of Physics B: Atomic and Molecular Physics **15** (1982), no. 18, 3169–3178.
- [TL99] M. M. Turner and M. A. Lieberman, *Hysteresis and the E-to-H transition in radiofrequency inductive discharges*, Plasma Sources Science Technology **8** (1999), 313–324.
- [TRBO89] S. A. Mucklejohn T. R. Brumleve and N. W. O’Brien, *The preparation and vapour pressures of the indium(I) halides and the standard molar Gibbs free energy change for formation of InX from In(g) and X₂(g), (X = Cl, Br, or I)*, Journal of Chemical Thermodynamics **21** (1989), no. 11, 1193–1206.
- [Val77] O. Vallee, *Measurements of broadening of argon lines and oscillator strengths of resonance lines*, Journal of Quantitative Spectroscopy and Radiative Transfer **18** (1977), 327–336.

- [Way69] J. F. Waymouth, *Electric Discharge Lamps*, The M.I.T. Press, Cambridge, Massachusetts and London, England, 1969.
- [WBD⁺89] W. L. Wiese, J. W. Brault, K. Danzmann, V. Helbig, and M. Kock, *Unified set of atomic transition probabilities for neutral argon*, Physical Review A **39** (1989), no. 5, 2461–2471.
- [WBHF87] R. C. Wetzel, F. A. Baiocchi, T. R. Hayes, and R. S. Freund, *Absolute cross sections for electron-impact ionization of the rare-gas atoms by the fast-neutral-beam method*, Physical Review A **35** (1987), 559–577.
- [WDF09] D. Wunderlich, S. Dietrich, and U. Fantz, *Application of a collisional radiative model to atomic hydrogen for diagnostic purposes*, Journal of Quantitative Spectroscopy and Radiative Transfer **110** (2009), 62–71.
- [Wei08] H. Weiß, *Chemical analysis of the grey deposit at the inner wall of a discharge vessel*, Protocolnumber: DA-M 058/08, OSRAM R&D laboratories, OSRAM GmbH München, 2008.
- [Wha93] D.O. Wharmby, *Electrodeless lamps for lighting: a review*, Science, Measurement and Technology, IEE Proceedings A **140** (1993), no. 6, 465–473.
- [WM80] W. L. Wiese and G. A. Martin, *NSRDS-NBS 68: Wavelengths and transition probabilities for atoms and atomic ions: Part 2. Transition probabilities*, United States National Bureau of Standards, 1980.
- [YCA05] Á. Yanguas-Gil, J. Cotrino, and L. L. Alves, *An update of argon inelastic cross sections for plasma discharges*, Journal of Physics D: Applied Physics **38** (2005), 1588–1598.
- [YSY06a] W. M. Yen, S. Shionoya, and H. Yamamoto, *Fundamentals of Phosphors*, Taylor & Francis Group, CRC Press, Boca Raton (FL), USA, 2006.
- [YSY06b] ———, *Practical Applications of Phosphors*, Taylor & Francis Group, CRC Press, Boca Raton (FL), USA, 2006.
- [ZLYZ03] W. Zou, M. Lin, X. Yang, and B. Zhang, *Ab initio calculations on the ground and low-lying excited states of InCl*, Journal of Chemical Physics **119** (2003), 3721–3728.

Acknowledgements

Ich möchte mich hiermit bei allen bedanken, die zur Entstehung dieser Arbeit beigetragen haben, insbesondere bei:

- Prof. Dr.-Ing. Ursel Fantz für die hervorragende Betreuung in jeglichen Belangen während der ganzen Arbeit und für die Aufnahme am Lehrstuhl für Experimentelle Plasmaphysik, an dem ich eine fundamentale wissenschaftliche Arbeitsweise erlernen konnte.
- Prof. Dr. Wolfgang Brütting für die Übernahme des Zweitgutachtens.
- der Firma OSRAM für die finanzielle Ermöglichung der Arbeit und insbesondere bei Dr. Gerd Lieder für die sehr gute Betreuung und die vielfältigen Bemühungen.
- Dipl.-Phys. Roland Friedl für die herausragende freundschaftliche Zusammenarbeit, die Hilfe bei jeglichen Problemen sowie die zahlreichen und teilweise langwierigen aber immer lehrreichen Diskussionen und das geduldige Korrekturlesen der Arbeit.
- den aktuellen und ehemaligen Mitgliedern des Lehrstuhls für Experimentelle Plasmaphysik, insbesondere bei Dipl.-Phys. David Ertle und Uwe Kurutz, Florian Vogel, Patrick Gutmann, Sinan Kalafat, Christian Wimmer und Wolfgang Böhm für die gute Zusammenarbeit und die sehr gute Arbeitsatmosphäre.
- Dr. Dirk Wunderlich vom Max-Planck-Institut für Plasmaphysik für die Einweisung in die Benutzung des Programms TraDiMo.
- Dr. Timo Körner für die Ausführung von EDX-Messungen.
- der feinmechanischen Werkstatt für die kompetente Beratung und die Herstellung zahlreicher Komponenten für den Versuchsaufbau.

Ganz besonders möchte ich mich außerdem bei meiner Familie und meiner Freundin für ihr Verständnis und ihre Unterstützung bedanken.

Curriculum Vitae

Name: Stefan Briefi
Date of birth: 07/01/1984
Place of birth: Augsburg, Germany
Marital status: single

09/1990 – 07/1994: Fröbel-Volksschule Augsburg
(primary school)

09/1994 – 06/2003: Holbein Gymnasium Augsburg
(secondary school)

June 2003: “Allgemeine Hochschulreife” (A levels)

06/2003 – 03/2004: Military service

04/2004 – 10/2008: Physics studies at the University of
Augsburg

October 2008: Diploma in physics

11/2008 – 11/2011: PhD student at the chair for experimental
plasma physics of the University of
Augsburg

Augsburg, 23 December 2011